



Research on Engineering Structures & Materials

Volume 6 Issue 2 June 2020

P-ISSN: 2148-9807

E-ISSN: 2149-4088

J

R

E

S

M

www.jresm.org



Research Group

The International Journal of **Research on Engineering Structures and Materials (RESM)** is a peer-reviewed open access journal (p-ISSN: 2148-9807; o-ISSN: 2149-4088) published by MIM Research Group. It is published in February, June, September, and December.

The main objective of RESM is to provide an International academic platform for researchers to share scientific results related to all aspects of mechanical, civil and material engineering areas.

RESM aims the publication of original research articles, reviews, short communications technical reports, and letters to the editor on the latest developments in the related fields.

All expenditures for the publication of the manuscripts are most kindly reimbursed by *MIM Research Group*. Thus, authors do not need to pay for publishing their studies in the journal.

The scope of the journal covers (but not limited to) behavior of structures, machines and mechanical systems, vibration, impact loadings and structural dynamics, mechanics of materials (elasticity, plasticity, fracture mechanics), material science (structure and properties of concrete, metals, ceramics, composites, plastics, wood, etc.), nano-materials performances of new and existing buildings and other structural systems, design of buildings and other structural systems, seismic behavior of buildings and other structural systems, repair and strengthening of structural systems, case studies and failure of structural systems, safety and reliability in structural and material engineering, use of new and innovative materials and techniques in energy systems and mechanical aspects of biological systems (biomechanics and biomimetics).

The topics covered in RESM include:

- Structural Engineering
- Mechanical Engineering
- Material Engineering
- Earthquake Engineering
- Nano-technology
- Energy Systems
- Biomechanics and Biomimetics

Abstracting and Indexing

Please visit <http://www.jresm.org> for more information.

Graphics and Design

H. Ersen Balcioglu

ersen.balcioglu@usak.edu.tr

Yunus Demirtas

yunus.demirtas@usak.edu.tr



**RESEARCH on
ENGINEERING STRUCTURES &
MATERIALS**



Published by MIM Research Group

RESEARCH on ENGINEERING STRUCTURES & MATERIALS

Editorial Board

Editor in Chief		
Hayri Baytan Özmen	Usak University	Turkey

Editor (Energy, Thermodynamics)		
Canan Kandilli	Usak University	Turkey

Editor (Mechanics, Materials)		
H. Ersen Balcioğlu	Usak University	Turkey

Editor (Earthquake Eng., Structural Eng.)		
Michele Barbato	University of California Davis	USA

Editor (Mechanics, Biosystems, Meta-materials)		
Alp Karakoç	Aalto University	Finland

Editor (Guest Editor)		
Suha Orçun Mert	Iskenderun Technic University	Turkey

Editorial Office

Publishing Manager & Copyeditor		
H. Ersen Balcioğlu	Usak University	Turkey

Publishing Assistant		
Yunus Demritaş	Usak University	Turkey

Editorial Board Members

Farid Abed-Meraim	Arts et Metiers ParisTech	France
P. Anbazhagan	Indian Institute of Science	India
Raffaele Barretta	University of Naples Federico II	Italy
R.S. Beniwal	Council of Scientific and Industrial Research	India
Antonio Caggiano	University of Buenos Aires	Argentina
Noel Challamel	University of South Brittany	France
Abdulkadir Çevik	Gaziantep University	Turkey
J. Paulo Davim	University of Aveiro	Portugal
Hom Nath Dhakal	University of Portsmouth	UK
S. Amir M. Ghannadpour	Shahid Beheshti University	Iran
Ali Goodarzi	Harvard University	USA
Jian Jiang	National Institute of Standards and Technology	USA
Ramazan Karakuzu	Dokuz Eylül University	Turkey
Arkadiusz Kwiecien	Cracow University of Technology	Poland
Stefano Lenci	Universita Politecnica delle Marche	Italy
Yuan Meini	North University of China	China
Stergios A. Mitoulis	University of Surrey	UK
Alaa M. Rashad	Shaqra University	Saudi Arabia
Mohammad Mehdi Rashidi	University of Tongji	China
Pier Paolo Rossi	University of Catania	Italy
Neritan Shkodrani	Polythecnic University of Tirana	Albania
Faris Tarlochan	Qatar University	Qatar
Y.B. Yang	National Taiwan University	Taiwan

Advisory Board Members

Yinusa Amoo Ahmed	University of Lagos	Nigeria
Sevim Alışır	Ondokuz Mayıs University	Turkey
Mustafa Yasin Aslan	Usak University	Turkey
Huseyin Ersen Balcioglu	Usak University	Turkey
Beyhan Bayhan	Bursa Technical University	Turkey
Hektor Cullufi	Polytechnic University of Tirana	Albania
Preeta Datta	North Carolina State University	USA
J. Paulo Davim	University of Aveiro	Portugal
Akar Dogan	Munzur University	Turkey
Hany El-Hamshary	Tanta University	Egypt
Dulce Franco Henriques	Instituto Politécnico de Lisboa	Portugal
Halit Levent Hosgun	Bursa Technical University	Turkey
Ercan Isik	Bitlis Eren University	Turkey
Charles Langston	University of Memphis	USA
Ahmet Meram	KTO Karatay University	Turkey
Masoomeh Mirrashid	Semnan University	Iran
Mehmet Palanci	Istanbul Arel University	Turkey
Alaa M. Rashad	Building Materials Research and Quality Control Institute	Egypt
Fabio Rizzo	University of Chieti-Pescara	Italy
Behnam Rosti	Shiraz University of Technology	Iran
Tamer Saracyakupoglu	Istanbul Gelisim University	Turkey
Rudimylla Septimio Azeredo	Federal University of Southern and Southeastern Pará	Brazil
Anand B. Tapase	Karmaveer Bhaurao Patil College of Engineering	India
Hamide Tekeli	Süleyman Demirel University	Turkey
Onder Yesil	Usak University	Turkey

Advisory Board Members

Ferhat Yıldırım

Çanakkale Onsekiz Mart University

Turkey

In This Issue

Research Article

105 **Mehmet Palanci**

Yield response prediction of unsymmetrically reinforced concrete rectangular beams

Research Article

119 **Serço Serkis Yeşilkaya, Ünzile Ulutaş**

Band gap modification of spray pyrolysed ZnS films by doping and thermal annealing

Research Article

127 **Sevim Alisir, Sinem Cevik**

The effects of foundry sand components on the cast iron

Research Article

141 **Tuğba Gürmen Özçelik**

Investigation of glycerol-Ni(NO₃)₂·6H₂O /perlite composites as form stable phase change materials

Research Article

153 **Hatice Aylin Karahan Toprakci, Ayse Turgut, Ozan Toprakci**

Fabrication and characterization of vapor grown carbon nanofiber reinforced flexible polymer composites

Research Article

167 **Emmanuel Folorunso Olasehinde, Segun Michael Abegunde**

Preparation and characterization of a new adsorbent from raphia taedigera seed

Research Article

183 **Ahsen Ünal, Işıl Özer, Melek Erol Taygun, Sadriye Küçükbayrak**

Fabrication and in-vitro evaluation of copper doped bioactive glass/polymer composite scaffolds for bone tissue engineering

Free access to tables of content, abstracts and full text of papers for web visitors.

Copyright © 2020

Research on Engineering Structures & Materials

MIM Research Group Publications

ISSN 2148-9807

<http://www.jresm.org>

ABSTRACTING / INDEXING

The international journal of Research on Engineering Structures and Materials (RESM) is currently Abstracted/Indexed by CrossRef, Google Scholar, Universal Impact Factor, Scientific Indexing Service, Research Bible, CiteFactor, Electronic Journal Library, Open Academic Journals Index, Global Impact Factor, Directory of Research Journals Indexing, Root Society for Indexing and Impact Factor Service, Cosmos, Materials Science & Engineering Database (ProQuest) Engineering Journals (ProQuest), ULAKBİM TR Index (Tubitak), International Institute of Organized Research (I2OR), International Scientific Indexing (ISI), Publication Forum, Asos Indeks and under evaluation by many other respected indexes.

Check web site for current indexing info.





Research Article

Yield response prediction of unsymmetrically reinforced concrete rectangular beams

Mehmet Palanci*

Department of Civil Engineering, Istanbul Arel University, Istanbul, Turkey

Article Info

Article history:

Received 02 Aug 2019

Revised 11 Sep 2019

Accepted 15 Sep 2019

Keywords:

Reinforced Concrete Structures;
Unsymmetrically Reinforced Concrete Beams; Moment-curvature Analysis;
Cracked Stiffness

Abstract

Main components such as columns and beams of reinforced concrete (RC) buildings are constructed as symmetrically and unsymmetrically reinforced. Symmetrically reinforced concrete members are widely studied and some analytical/numerical approaches are provided. However, unsymmetrically reinforced concrete members are not adequately investigated and further research is required to predict response of these members. For this reason, this study focuses on strength and deformation capacity prediction of unsymmetrically RC members at yield which primarily required for the design and assessment. In the study, wide range of RC sections are generated and analyzed using different section dimensions, material types, reinforcement ratios and configurations to reveal behavior of these members. Influence of parameters on the responses is investigated and they are contributed to prediction equations by statistical evaluations. Prediction equations are first tested with analytical RC section results and comparisons have shown very good agreement. Equations are then applied to predict dynamic features of two experimental MDOF buildings. Evaluations have revealed the reliability of prediction equations in approximation of responses in building scale.

© 2019 MIM Research Group. All rights reserved.

1. Introduction

Structural behavior is strongly affected from structural member responses and both design and performance assessment of structures requires the determination of flexural strength capacity of members. If the structural member has adequate strength and the demand is lower than strength capacity, response is elastic. However, nonlinear deformations occur if the strength of members is exceeded and nonlinear deformation capacity is affected from the efficiency of member confinement for reinforced concrete (RC) members. On the other hand, design of structures requires the flexural strength capacity of members since it is expected that elastic demands (shear forces, bending moment etc.) should always be lower than the capacity of members.

In addition to design or assessment of structures, strength capacity of members has also crucial role in determination of dynamic characteristics (e.g. natural vibration period) of buildings since elastic stiffness (or cracked stiffness) of the members are strongly affected from capacity of member at yield level. Stiffness of members at elastic region can be obtained by moment-curvature (so called as $m-\phi$) analysis. Section dimensions, reinforcement details, strength of materials and their behavior should be defined to perform $m-\phi$ analysis. Although it is rapid to get results from $m-\phi$ analysis in today's computers, it becomes time-consuming and exhausting for complex structures which have high amount of input data. Other than complex analysis methods, simplified

*Corresponding author: mehmetpalanci@arel.edu.tr

^a orcid.org/0000-0002-9223-5629

DOI: http://dx.doi.org/10.17515/resm2019_141st0802

Res. Eng. Struct. Mat. Vol. 6 Iss. 2 (2020) 105-118

analytical or numerical approaches [1-5] can also be used to determine strength and deformation capacity of members. These approaches significantly increase time saving, but they are mostly concentrated on symmetrically RC members. It is known fact that RC structures are not only composite of symmetrically reinforced members and RC beams are frequently designed as unsymmetrically reinforced due to combined effects of dead, live and earthquake loads. Although behavior of these elements are simpler than columns as the axial load is omitted, combined effects of section dimensions, longitudinal reinforcement ratio (compression and tension) and strength of materials has uttermost importance on the flexural response of these members. Flexural response of unsymmetrically RC elements is also important to exhibit damage mechanism of beam-column joints and hence the structural behavior. If the sum of strength of beams is higher than strength capacity of columns, damage is expected to occur at column critical regions or vice versa. Similar approximation is also followed during the design phase of beam-column joints, but it is obligated that strength of columns should be higher than beams due to strong column-weak beam philosophy.

Estimation of cracked stiffness (i.e. flexural strength) of RC members are also increasingly becoming important topic in modern seismic codes (e.g. Eurocode-8 [6] and Turkish Building Earthquake Code (TBEC) 2018 [7]) to determine behavior in member and/or structural content. In the codes, various cracked stiffness values are recommended for different type of members such as columns and beams. Besides the fixed values, simplified equations are also provided to estimate cracked stiffness of members. However, these equations also need to determine flexural capacity of members since these equations involve the flexural strength and rotation capacity of members at yield.

All issues stated above clearly show that strength and hence stiffness of unsymmetrically reinforced concrete members has crucial role in both design and performance assessment of new and existing structures. For this reason, this study is aimed to propose prediction equations to express flexural strength and deformation capacity of unsymmetrically reinforced (RC) members at yield level. During the designation of prediction equations, wide range of RC sections are generated for different section dimensions, reinforcement ratios and material types to cover all possible cases. All generated RC members are then subjected to $m-\phi$ analysis. Effect of all considered structural attributes are evaluated considering the analysis results and then prediction equations are obtained by statistical interpretations. Proposed equations are then applied to simulated RC sections and compared with $m-\phi$ analysis results. In addition, dynamic characteristics of experimental building and different analytical multi-degree of freedom (MDOF) buildings are projected using provided equations.

2. Description of Modeling Assumptions and Analytical RC Beams

In Fig. 1, behavior of materials (unconfined concrete and reinforcement) used in this study are plotted. It can be said that constitutive laws for concrete and reinforcements are represented by Modified Kent Park [8] and Mander [9] model, respectively. In the figure, tensile strength of reinforcement and compression of unconfined concrete and their corresponding strains is described by notations of (f_c, ϵ_{co}) and (f_y, ϵ_{sy}) , respectively. Ultimate strength of reinforcement is notated as f_{su} . In the study, young modulus of steel (E_s) is taken 2×10^5 MPa. Yield strain (ϵ_{sy}) is obtained by proportion of f_y and E_s which is the elastic slope of reinforcement. It is worth to remind that behavior of both materials after yield level have no significant importance since the capacity of members at yield level is investigated.

During the analysis of sections, neutral axis depth (c_n), curvature (ϕ) and moment (M) is obtained using material behaviors shown in Fig. 1 for each increments of strain values until the predefined strain values are (i.e. stopping criteria) developed. Flexural strength (M_y) and curvature (ϕ_y) at yield is determined when the stopping criteria, assigned to extreme fibre concrete compression strain of 0.004 and extreme tension reinforcing bar strain of 0.015 according to Priestley et al. [10], is reached.

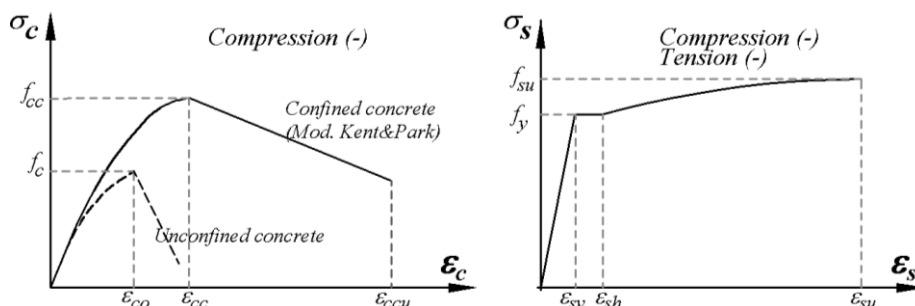


Fig. 1 Constitutive laws for materials used in $m-\phi$ analysis (Left: confined and unconfined concrete [8], Right: reinforcement [9])

In this study, beam width is taken between 250mm and 350mm with increment of 50mm. Section height is determined according to H/B ratio and this ratio is arranged between 1 and 4. Later, analytical RC sections are diversified by concrete compressive strength (f_c), longitudinal reinforcement ratio (ρ_l), mechanical reinforcement ratio (w'/w) and steel grade type (S220 and S420). It is worth to remind that, similar to Eurocode 8 [6], w and w' terms describe the mechanical reinforcement ratio of the tension (including the web reinforcement) and compression, respectively, longitudinal reinforcement. In the scope of study, more than 20,000 unsymmetrically reinforced analytical RC sections are considered and general attributes of generated analytical RC sections are given in Table 1. In addition to features of sections given in Table 1, RC sections are altered by different web reinforcement configurations. By this way, possibility of all cases is considered in the study.

Table 1 Range of parameters considered in generation of unsymmetrically RC sections

Parameters	Geometry of RC beams					
	Square			Rectangle		
	Min	Max	Increment	Min	Max	Increment
ρ_l	1%	4%	1%	1%	4%	1%
f_c (MPa)	10	35	5	10	35	5
f_y (MPa)	220	420	-	220	420	-
B (mm)	250	350	50	250	350	50
H (mm)	250	350	50	500	1000	100

3. Sectional Attributes on the Response of Unsymmetrically RC Beams

In order to investigate effect of section dimensions on the flexural response of RC sections, rectangular type members are used. In Fig. 2, relation between flexural strength (M_y) and section dimensions (B and H) is illustrated. It can be seen from the figure that section dimensions have significant contribution on the strength capacity of members and they can be involved in prediction equations. Palanci [4] showed that correlation

between BH^2 which includes combination of both dimensions, and moment capacity (M_y) of sections is satisfactory. For this reason, correlation between BH^2 and M_y values are compared in Fig. 2c. It can be observed from Fig. 2c that BH^2 is promising to exhibit relation with moment capacity of members compared to individual section dimensions

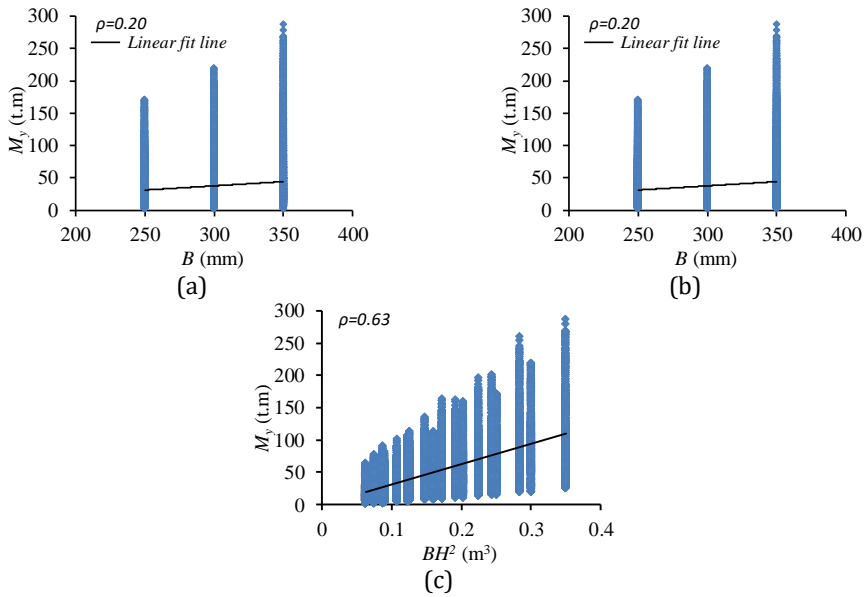


Fig. 2 Correlation between section properties and M_y (a: width (B), b: height (H), c: BH^2)

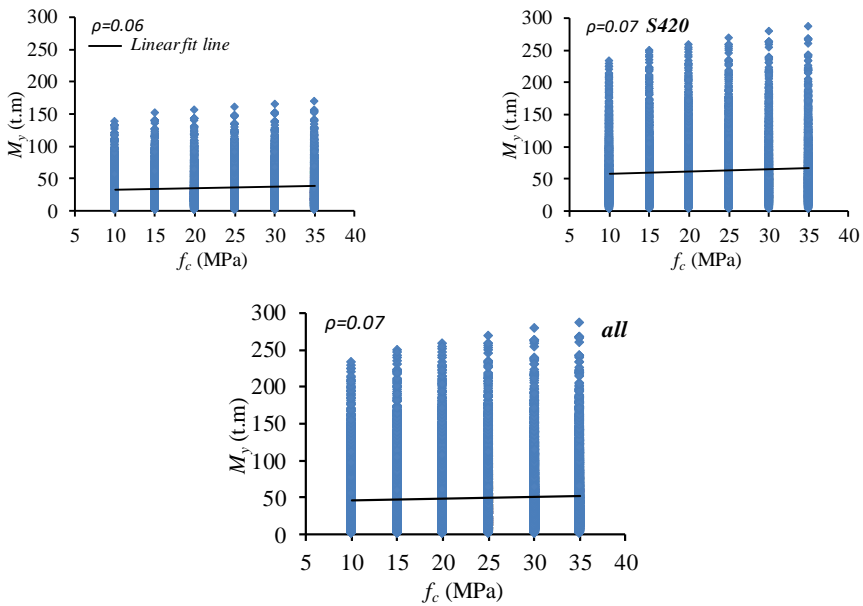


Fig. 3 Correlation between compressive concrete strength and M_y

In Fig. 3, relation of compressive concrete strength and moment capacity of section is illustrated for distinct steel grade type. It can be understood from the figure that compressive concrete strength type has no significant impact on the moment capacity of unsymmetrically RC members. However, it can be implied that moment capacities of sections which have S420 steel grade is higher than that of sections which have S220 steel grade.

It is real fact that longitudinal reinforcement ratio (ρ_l) significantly affects the strength capacity of RC members. In order to observe efficiency of ρ_l on the unsymmetrically RC sections, relation between ρ_l and M_y is observed in Fig. 4. Figure indicates that moment capacity of RC members is increasing with increasing longitudinal reinforcement ratio. It is worth to reminded relation of ρ_l and M_y is also investigated for S220 and S420 grades, respectively. Investigations have also revealed that higher correlations can be observed if the relation between ρ_l and M_y is studied for each steel grade type individually. Furthermore, it can be expressed that correlation between ρ_l and M_y parameters is satisfactory.

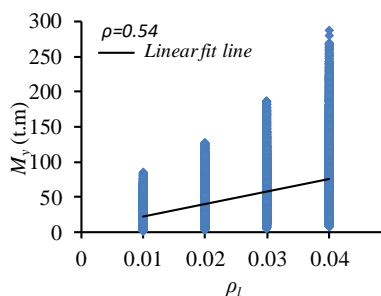


Fig. 4 Relation of ρ_l and M_y for all RC beams

During the evaluation of sectional attributes on the moment capacities of unsymmetrically RC sections, effect of mechanical reinforcement ratio is not considered. For this reason, effect of mechanical reinforcement ratio (w'/w) on the flexural strength capacity (M_y) of the members is investigated separately. In Fig. 5, relation between w'/w and M_y is plotted for distinct steel grade types and the extreme values of longitudinal reinforcement ratio, respectively. In general, it can be said that moment capacities of RC sections are inversely proportional to mechanical reinforcement ratios and relation is likely exponential between these two parameters. It can be also told that effect of steel grade type is not apparent on the relation. However, relation between these parameters significantly declines with increasing longitudinal reinforcement ratio.

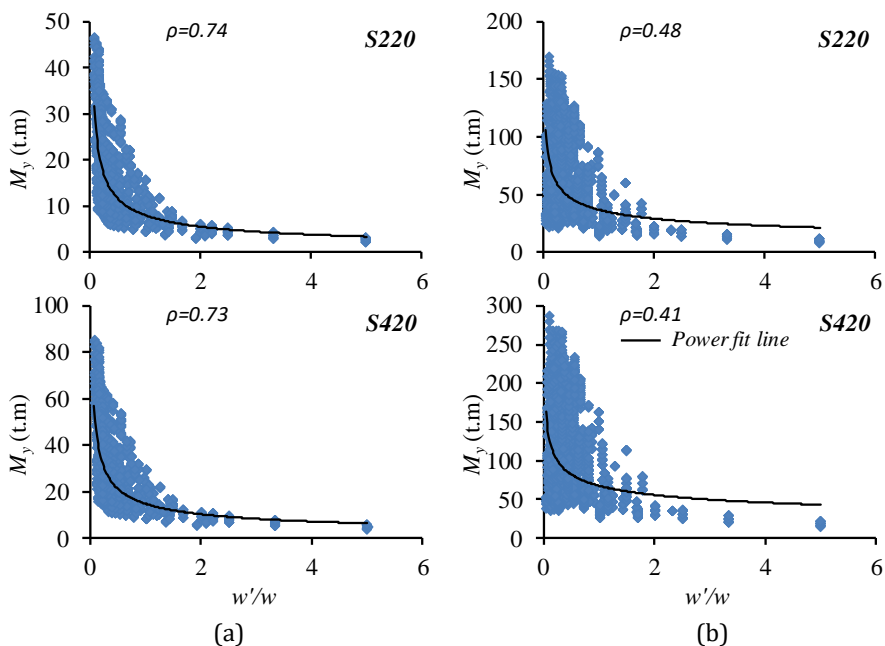


Fig. 5 Relation between w'/w and M_y (a: $\rho_l=1\%$, b: $\rho_l=4\%$)

It was realized in statistical evaluations that A_s'/A_s ratio has important contribution on moment capacities of unsymmetrically RC members. A_s'/A_s describes the ratio of extreme compression longitudinal reinforcement to extreme tension longitudinal reinforcement area (note that web longitudinal reinforcement is not included). For this reason, relation between A_s'/A_s and M_y is also studied to make further investigation. In Fig. 6, effect of distinct longitudinal reinforcement ratios is shown in different columns and steel grade types are illustrated in two rows to investigate correlation between A_s'/A_s and M_y . By this way, combined effects are explored. In addition, effect of extreme values of section dimension ratios (H/B) is included to make detailed assessment. It can be seen from the figure that longitudinal reinforcement ratio significantly affects the trend of moment capacities.

It can be admitted that high longitudinal reinforcement ratios dramatically influenced the relation between A_s'/A_s and M_y . Hence, A_s'/A_s becomes distinguishing parameter for high longitudinal reinforcement ratio. For A_s'/A_s values lower than one, moment capacity of RC sections is increasing with increasing A_s'/A_s . However, this situation is reversed if A_s'/A_s is higher than one. Nevertheless, it can be told that relation between A_s'/A_s and M_y seems more promising than relation between w'/w and M_y in general. In addition, when the distribution of w'/w and A_s'/A_s with M_y is compared, it can clearly be said that distribution of w'/w is much more dispersed and this situation is an important obstacle for the definition of prediction equation.

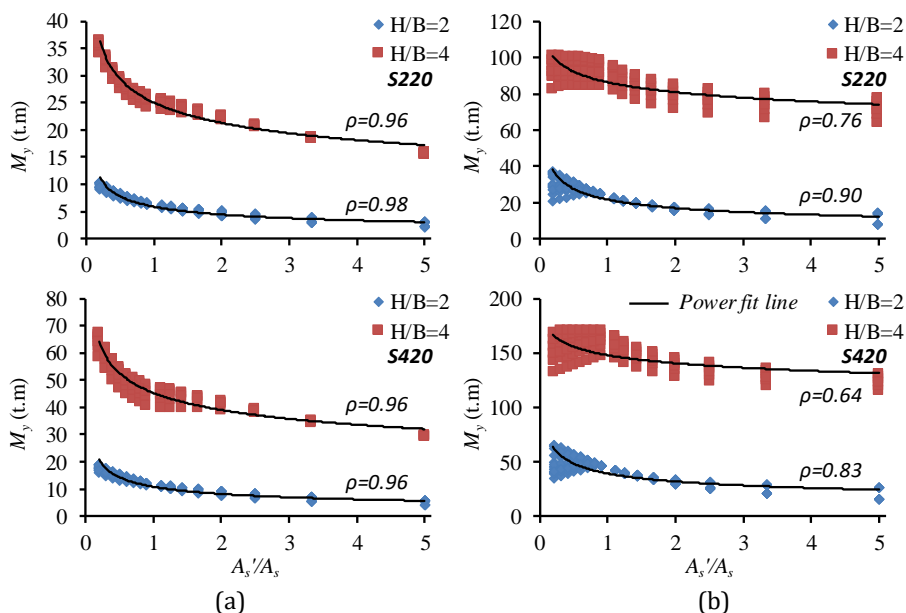


Fig. 6 Relation of A_s'/A_s and M_y (a: $\rho_l = 1\%$, b: $\rho_l = 4\%$)

4. Mathematical Expression for Unsymmetrically RC Member Responses at Yield

During the development of mathematical equations, it was aimed to involve all parameters (e.g. strength of materials, section dimensions, amount of reinforcement ratio and etc.) as much as possible which primarily affect the strength and deformation capacity of members. By this way, possibility of changes in section dimensions or strain and/or strength of materials due to exposure of corrosion, moisture and other related issues which in long term dramatically influence behavior of materials and hence the strength and deformation capacity of members are taken into account. Investigations in Section 3 have also revealed that BH^2 , ρ_l , yield strength of reinforcement (f_y) and A_s'/A_s have primary contribution on the flexural strength of unsymmetrically RC members. It should be reminded that during the evaluations for the determination of these parameters, the full bond mechanism between concrete and reinforcement is assumed and also it is accepted that longitudinal reinforcement bars are homogeneously distributed along the section.

After determination of parameters, statistical evaluations were made to finalize the equation using nonlinear optimization algorithm: generalized reduced gradient (GRG) algorithm via Excel spreadsheet solver. During the iteration process, it was aimed to minimize the variation between predictions and actual data. In addition, it was assumed that predicted/actual values are normally distributed and exceedance probability of both tails in the distribution was limited to 5%. In other words, the constraint was used to enforce prediction equation to estimate value that falls in 90% occurrence probability of actual data. Consequently, equations and their multipliers are determined considering all constraints (limitations). Consequently, mathematical expression for flexural strength capacity (M_y) of unsymmetrically RC beams suggested in this study is given in Eq. (1).

$$M_y = \left(60 \frac{f_y}{220}\right) BH^2 \rho_l^{0.9} \left(\frac{A_s'}{A_s}\right)^\alpha (N - mm) \tag{1}$$

Notation of α is described to distinguish ratio of compression and tension reinforcement. If A_s'/A_s is higher than one, then α is equal to -0.3 and -0.1 if vice versa. The most advantageous aspect of the equation is that it is direct, simple and appropriate to spreadsheet applications. Since it considers the most important and very easily determined parameters, it can be used in practical to estimate moment capacities. Although generalized rules are applied for the construction of RC members, Eq. (1) neglects the effect of depth of concrete cover on flexural strength capacity.

It is also worth to remind that Eq. (2) is used in prediction of flexural strength capacity of RC beams for approximate estimations especially in design phase of RC structures. In the equation, A_s , d and d' is the tensile longitudinal reinforcement area, section height minus concrete cover and concrete cover, respectively. Concrete cover here is described as distance from the extreme fiber to center of longitudinal reinforcement bar. It should be noted that the most important deficiency of this equation is that it neglects the difference between the moment capacities of beams having the same reinforcement area but different beam widths. In the study, moment capacities obtained according to Eq. (1) and Eq. (2) is also compared with moment capacities determined from moment-curvature analysis in forthcoming section, separately.

$$M_y = A_s f_y (d - d') \quad (2)$$

Curvature is another parameter to describe unsymmetrically RC beam responses at yield. According to Priestley et al. [10] yield curvature is the K times of the proportion of yield strain of longitudinal reinforcement (ϵ_{sy}) to section height. K is the coefficient value that depends on geometric features and structural member type such as beam or column. However, Palanci [4] stressed the high dispersion of this expression and stressed that Priestley et al. [10] expression may lead to overestimate yield capacities especially with increasing axial load ratio (ν). Accordingly, yield curvature capacity of RC sections is calculated by Eq. (3) suggested by Palanci [4]. Statistical evaluations performed by Palanci [4] have shown that yield curvature depends on the axial load level and longitudinal reinforcement ratio of members. In addition, the relation between these parameters and yield curvature was described in polynomial function. Using the appropriate function curve with spreadsheet solver, Eq. (3) is finally provided. In the equation, axial load ratio (ν) can be assumed zero for both symmetrically and unsymmetrically RC beams and Eq. (3) can be calculated accordingly.

$$\phi_y = 2.0 \frac{\epsilon_{sy}}{H} [-2.75(\nu)^2 + 1.30(\nu) + 0.90] [5.50\rho_l + 0.90] \quad (3)$$

The pros of Eq. (3) are it is applicable to variety of members such as beams and columns and it is very practical to estimate yield curvature. However, equation is just valid for square or rectangular RC sections.

Consequently, flowchart for the application of mathematical expressions to determine flexural strength and yield curvature capacity of unsymmetrically RC members can be followed by Fig. 7. In the figure, details about calculation of parameters for each step are clearly shown. It should be reminded that H describes the section dimension parallel to earthquake (i.e. seismic force or excitation) direction.

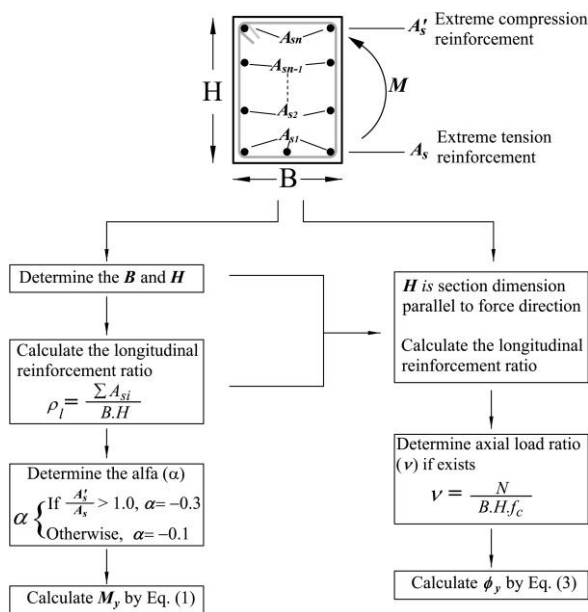


Fig. 7 Flowchart for the calculation of M_y and ϕ_y

4.1. Comparison of Prediction Equations with Sectional Responses

In Fig. 8, correlation between Eq. (1) and $m-\phi$ results and distribution of $M_{y,Eq.(1)}/M_{y,m-\phi}$ ratios are plotted. In order to make statistical evaluations some salient statistical parameters such as mean, median and coefficient of variation (CoV) is also provided. Comparison of mean and median values might be useful when the CoV is high. Furthermore, it can be said that close relation between the mean and median values emphasises the reliability of predictions.

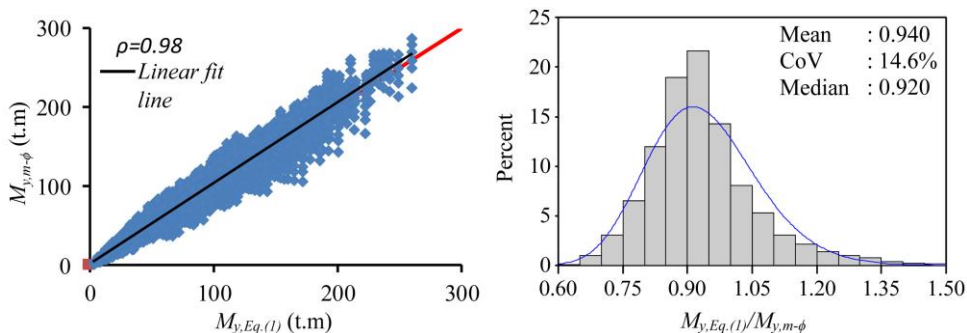


Fig. 8 Comparison of flexural strength determined from $m-\phi$ analysis and Eq. (1)

It can be understood from the Fig. 8 that correlation coefficient is very high (0.98) between $m-\phi$ analysis and Eq. (1) results. It can also be seen that mean (0.94) and median (0.92) values of $M_{y,Eq.(1)}/M_{y,m-\phi}$ ratio is very close to each other. Comparisons clearly have shown that proposed equations highly satisfactory to express the moment capacities of unsymmetrically RC beams at yield. The CoV (0.146) of $M_{y,Eq.(1)}/M_{y,m-\phi}$ is also very low and this situation is also another indicator of reliable estimations.

In Fig. 9, Eq. (2) predictions and $m-\phi$ results are also compared using mean, median and CoV parameters. It can clearly be viewed from the Fig. 9 that Eq. 2 mostly underestimates

(0.59) the moment capacity of RC beams. Difference is around 41% and this endangers the reliability of equation. Comparison of $M_{y,Eq.(2)}$ and $M_{y,m-\phi}$ results is also manifest the dispersion of results and thus CoV of $M_{y,Eq.(2)}/M_{y,m-\phi}$ is very high (40%). One may think that prediction of Eq. (2) may be improved when the steel grade type and longitudinal reinforcement ratios are separately investigated. For this purpose, correlation coefficient, CoV and $M_{y,Eq.(2)}/M_{y,m-\phi}$ are studied for each ρ_l and steel grade type. Results have indicated that relation of $M_{y,Eq.(2)}$ and $M_{y,m-\phi}$ is fluctuated and CoV is generally higher than 30%.

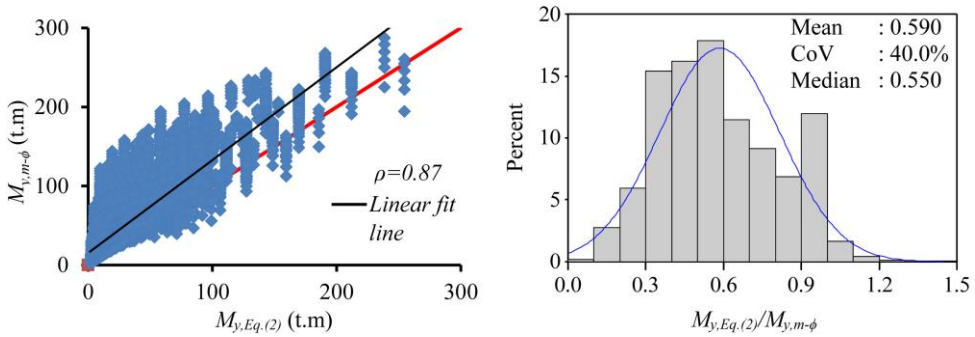


Fig. 9 Comparison of flexural strength determined from $m-\phi$ analysis and Eq. (2)

4.2. Estimation of Dynamic Characteristics of MDOF Buildings Using Prediction Equations

In order to study efficiency of provided equations, vibration periods which reflect the dynamic features of the structure of two experimental MDOF buildings are predicted. For this purpose, cracked stiffness of beams and columns in MDOF buildings are calculated by Eq. (4). In the equation, M_y , θ_y and L_s describe the mean yield strength and chord rotation capacity at the both ends and shear span length of the member, respectively. Chord rotation capacities can also be calculated by Eq. (5). In the equation, d_b is the (mean) diameter of the tension reinforcement. During the calculations for experimental buildings, M_y and ϕ_y values are obtained by Eq. (1) and Eq. (3) and then cracked stiffness of symmetrically and unsymmetrically RC members are calculated via Eqs. (4) and (5). The reader is referred to see Palanci [4, 11] for flexural strength capacity of ordinary RC columns. Calculated cracked stiffness values were then implemented to analytical models and dynamic features of models were obtained to compare with experimental MDOF building results.

$$EI_{eff} = \frac{M_y L_s}{3\theta_y} \tag{4}$$

$$\theta_y = \frac{\phi_y L_s}{3} + 0.0013 \left(1 + 1.5 \frac{H}{L_s} \right) + 0.13 \phi_y \frac{d_b f_y}{\sqrt{f_c}} \tag{5}$$

Provided equations are first practiced on full-scale, 2D four-story ICONS bare frame. The frame was produced to reflect construction practices used in southern European countries in the 1950's and it was tested at the ELSA laboratory (Joint Research Centre, Ispra). Further information about the ICONS can be found in Pinho and Elnashai [12] and Varum [13]. Structural model of the experimental building is prepared using SAP2000 [14] and shown in Fig. 10. It can be seen from the figure that model consists of a three-bay RC frame with varying lengths, but all stories have identical (2.70m) story height. Further information about the sectional attributes of the RC members can be found from Varum [13].

Experimental bare frame was tested under earthquake levels that have returned periods of 475 and 975 years. It was observed during the tests that significant damage, such as full-width cracks or concrete spalling, is not observed [12]. In addition, Pinho and Elnashai [12] carried out non-linear dynamic analysis of frame model and they pointed out that building behaved satisfactory under input motion that have return period of 475 years although local hinging is recorded. However, high level of damage is stressed under return period of 975 years at different stories of building due to large deformation demand of strong-column. According to analytical analysis results of Pinho and Elnashai [12], dominant (first) inelastic vibration period of the building is 1.1s and 1.4s for return periods of 475 and 975 years. Considering the numerical and experimental test results [12, 13], it can be assumed that inelastic vibration of the building is likely to be somewhere close to the return period of 975 years results. For this purpose, first 4 equivalent modal frequency of bare frame provided by Varum [13] from the test for the return period of 975 years is determined approximately. Accordingly, first 4 equivalent modal frequency of bare frame is approximated 0.7Hz (1.43s), 2.18Hz (0.46s), 3.06Hz (0.33s) and 6.76Hz (0.15s), respectively. It is worth to note that determined frequencies approximately correspond to 0.75% of roof drift ratio and dominant period approximated from the test results is also very close to inelastic period of Pinho and Elnashai [12].

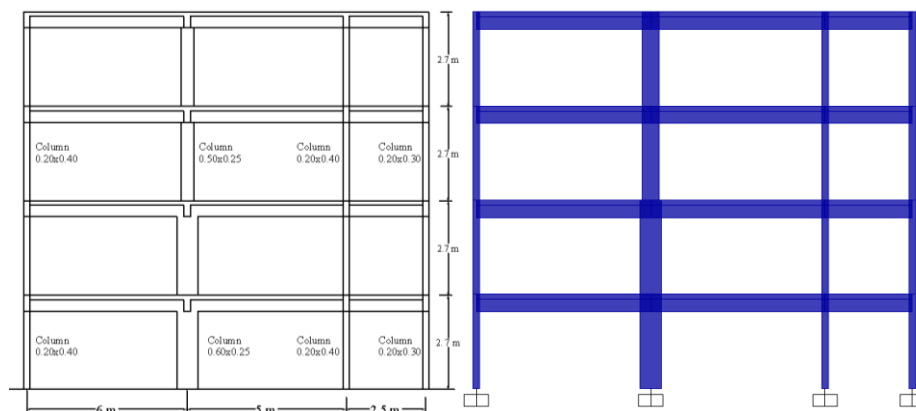


Fig. 10 Building elevation of ICONS RC bare frame and 2D analysis model

After implementation of cracked stiffness of members to bare frame, first 4 natural vibration period of the building is also obtained from 2D analytical model shown in Fig. 10 using prediction equations. Obtained values are given in Table 2 with experimental test results for comparison purposes. It can be seen from the table that analytical model periods are very close to results of experimental test results. Difference between the dominant periods is lower than 1%. It seems that differences are increasing at high modes but it is still an acceptable range and it can be admitted that analytical model results have very good agreement with test results.

Second practice is also made again on three-story, three-dimensional RC building also called the SPEAR building (see Fig. 11). The test building was designed only for gravity loads without earthquake resistance to represent older construction in Southern European Countries. Further details about the SPEAR test building procedure and construction, mechanical features of the building materials and reinforcement details can be found in Jeong and Elnashai [15], Mola et al. [16], Molina et al. [17] and Negro et al. [18].

Table 2 Comparison of first 4 natural vibration periods of analytical model and ICONS bare frame

	1 st period (s)	2 nd period (s)	3 th period (s)	4 th period (s)
ICONS Test	1.43	0.46	0.33	0.15
This study	1.44	0.48	0.28	0.19
Difference (%)	0.70	4.35	17.86	26.67

It can be seen from the figure that building is irregular in plan but story height of each floor is same (3m) which can be said regular in height. Section dimension of RC columns is mainly 0.25 x 0.25 m except that one RC column is 0.25 x 0.75 per floor and RC beams are identical (0.25 x 0.50 m). The test building was subjected to PGA levels of 0.02g and 0.15g which can be described as low and high level of excitations along two orthogonal directions (i.e. bi-directional excitations) and general engineering demand parameters (EDP) such as displacement history of floors, member internal forces and deformations were recorded in time domain. The test results of experimental building are provided in many studies [18-20] including modal characteristics of building.

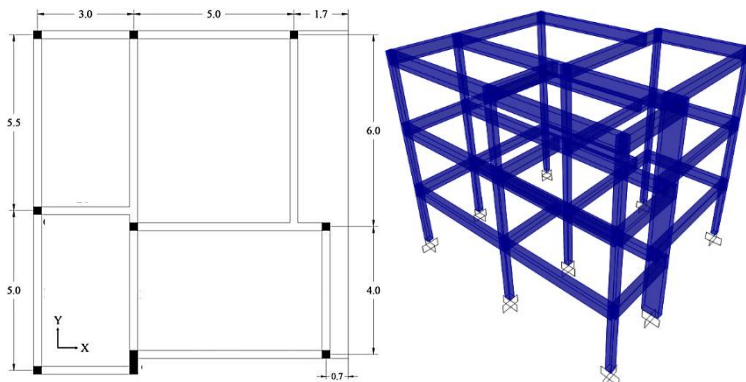


Fig. 11 Plan view (Left) and 3D structural model (Right) of three-story SPEAR building (Units in meter)

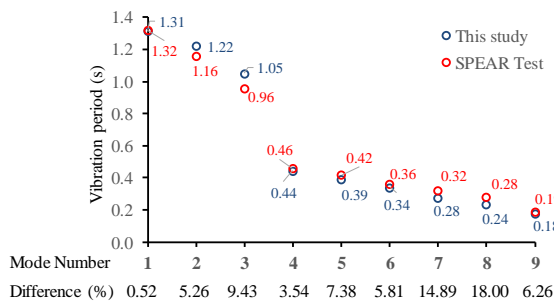


Fig. 12 Comparison of 3D analytical and experimental modal analysis results for 0.15g test

In order to make comparison of modal characteristics of test building, 3D view of analytical model is prepared by SAP2000 [14] as shown in Fig. 11 (right) and cracked stiffness of structural members are determined under provided sectional features of the members. Obtained member stiffness values are implemented building and compared

with test results for high level (0.15g) excitation (see Fig. 12). Selection of this level is based on the study of Avsar et al. [21] since they stress that member response is far from the section yield level and cracking of members are limited. Analytical model results and tests results are compared for 9 mode shapes of the building and percent difference between them is also shown in the figure. Comparisons clearly show very good fit between the results which, in other words, reveals the reliability of proposed equations.

5. Conclusions

In this study, prediction equations are provided to estimate cracked stiffness and hence the flexural strength capacity of unsymmetrically RC members at yield. For this purpose, wide range of section dimensions, material types, reinforcement ratios and configurations are covered, analyzed and statistically evaluated. Influence of parameters on the response of unsymmetrically RC members is investigated and implemented to prediction equations by extensive statistical treatments. Prediction equations are first tested with individual sections analytical RC section results and comparisons have shown very good agreement. In addition, mode shapes (periods) that represent the dynamic characteristics of full scale two experimental building is projected by using prediction equations. Comparisons have also shown that dynamic characteristics of the analytical models which stiffness of the members formed by provided equations have very good matching with experimental building results. Furthermore, it can be admitted that provided equations are capable of approximation of responses in building scale. Consequently, it can be said that results of this study have proved that proposed equations can be used to determine flexural strength and stiffness of unsymmetrically reinforced members reliably. Some important implications of the study can be expressed as follows:

- Statistical evaluations have shown that combination of section dimension (BH^2) is more promising in determination of relation between M_y than that of individual dimensions.
- It is observed that mechanical reinforcement ratio (w'/w) which includes the web reinforcement is inversely proportional to moment capacities of RC sections and relation is exponential. It can also be said that correlation between ratio of compression reinforcement to tension reinforcement (A_s'/A_s) and M_y is higher than w'/w .
- BH^2 , longitudinal reinforcement ratio (ρ_l), yield strength capacity of reinforcement (f_y) and A_s'/A_s are found adequate to express flexural capacity of unsymmetrically reinforced concrete members.
- It can be expressed that proposed equations can be used with numerical and analytical approaches proposed for symmetrically RC members to predict dynamic response of real buildings.

References

- [1] Chandrasekaran S, Nunziante L, Serino G and Carannante F. Curvature Ductility of RC Sections Based on Eurocode: Analytical Procedure. KSCE J Civ Eng. 2011; 15(1): 131 – 144. <https://doi.org/10.1007/s12205-011-0729-4>
- [2] Colajanni P, Fossetti M and Papia M. An Analytical Step-by-Step Procedure to Derive the Flexural Response of RC Sections in Compression. Advances in Civil Engineering. 2013; Article ID 275657: 1-13. <http://dx.doi.org/10.1155/2013/275657>
- [3] Naderpour, H. and Mirrashid, M. Moment capacity estimation of spirally reinforced concrete columns using ANFIS. Complex and Intelligent Systems. 2019. <https://doi.org/10.1007/s40747-019-00118-2>

- [4] Palanci, M. Flexural response prediction of reinforced concrete members based on statistical observations. *Arabian Journal for Science and Engineering*. 2017; 42(9): 3689-3709. <https://doi.org/10.1007/s13369-016-2392-z>
- [5] Panagiotakos TB, Fardis MN. Deformations of reinforced concrete members at yielding and ultimate. *ACI Structural Journal*. 2001; 98: 135-148. <https://doi.org/10.14359/10181>
- [6] Eurocode 8. Design provisions for earthquake resistance of structures, Part 3: Assessment and retrofitting of buildings. European Committee for Standardization, Brussels; 2003
- [7] TBEC. Turkish Building Earthquake Code, Disaster and Emergency Management Presidency, Ankara; 2018.
- [8] Scott BD, Park R and Priestley MJN. Stress-strain behavior of concrete confined by overlapping hoops at low and high strain rates, *ACI J*. 1982; 79(1): 13-27. <https://doi.org/10.14359/10875>
- [9] Mander J. (1984). Seismic design of bridge piers. Ph.D. Dissertation, University of Canterbury, New Zealand.
- [10] Priestley MJN, Calvi GM, Kowalsky MJ. Displacement Based Seismic Design of Structures. IUSS Press, Pavia, 2007.
- [11] Palanci, M. Flexural Strength Estimation of Ordinary Rectangular Reinforced Concrete Sections. Proceedings of the 3th International Conference on Civil and Environmental Engineering, Çeşme, Paper No. 387, 2018.
- [12] Pinho R and Elnashai AS. Dynamic collapse testing of a full-scale four storey RC frame, *ISCTE Journal of Earthquake Technology*. 2000; 37(4): 143-164.
- [13] Varum H. (2003). Seismic Assessment, Strengthening and Repair of Existing Buildings. Ph.D. Dissertation, University of Aveiro, Portugal.
- [14] SAP2000, Integrated finite element analysis and design of structures basic analysis reference manual. Computers and Structures Inc., Berkeley, California (USA).
- [15] Jeong SH, Elnashai AS. Analytical assessment of an irregular RC full scale 3D test structure, Mid-America Earthquake Centre, (MAE) Report, University of Illinois at Urbana-Champaign, CD Release 04-03, USA, 2004.
- [16] Mola E, Negro P, Pinto AV. Evaluation of current approaches for the analysis and design of multi-storey torsionally unbalanced frames, Proc. of 13th World Conference on Earthquake Engineering, Vancouver, Paper No. 3304, 2004.
- [17] Molina FJ, Buchet Ph, Magonette GE, Hubert O, Negro P. Bidirectional pseudo dynamic technique for testing a three-storey reinforced concrete building. Proceedings of the 13th World Conference on Earthquake Engineering, Vancouver, Paper No. 75, 2004.
- [18] Negro P, Mola E, Molina FJ, Magonette GE. Full-scale PSD testing of a torsionally unbalanced three-storey non-seismic RC frame. Proceedings of the 13th World Conference on Earthquake Engineering, Vancouver, Paper No. 968, 2004.
- [19] Fardis MN and Negro P. SPEAR – Seismic performance assessment and rehabilitation of existing buildings”, Proceedings of the International Workshop on the SPEAR Project, Ispra, 2006.
- [20] Jeong SH, Elnashai AS. Analytical assessment of an irregular RC frame for full-scale 3D pseudo-dynamic testing: part II- condition assessment and test deployment. *Journal of Earthquake Engineering*. 2005; 9(2): 265-284. <https://doi.org/10.1080/13632460509350535>
- [21] Avsar Ö, Bayhan B and Yakut A. Effective flexural rigidities for ordinary reinforced concrete columns and beams. *The Structural Design of Tall and Special Buildings*. 2014; 23(6): 463-482. <https://doi.org/10.1002/tal.1056>



ResearchArticle

Band gap modification of spray pyrolysed ZnS films by doping and thermal annealing

Serço Serkis Yeşilkaya^{1,a}, Ünzile Ulutaş^{*1,b}

Department of Physics, Yıldız Technical University, İstanbul, Turkey

Article Info

Article history:

Received 30 Jan 2019

Revised 29 July 2019

Accepted 2 Sep 2019

Keywords:

ZnS;

Spray pyrolysis;

Band gap energy;

Doping

Abstract

ZnS thin films are widely used in solar cells as window material. Optical and electrical properties of the films such as band gap energy and resistivity directly affect device performance. In this work it was shown that properties of ZnS films can be changed by doping and thermal annealing. Therefore, films with convenient parameters can be chosen for the fabrication of any device. ZnS films were fabricated by spray pyrolysis technique. Zinc chloride and thiourea used as sources of Zn and S respectively. Films were grown on 350°C hot substrates. Furthermore 1, 5, 10, 15 % doped films prepared by addition of boric acid into the solution. Structural, optical and electrical properties of the films were examined by SEM, XRD, optical transmission and resistivity measurements. Later on all films annealed in air at 350°C for 30 min. All measurements were done also for annealed films. Effects of doping and thermal annealing on the band gap energy and resistivity of the films were shown. Band gap energies of the films were between 3.37-3.82 eV and surface resistivities were between 257.2-12.5 MΩ.

© 2019 MIM Research Group. All rights reserved.

1. Introduction

ZnS thin films are often used as window material in solar cells. The optical and electrical properties of the films, such as the band gap energy range and resistance, directly affect device performance. In this study, it has been shown that the properties of ZnS film can be changed by adding and annealing. This allows the selection of films with suitable parameters for the device to be planned.

ZnS is one of the most important wide band gap semiconductor materials for electronic device applications. It is commercially used in photovoltaic, phosphorescence and thin film electroluminescence devices [1–2]. Luminescent properties of impurity doped ZnS nano crystals are significantly different from the properties of undoped ZnS[6]. Optimization of film parameters directly affects the device performance. Caiying Mao et al. were grown boron doped ZnO (BZO) films with 0 to 6 % doping concentrations by RF magnetron sputtering technique on quartz substrates. They stated that crystalline quality of the films gets worse over 4% doping concentrations. They found that band gap energy of BZO films increases to 3.57 eV from 3.28 eV with increase of Boron concentration from 0 to 6% and minimum resistivity was obtained for 2% B doping as 1.58.10⁻³ (Ω cm) [4]. The resistivity of the film is particularly important in application of transparent conductive oxide in photovoltaics. Low resistivity promotes energy-conversion efficiency owing to improved

*Corresponding author: unzileulutas@gmail.com

^aorcid.org/0000-0001-5441-2439; ^borcid.org/0000-0001-7964-2919

DOI: <http://dx.doi.org/10.17515/resm2019.104ma0130>

Res. Eng. Struct. Mat. Vol. 6 Iss. 2 (2020) 119-126

photo current [10]. Karakaya et.al. [5] fabricated ZnO:B films by ultrasonic spray pyrolysis method due to low cost and simplicity. They showed that films were polycrystalline structured and oriented in [002] direction. They also found that increasing B concentration was lead to a decrease in crystalline quality of the ZnO films. Optical transmission of the films was higher than 80% for visible region. Resistivity of the films were decreased from $1.87 \times 10^{-2} \Omega \text{cm}$ to $2.40 \times 10^{-3} \Omega \text{cm}$. Band gap energies were increased to 3.30 eV from 3.25 eV while boron concentration was increasing to 5% from 1%. According to these results B-doped ZnO is a promising material for photovoltaic solar cells [5]. Some research showed that doped nano crystalline semiconductors are a new class of materials which can be used in imaging, lighting, sensors and lasers [7-8]. Rajendra S. Gaikwad et al. found in their study that sprayed ZnO thin films revealed >95% transmittance in the visible wavelength range, $1.956 \times 10^{-4} \Omega \text{cm}$ electrical resistivity, $46 \text{ cm}^2/\text{V.s}$ Hall mobility and $9.21 \times 10^{21} \text{ cm}^{-3}$ charge carrier concentration. The X-ray photoelectron spectroscopy study has confirmed 0.15 eV binding energy change for Zn 2p_{3/2} when 2 at% boron content is mixed without altering electro-optical properties substantially. Finally, using soft modeling importance of these textured ZnO over non-textured films for enhancing the solar cells performance is explored. Due to decrease in grain size after boron doping hydrophilicity was decreased. One can use these highly conducting, transparent, high surface roughness and self-textured Zn_{1-x}B_xO films, as a transparent conducting working electrode, in solar cells by assuming most of the incident solar radiation will be scattered and thereby, the solar cell efficiency will be improved [9].

Upon doping a semiconductor, impurity states are created which could appear either within its gap or outside of it. If the impurity states are formed within the energy range of the energy gap, this will cause its reduction and most probably will shift the Fermi energy, E_f , into the impurity bands. On the other hand, if the impurity states are created outside the gap, it is expected that they will not affect the gap value in an appreciable way. The gap problem, thus, turns to be the problem of finding the appropriate dopant(s) which can reduce the energy gap of the wide band gap materials [12].

Abdelhak Jrad and friends have deposited indium-doped zinc sulfide (ZnS:In) thin films by chemical bath deposition technique (CBD). The structural properties studied by X-ray diffraction indicate that ZnS:In has a cubic structure with an average crystallite size 4.7–11.0 nm. Transmission and reflection spectra reveal the presence of interference fringes indicating thickness uniformity and surface homogeneity of deposited material. All the films were transparent in the visible and infrared regions (P60%), which allows us to use this material as an optical window or a buffer layer in solar cells. The obtained band gap energy E_g is in the range of 3.70–3.76 eV [13].

II-VI semiconductor nano structures are of great interest due to their morphology and possible variety of applications. Band gap energy is an important parameter for these applications. Among all II-VI compounds ZnS one which has very large band gap. ZnS can be in two different crystalline structure, zinc blend with $E_g=3.72 \text{ eV}$ and wurtzite with $E_g=3.77 \text{ eV}$. Because of these properties ZnS becomes a similar material to ZnO in UV based devices [1].

In this work we fabricated boron doped ZnS films for the first time using easy and cost-effective spray pyrolysis technique. Since all parameters are kept constant and only boron is added to ZnS solution, we think that films are doping with boron.

2.Experimental

0.05M ZnS solution was prepared by adding 1.74 g ZnCl₂ and 0.953 g thiourea (CH₄N₂S) into 500 ml distilled water at room temperature. ZnS films were grown on 26 mm×15 mm×2 mm glass substrates. Substrates cleaned by detergent, distilled water, alcohol and

again distilled water respectively. ZnS films were grown by spray pyrolysis on the 400°C hot substrates with a spraying rate of 1/3 spray/s. 1, 5, 10 and 15% boron doped ZnS films obtained. Boric acid used as boron source. Films were annealed at 350°C in oven. Transmission spectra of films were measured by Lambda 2 Perkin Elmer UV spectrophotometer in 320-1100 nm wavelength range. Direct band gap energy of the films were calculated by equation 1 [3] according to absorption spectra obtained from transmission spectra of the films.

$$\alpha^2 = \frac{B(h\nu - E_g)}{(h\nu)^2} \tag{1}$$

In the eq.1 α is absorption coefficient, E_g band gap energy, $h\nu$ photon energy and B is constant. The extrapolation of the straight line to $h\nu$ axis at $(\alpha h\nu)^2=0$ on the plot of $(\alpha h\nu)^2$ versus $h\nu$ gives the value of energy band gap (E_g).

In this study; the thickness of ZnS thin films formed on glass substrates was calculated by weighing method. In this method, after the necessary cleaning of the glass mats, a group of glass mats to be filmed were weighed with an electronic balance of 10^{-4} grams. After the film was formed on the glass mats, weighing was performed again. The difference between these two weighing results gave us the mass of the films. Subsequently, the dimensions of all film coated glasses were determined and their surface areas were calculated. Since we are not sure the homogeneity of the films, the average film thickness was calculated on 5 or more samples instead of a single sample. Thus, the average thickness of ZnS thin films;

$$d = \frac{\Delta m}{S \cdot \rho_{film}} \tag{2}$$

calculated with the formula (2). In this equation, Δm is the mass of the film, S is the total surface area of the films, ρ is the density of the film, and d is the average film thickness. The average thickness of the obtained ZnS thin films was calculated as 5.05 μm .

The crystalline structures of ZnS thin films which were annealed at different temperatures were analyzed using X-ray diffraction (XRD, Panalytical Diffractometer Philips) with $\text{Cu K}\alpha$ radiation ($\lambda=1.54056 \text{ \AA}$) in the range of $5^\circ-80^\circ$. The lattice constants of the ZnS thin films with wurtzite phase structure were calculated from Eq. (3). Debye-Scherrer's Formula given in Eq. (4) was used for estimating the average crystallites of the thin films. The dislocation density (δ) given in Eq. (5) Williamson and Smallman's formula, which is related to the dislocation lines per unit area in the film, was estimated using the average of the grain size (D) [11].

$$\frac{1}{d^2} = \frac{4}{3} \frac{(h^2 + hk + k^2)}{a^2} + \frac{l^2}{c^2} \tag{3}$$

$$D = \frac{K\lambda}{\beta \cos\theta} \tag{4}$$

$$\delta = \frac{\text{lines}}{D^2 m^2} \tag{5}$$

Where in the Eq. (3), a and c are the lattice constants, d is the distance between adjacent lattice planes and (hkl) is Miller indices. Where in the Eq. (4), D is the crystal size, K is the constant shape factor (0.9), λ is the wavelength of X-ray radiation source, θ is the diffraction angle and β is the full width at half maximum of the prominent peak in radian.

3. Results

FEI-Quanta FEG 250 scanning electron microscopy was used to observe the surface morphologies of the ZnS films. SEM analysis was applied to the films. Small particle size differences were seen in particle sizes of doped and undoped films. It can be seen from Figure 1 that doped films has a little bit larger particle size comparing to the undoped one.

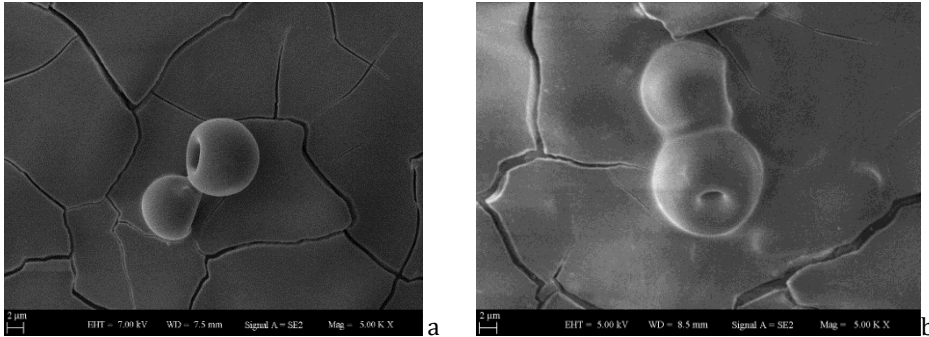


Fig. 1 SEM images of a) non-doped and b) 15% boron doped ZnS films.

X-ray diffractograms of the films prepared with different boron doping are shown in Figure (2 and 3). According to XRD results intensities of [111], [220] and [311] Zn peaks at 29° , 48° and 57° for 2θ were increased with boron doping and thermal annealing. Samples are amorphous at the lowest doping rate. The intensity of the reflection increased as the doping rate increased before any new reflection appeared. Thus, no other phase was formed, but only the crystallization of the formed phase was improved.

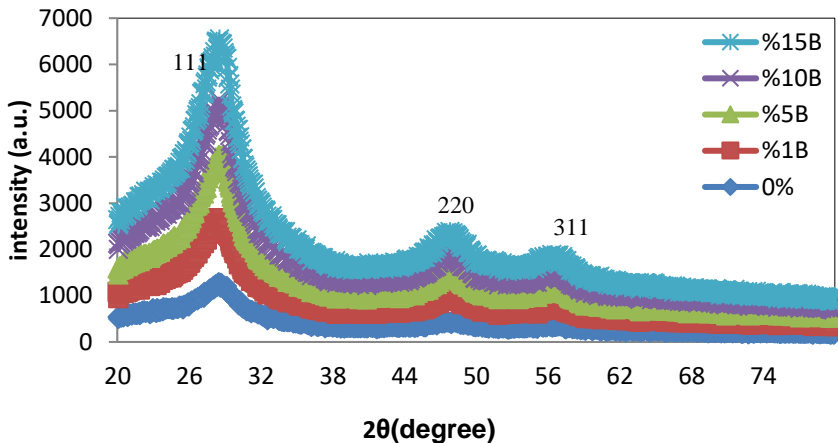


Fig. 2 XRD patterns of boron doped non-annealed ZnS films

A well-crystallized film was obtained with 15% boron doping. The phase identification revealed that only cubic ZnS was formed. Therefore, the preparation conditions of a given technique greatly affect not only the number of phases formed but also its microstructural properties such as crystallinity. These results are in agreement with Muraliet al.[14]. The crystallite size was measured using Debye Scherrer's formula [11].

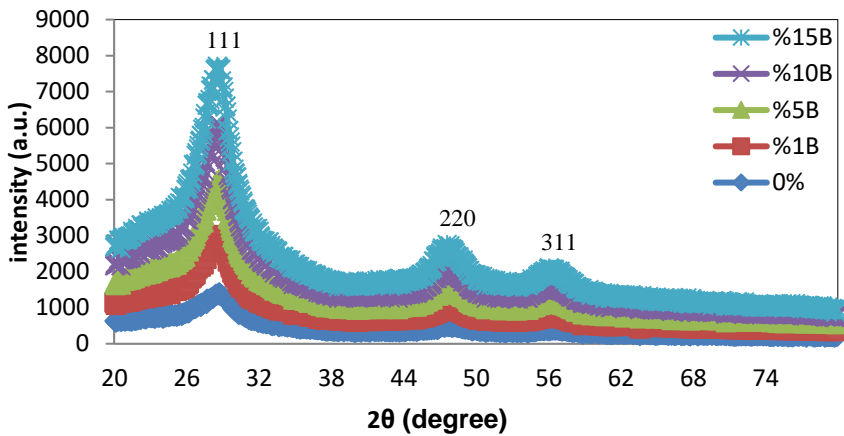


Fig. 3 XRD patterns of boron doped annealed ZnS films

Some differences observed in optical transmission spectra of ZnS films due to boron doping (Fig. 4 and 5). Band gap energies of the films were in the range of 3.37-3.82 eV (Fig. 6 and 7). This wide range is very important for different working requirements and design of optoelectronic devices. Band gap energy values of the films were given in table 1 according to boron doping and thermal annealing. An ohmmeter was used to measure the surface resistances of boron doped ZnS films and the measurements were made 10 times from 10 different locations of the films and the average resistance values were calculated. It was also seen that surface resistivity of annealed films were changed from 257.2MΩ to 86.3MΩ with boron doping while this change was from 189.5MΩ to 12.5MΩ for non-annealed films.

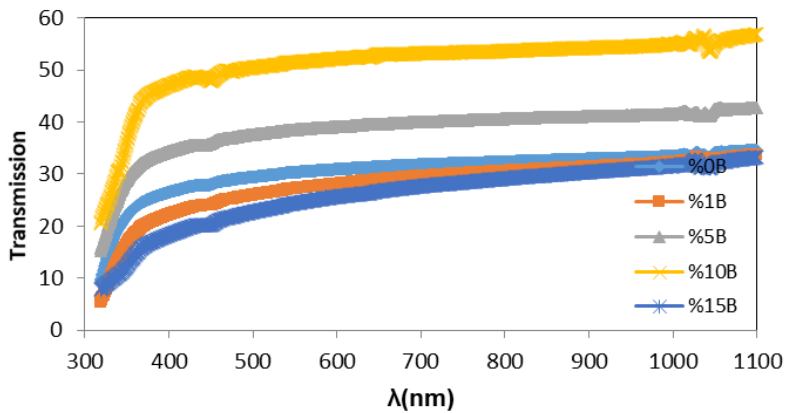


Fig. 4 Optical transmission spectra of boron doped non-annealed ZnS films.

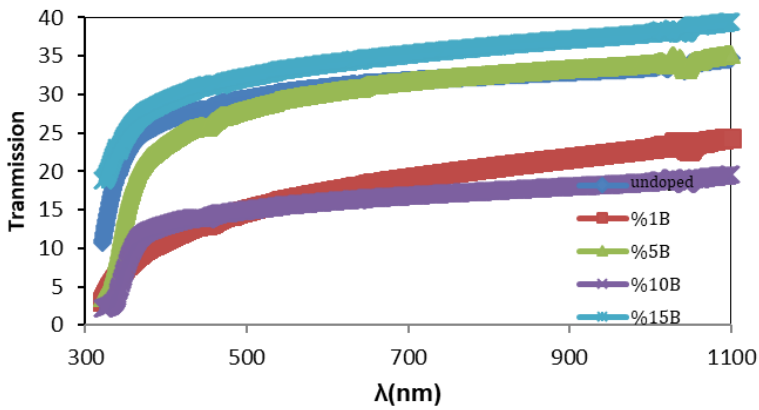


Fig. 5 Optical transmission spectra of boron doped annealed ZnS films.

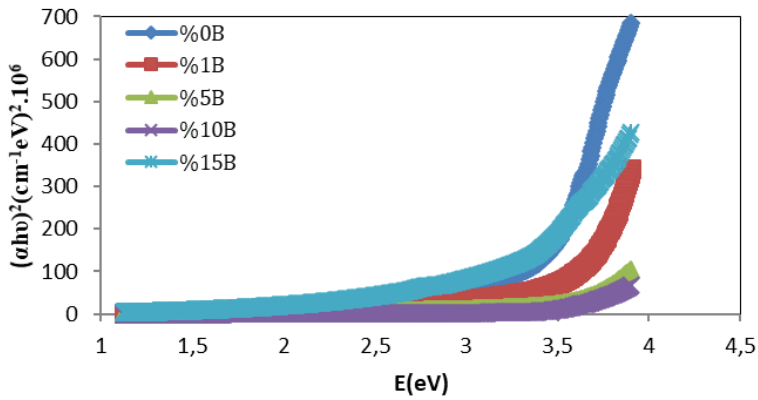


Fig. 6 Absorption spectra of boron doped non-annealed ZnS films.

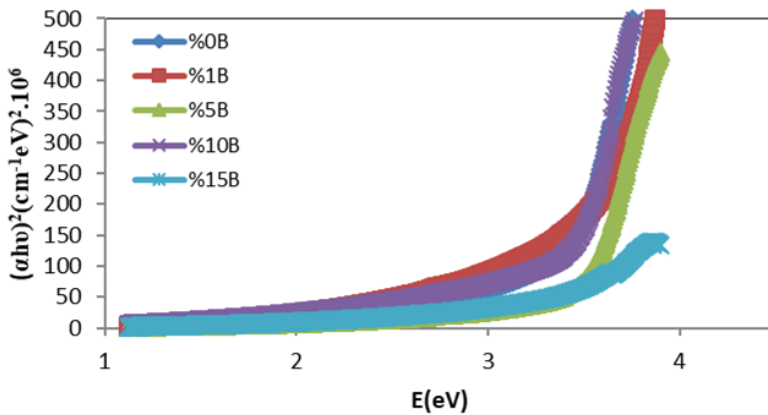


Fig. 7 Absorption spectra of boron doped annealed ZnS films.

Table 1 Band gap energy values of ZnS films.

ZnS(E_g)	Undoped	1% Boron	5%Boron	10%Boron	15%Boron
Non-annealed	3.48eV	3.62eV	3.63eV	3.73eV	3.82eV
Annealed	3.69eV	3.68eV	3.52eV	3.48eV	3.37eV

4. Conclusions

XRD results of the spray pyrolysed ZnS thin films showed that the positions of [111], [220] and [311] Zn peaks did not change by boron doping or thermal annealing. Furthermore, no new peak was seen in the spectra. Therefore, it can be concluded that no new phase was formed in film and compound remained as ZnS. More beneficiary, intensities of these XRD peaks were increased by boron doping and more increase was observed after thermal annealing. Band gap energy values of spray pyrolysed ZnS thin films were changed by boron doping and thermal annealing. Band gap widening in doped ZnS thin films can be attributed to the Burstein–Moss effect. According to mentioned effect Fermi level moves upward with increasing donor concentration. This also causes the shift of unoccupied levels in the conduction band. Therefore, the energy gap between the valence band and the conduction band widens and higher energies are needed for electrons to reach from the valence band to the shifted conduction band. Surface resistivity of the ZnS thin films were decreased with boron doping and also with thermal annealing which was a preferred result for increasing the performance of fabricated devices. Surface resistivity of annealed ZnS films were changed from 257.2M Ω to 86.3M Ω with boron doping while the change in surface resistivity was from 189.5M Ω to 12.5M Ω for doped but non annealed ZnS films. All results and obtained data show that it is possible to tune the band gap energy of ZnS thin films by boron doping and thermal annealing which are easy and cheap processes. In our doping range band gap energies of the ZnS thin films had a wide range of 3.37-3.82 eV. This wide range makes doped ZnS thin films applicable for fabrication of different optoelectronic devices such as sensors, solar cells, photodiodes etc. with different band gap requirements.

Acknowledgement

This work was supported by Yıldız Technical University Scientific Project Coordination with project no:2015-01-01-DOP01

We would like to thank to Dr. ÖzlemYağcı for her help on structural analysis of the films.

References

- [1] Ongul F, Ulutas U, Aydın Yüksel S, Yeşilkaya SS, Gunes S. Influences of annealing temperature and thickness on ZnS buffer layers for inverted hybrid solar cells, Synt. Met. 2016;220: 1-7. <https://doi.org/10.1016/j.synthmet.2016.05.017>
- [2] Senna YM, Effects of Mn+2 distribution in Cu-modified ZnS on the concentration quenching of electroluminescence brightness. Appl. Phys. Lett. 1995: 66;424-426. <https://doi.org/10.1063/1.114044>
- [3] Ghaffar MAR, Goudarzi A. Compositional, structural, and optical study of nano crystalline ZnS thin films prepared by a new chemical bath deposition route. Alloys&Comp. 2008: 466; 488-492. <https://doi.org/10.1016/j.jallcom.2007.11.127>
- [4] Mao C, Fang L, Zhang H, Li W, Wu F, Qin G., Ruan H, Kong C. Effect of B doping on optical, electrical properties and defects of ZnO films. Journal of Alloys and Compounds. 2016: 676; 135-141. <https://doi.org/10.1016/j.jallcom.2016.03.157>

- [5] Karakaya S, Özbas Ö. Boron doped nanostructure ZnO films deposited by ultrasonic spray pyrolysis. *Applied Surface Science*. 2015; 328:177-182. <https://doi.org/10.1016/j.apsusc.2014.11.084>
- [6] Yang GP, Lu MK, Yuan DR, Song CF, Liu SW, Cheng XF. Luminescence characteristics of ZnS nanoparticles co-doped with Ni²⁺ and Mn²⁺. *Opt. Mater.* 2003; 24, 497-502. [https://doi.org/10.1016/S0925-3467\(03\)00036-3](https://doi.org/10.1016/S0925-3467(03)00036-3)
- [7] Bhargava RN, Lumin J. Doped nano crystalline materials. *Physics and applications*. 1996: 70; 85-94. [https://doi.org/10.1016/0022-2313\(96\)00046-4](https://doi.org/10.1016/0022-2313(96)00046-4)
- [8] Waldrip KE, Lewis JS, Zhai Q, Davidson MR, Holloway PH, Sun SS. Improved brightness, efficiency, and stability of sputter deposited alternating current thin film electroluminescent ZnS:Mn by codoping with potassium chloride. *Appl. Phys. Lett.* 200: 76; 1276- 1278. <https://doi.org/10.1063/1.126007>
- [9] Gaikwada RS, Bhande SS, Rajaram SM, Bhagwat NP, Gaikwad SL, Han SH, Joo OS. Roughness-based monitoring of transparency and conductivity in boron-doped ZnO thin films prepared by spray pyrolysis. *Materials Research Bulletin*. 2012: 47; 4257-4262. <https://doi.org/10.1016/j.materresbull.2012.09.022>
- [10] Steinhauser J, Fay S, Oliveira N, Vallat SE, Zimin D, Kroll U, Ballif C. Electrical transport in boron-doped polycrystalline zinc oxide thin films. *Physica Status Solidi (A)*. 2008: 205; 1983-1987. <https://doi.org/10.1002/pssa.200778878>
- [11] Williamson GB, Smallman RC. Dislocation densities in some annealed and cold worked metals from measurements on the X-ray Debye-Scherrer spectrum. *Philos. Mag.* 1956:1; 34-46. <https://doi.org/10.1080/14786435608238074>
- [12] Antonis NA. Band Gap Engineering via Doping: A Predictive Approach, *Journal of Applied Physics*. 2015:117, 125708. <https://doi.org/10.1063/1.4916252>
- [13] Jrad A, Nasr, TB, Turki KN. Study of structural, optical and photoluminescence properties of indium-doped zinc sulfide thin films for optoelectronic applications, Tunisia, *Optical Materials*. 2015; 50:128-133. <https://doi.org/10.1016/j.optmat.2015.10.011>
- [14] Murali KR, Dhanmozhi AC, John R. Brush plated ZnS films and their properties. *Journal of Alloys and Compounds*. 2008: 464; 383-386. <https://doi.org/10.1016/j.jallcom.2007.09.131>



Research Article

The effects of foundry sand components on the cast iron

Sevim Alisir^{a,*}, Sinem Cevik^b

Department of Metallurgy and Materials Engineering, Ondokuz Mayıs University, Samsun, Turkey

Article Info

Article history:

Received 11 Sep 2019

Revised 15 Jan 2020

Accepted 17 Jan 2020

Keywords:

Foundry sand;

Cast iron;

Microstructure;

Mechanical properties;

Perlite and bentonite.

Abstract

Many studies are being carried out on factors such as casting temperature, cooling rate, mold design and, so on due to the effects of casting and solidification conditions on the mechanical properties of the final product. However, given literature, there appears to be no comprehensive study on the effect of casting mold sand components on the mechanical properties of cast iron. From this point of view within the scope of this study, the effects of casting mold sand and binder on the cast iron were investigated. By using silica and olivine as foundry sand at different ratios, bentonite and perlite as binders, the effects of them on the microstructure and the mechanical properties of casting were investigated. The microstructures of the products show that as the cooling rate slows down, the distribution of graphite particles in the structure changes from flakes to nodules. These structural changes are very matched with the results of mechanical properties. Therefore, when the cooling rate decreases, the hardness decreases from 310 HV to 239 HV in all of the groups. Also, the bending strength is going from 971.53 MPa to 487.42 MPa, like in the hardness results. On the contrary, the deformation increases from 13 % to 24 % when cooling rates decreases. This study clearly demonstrates that the products can be obtained by changing the heat conduction coefficient of the casting mold with different mechanical properties from the same molten metal.

© 2019 MIM Research Group. All rights reserved.

1. Introduction

The alloy of iron in which the carbon ratio is 2- 4 %, is usually called cast irons. They are hard and brittle. Because of the brittle character, they can be produced by the method of casting [1]. They include much more silicon (max 3.5 %) and phosphorus (max 2 %) content than steels do. The microstructure (containing phases and the distribution of these phases) and mechanical properties of cast iron depend on chemical composition (especially carbon and silicon content) and cooling rate. Cast irons have many advantages in terms of both castings and finished parts. They have 20-40% lower production cost than steels, good fluidity (increases when approaches eutectic composition), good vibration damping, high compression strength, low volume shrinkage during solidification, high corrosion and wear resistance. Cast irons are used especially in the automotive industry as crankshaft, piston ring and, the parts of brake system.

The gray cast iron of which the fracture surface seems gray is one of the kinds of cast iron. It is a widely used cast material. The carbon in its composition is in the form of free graphite flakes or iron carbide (cementite) after solidification. The size, distribution, and shape of the incorporated graphite particles in gray cast iron significantly affect the mechanical properties of product. They can be controlled by adding a large number of

*Corresponding author: sevimh@omu.edu.tr

^a orcid.org/0000-0001-7296-8318; ^b orcid.org/0000-0002-3506-7892

DOI: <http://dx.doi.org/10.17515/resm2019.148ma0911>

Res. Eng. Struct. Mat. Vol. 6 Iss. 2 (2020) 127-140

alloying elements (Ni, Cr, Mo, Al, Cu, Mg, S, etc.), [2-5] or by changing the cooling rate of the molten metal [6].

Many casting methods and different molding materials are also used in the iron casting industry, depending on the size and mechanical properties of the desired product. Among the techniques used, the sand molding method is irreplaceable due to its suitability to different product sizes and compositions, the reuse of the molding sand, and its low cost [7].

In the sand-casting method, first molten metal is poured to sand mold, then waited for a while to permit the metal to solidify in the mold. There are two major factors that determine to great extent the soundness of the final casting produced in this method. The first factor, graphitization, is the process in which free carbon is precipitated in iron, or the chemically bonded carbon (Fe_3C) is replaced by free carbon (or graphite). The second factor that significantly influences the microstructure of cast iron is the cooling rate during solidification. It is also a very useful parameter in the graphitization process.

The cooling rate defines the solidification time of molten metal and varies depending on the heat conduction coefficient of the mold. At an industrial level, the quality of the molding sands is crucial to provide high- grade castings. Because the heat conduction coefficient of the mold changes as the mold components change. The cooling rate can be controlled by using molding components of different types or compositions to obtain the product with the desired mechanical properties. So, the most important point in this technique is the adjustment of sand components.

When the studies done to date are examined, it is seen that many factors mentioned above affect the microstructure and mechanical properties of cast iron.

In the study of Gupta et al., the distribution of graphite clusters in the product was investigated by using three different mold systems, which include green sand mold, dry sand mold, and CO_2 sand mold. The methods used in production are effective on microstructure and mechanical properties (such as tensile strength, Brinell hardness, and Charpy impact test) [8].

Górny and Tyralla investigated the effect of cooling rate on microstructure and mechanical properties as determined by changing molding media and section size. Thin-walled iron castings with 2-5-mm wall thickness and different molding materials (silica sand and insulating sand "LDASC") were used to obtain various cooling rates. In the study, the gray cast iron used was hyper-eutectic, with a C_{eq} value of 4.58 [9].

In his studies, Sjogren changed the shape of the graphite in the microstructure by adjusting the amount of magnesium in eutectic cast iron. In the report, experiments confirmed the importance of micro-yielding of the matrix at the tip of the graphite particles on the macro-elastic behavior of the studied cast irons. It was determined that the macro-stress and macro-strain values of the flake graphite cast iron are very lower than in the case of the compacted graphite cast iron [4].

The researches given above showed that the main factor underlying the change in properties of the product is the change of cooling rate. As is known, the heat conduction coefficient of the mold also depends on the casting mold components. To our knowledge, there is only one systematic study in the literature that shows the effect of mold components on the microstructure and mechanical properties of the product obtained from cast iron.

An experiment was done by Adedayo to investigate the effects of additions of iron fillings to green molding sand on the microstructure of gray cast iron. For this experiment, five sand samples were prepared with different Fe content ranging from 1 wt% to 5 wt%. The

properties of the sand samples were tested and used to cast some grey cast iron samples whose microstructure was observed by optical microscopy. The results show that the addition of Fe filing does not have any adverse effects on the properties of green molding sand; however, the microstructures show a dependence on the heat storage capacity of the mold [10].

In the present study, it was examined how mold sand and binder used in the production of cast iron affect the microstructure and mechanical properties of the final product. For this purpose, two different foundry sands (olivine and silica sand) and two different binders (bentonite and perlite) were used in our study.

2. Materials and Methods

2.1. Casting Process

The different kinds of metallic scraps were used to prepare molten metal (in Fig. 1a). Melting was performed in an intermediate frequency electric induction furnace in a 100 kg crucible (in Fig. 1b). After the scrap metal was heated to 1490 °C, the molten cast iron was poured into the sand mold at 1450 °C (in Fig. 1c). Three samples were poured for every sub working groups.

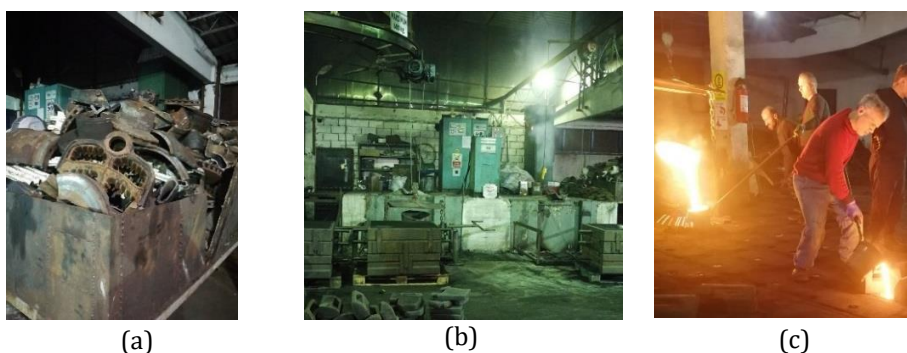


Fig. 1 Casting process

The chemical composition analysis of the investigated gray cast iron was made with Foundry Master Spectrometer by measuring from five different regions to determine the homogeneity of the castings and reported in Table 1.

Table 1. The chemical compositions of the investigated cast iron

Fe%	C%	Si%	Mn%	P%	Si%
92.950	2.717	3.085	0.595	0.154	0.025

2.2. Mold preparation process

In this study, two different sands were used as mold sands. The first is silica; the other is olivine. Also, all molding sand components were prepared to contain approximately 8.8% binder. Two different binders (bentonite and perlite) were added to each group.

Bentonite, which is a kind of clay, can be used as a binder material in sand molding process. It includes montmorillonite and volcanic ash predominantly, and it is in the mineral group of aluminosilicates. It provides mold sands good flowability, compatibility, and thermal stability for the production of high-quality castings [11]. In this study, CANDOK foundry grade bentonite is used as a binder (in Fig. 2a).

Perlite is importantly useful material for heat insulation. It is also known as a lightweight material [12]. Turkey has 70 % of world reserves. Therefore, expanded perlite was selected as the other binder and provided by AKPER (in Figure 2b).



Fig. 2 Used binders (a) bentonite and (b) perlite

In the first working group, the amount of silica sand and coke powder was kept approximately constant. But the amount of bentonite and perlite used as the binder in sand mold were changed (in Table 2). For second working group was used olivine instead of silica sand, and other ingredients remained the same. For each group the effects of the change in the ratio of bentonite and perlite at all composition were investigated individually on the quality of castings.

The composition of the mold sands and the sample code in experimental working groups can be seen in Table 2 and Fig. 3, respectively.

Table 2. Mold compositions (*WG: working group)

	Samples	Mold sand (%)	Coke powder (%)	Bentonite (%)	Perlite (%)	Water (%)
I. WG * (silica)	1.1	78.89	8.87	8.87	None	3.37
	1.2	78.82	8.78	3.90	4.97	3.53
	1.3	78.82	8.78	None	8.78	3.53
II. WG * (olivine)	2.1	78.89	8.87	8.87	None	3.37
	2.2	78.82	8.78	3.81	5.06	3.53
	2.3	78.82	8.78	None	8.87	3.53

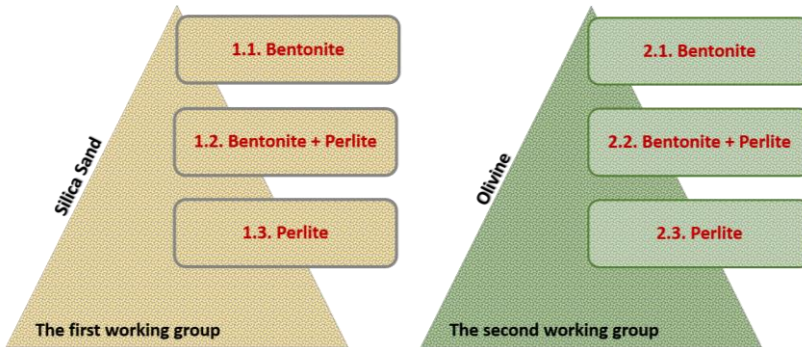


Fig. 3 The sample code in experimental working groups

The samples with dimensional 40 x 40 x 40 mm and 40 x 40 x 150 mm were produced in the foundry. The prearranged model (in Fig. 4a) and feeder were put into mold sand for the casting process (in Fig. 4b). Mold sands that were mixed in specific proportions according to their recipes were supported and pressed. Then the molten metal was poured to mold sands by ladle. The pictures for mold preparation are shown in Fig. 4. Some parameters, the chemical composition of castings and molding time, were held as constant as possible during the casting process.

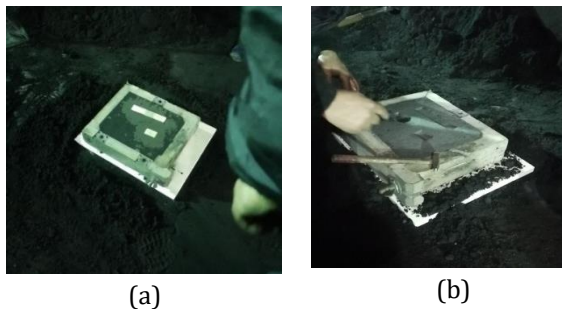


Fig. 4 Mold preparation process

2.3. Characterizations of the sample

After the casting process, the sample was mounting with bakelite for the optical microscope. Then the surface of the samples was ground and polished to observe the microstructure of samples (in Fig 5). The etching was made by using of 5 % nital solution.

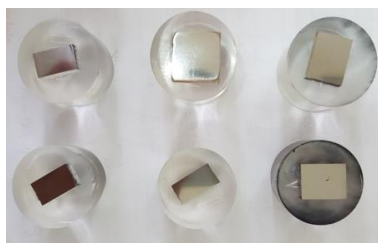


Fig. 5 Preparation of the samples for optical microscope.

To evaluate the microstructure of the castings and to observe surface defects, Leica DM2500P model light microscope connected to computer equipped with image analysis software was used.

The tensile tests were conducted 10 tone universal MARES tension-compression test unit (in accordance with ASTM E9 standard). The cube-shaped samples with dimensions 25 mm x 25 mm x 25 mm was used for compression tests.

The hardness test was performed using TMTECK HV-1000B model hardness tester at the load of 200 gf. In order to obtain an average hardness value, measurements were taken from at least 10 different regions.

Three-point bending tests were performed (in accordance with ASTM E855) by GUNT, Wp300 model device. During test, bearer length was adjusted as 100 mm, and test maintained until samples were broken (in Fig. 6).



Fig. 6 Three-point bending test samples

3. Results and Discussion

The effects of used mold sand and binder on the microstructure and mechanical properties of cast iron are the main objectives of the present study. Therefore, working groups were formed in order to observe the mold sand and binding effect on the product more clearly (as seen in Fig. 3).

3.1. Analysis of Chemical Compositions

After spectral chemical analysis, to define the type of final castings, the results were compared to cast iron compositions, and carbon equivalent was calculated by helping Equation 1 [11].

$$C_{eq} = \% C + (\% Si + \% P) / 3 \quad (1)$$

The carbon equivalent value ($C_{eq} = 3.79$) was found, and from these findings, it is clear that the final cast product is solidified as a gray cast iron. It is evaluated as hypoeutectic gray cast iron since C_{eq} value is lower than 4.25 % [13].

3.2. Mechanical Properties

The stress-strain diagrams for the samples according to their codes have been shown in Fig. 7. It is seen that in both of the sample groups, provided cast iron molded by bentonite addition has got a positive effect on the strength of the cast iron. Perlite addition to mold sand decreases the max strength of castings. It is concluded that cast samples prepared by the molds with only perlite addition have the lowest max strength. However, the castings produced in silica sand mold has more max strength than the others molded by using olivine sand shown in Fig. 8. In Table 3, it is seen the thermal conductivities of some of the different kinds of sands and clays. Among these silica sand has the highest thermal conductivity with 7.7 W/m. K. Therefore, its thermal conductivity is almost twice olivine's sand. The produced gray cast irons molded with silica sand has got a high cooling rate.

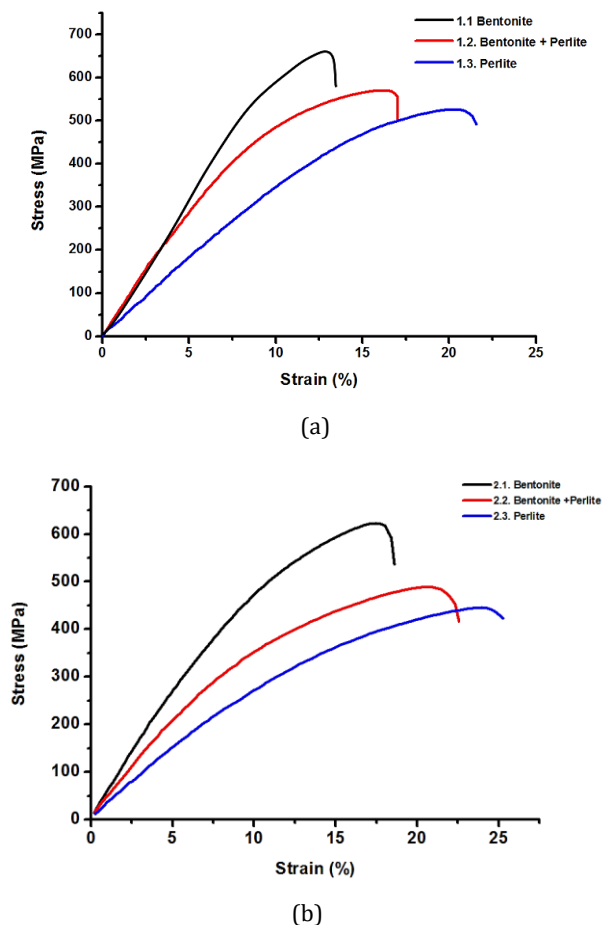


Fig. 7 Stress-strain diagram of produced sample (a) first, (b) second working group.

As seen in Fig 7a, the increasing cooling rate leads to rising max compression strength. Bentonite has a higher thermal conductivity than perlite (as seen in Table 3). It was determined that compressive strength decreased from bentonite (presented with 1.1

sample code, 660.70 MPa) to perlite (presented with 1.3 sample code, 526.03MPa) in the same working group. However, ductility was observed to increase.

Table 3 Thermal conductivities of some of the different kinds of clays and sands

Various clays and sands	Thermal conductivity (W/m.K)	References
Silica sand (Quartz)	7.7	[14]
Olivine	4.6	[14]
Bentonite	1.15	[15]
Perlite	0.0547	[15]

A similar change was observed in the second working group (in Fig 7b). It was determined that the compressive strength decreased from 622.5 to 445.5 MPa (sample 2.1 and 2.3, respectively).

Moreover, a similar effect was observed in molding sand exchange. The compressive strength of the product obtained from the mold of silica sand with rapid cooling was found to be 660.7 MPa, while the compressive strength of the product obtained from the slower cooling olivine was determined to be 622.5 MPa (presented with 1.1 and 2.1 sample codes, respectively). The same binder (bentonite) was used in the preparation of mold of these two samples.

So, the gray cast irons molded by high bentonite addition have higher maximum strengths in the two working groups (in Fig 8). It is concluded that perlite (low thermal conductivity) addition to mold sand has a negative effect on the maximum compression strength of the provided cast irons.

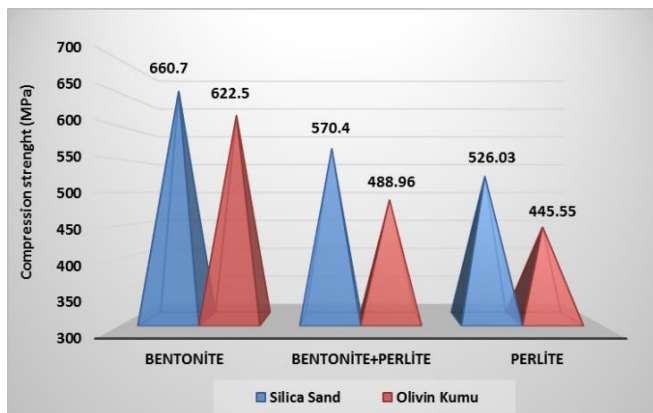


Fig. 8 Maximum strength of castings prepared in molds by silica and olivine sand

Similar results were observed in Ref. 16. In there, Adedayo shows that the heat storage capacity (HSC) of the mold has significant effects on the microstructure and properties of gray iron. He suggests that HSC of mold could be varied as required to effect changes in the microstructure, tensile strength, elongation, hardness, and toughness of gray iron.

It is also observed that after tensile- compression test, the samples are fractured at 45° (in Fig. 9).



Fig. 9 Fractured samples after tensile- compression test

Hardness is a measure of a material’s resistance to localized plastic deformation (e.g., a small dent or a scratch). Hardness tests are usually made to evaluate the materials’ mechanical properties. It is also clearly known that when the cooling rate decreases, the hardness decreases, so there is a direct relationship between the hardness, cooling rate, and max strength [17]. In Fig. 10 demonstrates the hardness test results of sample groups. In the first study groups (silica sand) due to the fact that the binder, bentonite, with a higher thermal conductivity coefficient has a faster cooling, the harder material was obtained. In the second study group (olivine sand), similar results are observed.

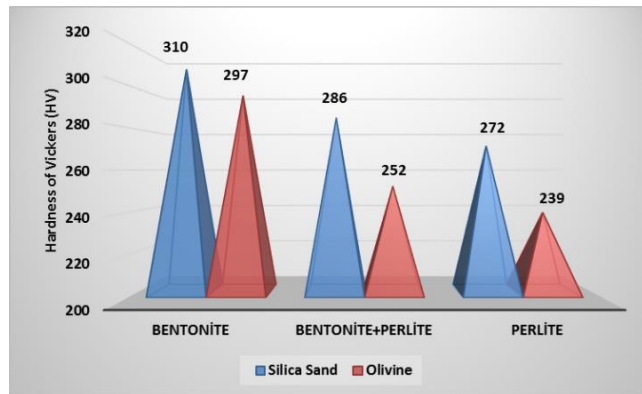


Fig. 10 Hardness values of castings prepared in molds by silica and olivine sand

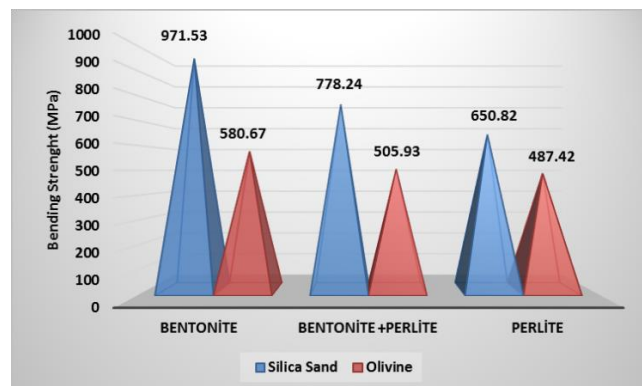


Fig. 11 Three- point bending test results of castings prepared in molds by silica and olivine

The results of three- point bending test show that increasing hardness (increasing cooling rate) leads to increasing bending strength (Fig. 11). The provided three- point bending test results for both of the study groups are very consistent with the compression and hardness test results (Fig. 12).

As a result, for working group 1, as seen in Fig. 12 the cooling rate decreased, bending stress and hardness decreased while ductility increased. Also, for the second group, the cooling rate decreased, bending stress and hardness decreased while ductility increased (in Fig. 13).

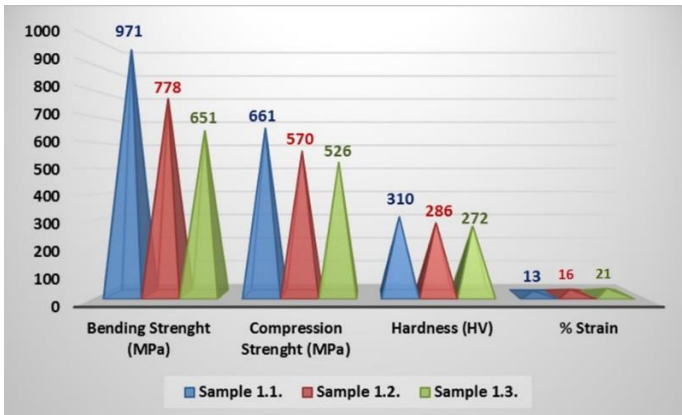


Fig. 12 The comparative mechanical properties for the first working group

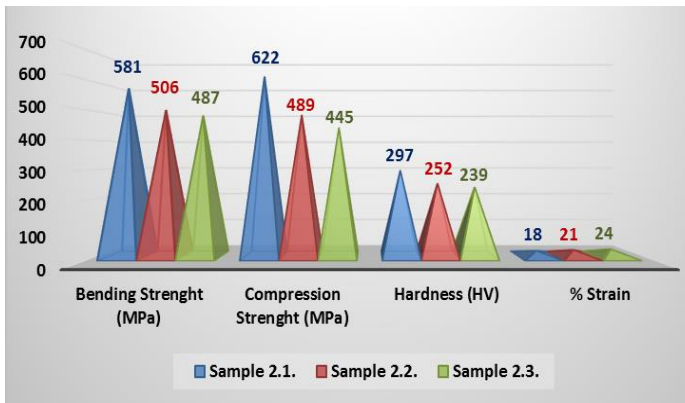
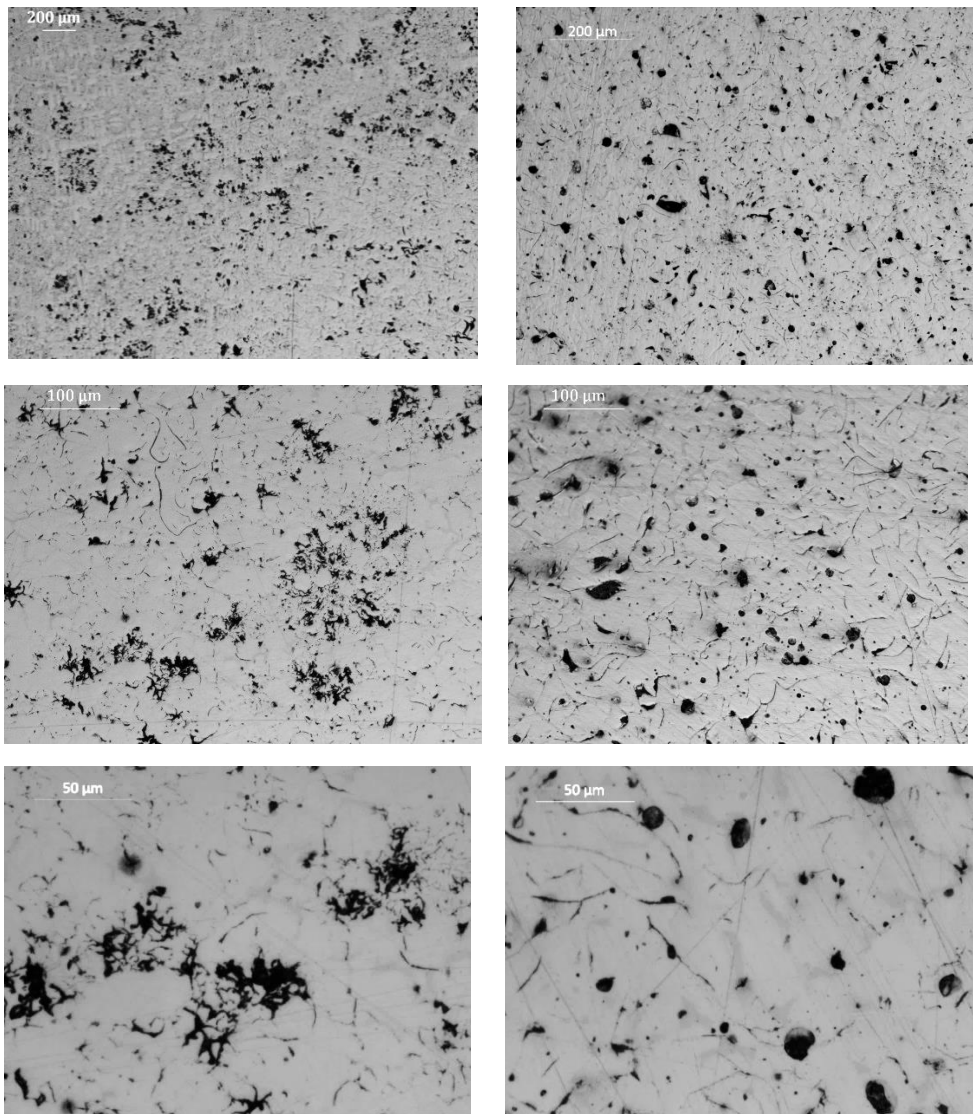


Fig. 13 The comparative mechanical properties for the second working group

3.3. Microstructural Characterization

It is well known that the mechanical properties of cast irons at room temperature are very dependent on lots of different parameters. These are solidification microstructure, consisted phases in the matrix, chemical composition and size, shape, and distribution of graphite. There are other factors also affecting the microstructure of gray cast irons such as inoculants and thickness of sections. However, the most important is the cooling rate applied during the solidification of the molten metal [16, 17].



(a) For the sample 1.3. from first working group

(b) For the sample 2.3. from second working group

Fig. 14 The microstructure of products

In Fig. 14 (a), it is seen the microstructure of provided gray cast iron from group 1.3. For this sample, the silica sand and perlite mixture were used as a mold. The microstructure demonstrates that graphite flakes dispersed heterogeneously on the matrix. It is known that foundry practice can influence nucleation and growth of graphite flakes [18]. The amount of graphite and size, morphology, and distribution of graphite flakes are critical in determining the mechanical properties of gray cast iron. The appearance of graphite flakes is like a rosette group. Since as is known, silicon is an element that facilitates graphitization in the solidification of cast iron, high Si content is thought to be effective in

the formation of rosette- like graphite without heat treatment. So that the size and type of graphite flakes is important to determine the mechanical properties of castings. The effect of high cooling rates in producing fine microstructures results in the development of high strength cast [17].

Lamellar graphite is classified into five types for foundries and they are designated by capital letters A through E. A lamellar graphite shows random orientation, and it is very suitable for lots of applications. In Fig.14 (b) it is clearly seen A- type [18] graphite structure was formed in produced gray cast iron molded in olivine + perlite mixture. Because of the low thermal conductivities of olivine and perlite, low cooling rate results. These results are very well correlated with the microstructure. In this case, the solidification time is long, the growth rates of the graphite cells are high. This structure gives maximum ductility and toughness [15].

The microstructures of gray iron can be evaluated by cooling rate, composition, nucleation and growth conditions existing during solidification. So, as the undercooling decreases (by a decrease of cooling rate), diffusion rate increases, and the carbon atoms can diffuse more extensively by the time. This results in coarse grains. Rapid cooling produces fine dendrites, while slow cooling results in large and coarse dendrites. Thus, solidification over a temperature range is the primary requirement for dendrite growth [17]. In all samples, it is observed that some porosities and all distributed heterogeneously in the dimension of different sizes. It is not unexpected to see them on the surface because some thermal decomposition of organic components of mold sands can occur during the casting process. This leads to a large emission of gases, and some gas bubbles traps on the surface of the cast. This is a disadvantage for the quality of castings [19].

4. Conclusions

The effects of casting mold sand, and binder on the cast iron were investigated. By using silica and olivine as foundry sand at different ratios, bentonite and perlite as binders, the effects of them on the microstructure and the mechanical properties of casting were determined. The results are evaluated based on the thermal conductivity of sands and binders. As a result, the mold sand and binder used in the casting process affects on both the microstructure and the mechanical properties of final castings importantly. Based on this study, the following conclusions are obtained;

- The microstructures of the products show that as the cooling rate goes up, the distribution of graphite particles in the structure changes from nodules to flakes.
- The microstructure of sample 2.3., which olivine and perlite were used as the molding component, show that spherical graphite nodules were obtained without any heat treatment or additive in the lower cooling rate. Especially, this is very important in the manufacturing of products which must have high impact resistance and damping properties. If the casting mold is prepared according to these molding components, the produced part will not need heat treatment again.
- When the cooling rate decreases, the hardness decreases from 310 HV to 239 HV in all of the groups. Also, the bending strength is going from 971.53 MPa to 487.42 MPa, like in the hardness results. On the contrary, the deformation increases from 13 % to 24 % when cooling rates decreases.

In summary, cast iron is used as a raw material for many productions in the industrial applications because of its high carbon content and relatively low mechanical properties. With any probable improvement which can be made in its

mechanical properties, it will provide pig iron opportunity to be used directly in many more industries. Therefore, a change that will be done in the casting method will provide the desired properties to be obtained at a lower cost.

Acknowledgement

The authors thank AKIN POMPA in Samsun for their help in casting the samples.

References

- [1] Heine RW, Loper CR, Rosenthal PC. Principles of Metal Castings. 26th reprint, TMH ed. New York, USA, 2003, p. 86.
- [2] ELsawy EET, EL-Hebeary MR, El Mahallawi ISE. Effect of manganese, silicon and chromium additions on microstructure and wear characteristics of grey cast iron for sugar industries applications. *Wear.* 2017; 390: 113 - 124. <https://doi.org/10.1016/j.wear.2017.07.007>
- [3] Gundlach R, Meyer M, Winardi L. Influence of Mn and S on the properties of cast iron part III testing and analysis. *International Journal of Metal Casting.* 2015; 9: 69 - 82. <https://doi.org/10.1007/BF03355617>
- [4] Sjogren T, Vomacka P, Svensson IL. Comparison of mechanical properties in flake graphite and compacted graphite cast irons for piston rings. *International Journal of Cast Metals Research.* 2004; 17; 65 - 71. <https://doi.org/10.1179/136404604225017474>
- [5] Nakae H, Shin H. Effect of graphite morphology on tensile properties of flake graphite cast iron. *Material Transactions.* 2001; 42: 1428 - 1434. <https://doi.org/10.2320/matertrans.42.1428>
- [6] Salazar FR, Herrera-Trejo M, Castro M, Me'ndez JN, Torres JT, Me'ndez M. Effect of Nodule Count and Cooling Rate on As-Cast Matrix of a Cu-Mo Spheroidal Graphite. *Journal of Materials Engineering and Performance.* 1999; 8: 325 - 329. <https://doi.org/10.1361/105994999770346873>
- [7] Ibitoye SA. Effect of the addition of sodium silicate and bulk density variation on the permeability of potter's clay-bonded moulding sand. *Nigerian Society of Engineers Technical Transactions.* 2005; 40: 67 - 77.
- [8] Gupta AK, Boruah D, Suresh N, Kamal N, Singh AK. Preparation effect of the mould systems on the microstructure and mechanical properties of spheroidised graphite iron. *Int. Journal of Engineering Research and Applications.* 2016; 6: 68 - 73.
- [9] Górný M, Tyrála E. Effect of cooling rate on microstructure and mechanical properties of thin-walled ductile iron castings. *Journal of Materials Engineering and Performance.* 2013; 22: 300 - 305. <https://doi.org/10.1007/s11665-012-0233-0>
- [10] Adedayo AV. Effects of Addition of Iron (Fe) Filings to Green Moulding Sand on the Microstructure of Grey Cast Iron. *Journal of the Brazilian Society of Mechanical Sciences and Engineering.* 2010; 32: 171 - 175.
- [11] Atanda PO, Olorunniwo OE, Alonge K, Oluwole OO. Comparison of Bentonite and Cassava Starch on the Moulding Properties of Silica Sand. *Int. Journal of Materials and Chemistry.* 2012; 2: 132 - 136.
- [12] Vaou V, Panias D. Thermal insulating foamy geopolymers from perlite. *Minerals Engineering.* 2010; 23: 1146 - 1151. <https://doi.org/10.1016/j.mineng.2010.07.015>
- [13] Radzikowska JM. Metallography and Microstructures of Cast Iron. The Foundry Research Institute. Kraków, Poland, 2004, 565 - 587. <https://doi.org/10.31399/asm.hb.v09.a0003765>
- [14] Petitjean S, Rabinowicz M, Gregoire M, Chevrot S. Differences between archean and proterozoic lithospheres: assessment of the possible major role of thermal

- conductivity. *Geochemistry Geophysics Geosystems*. 2006; 7. <https://doi.org/10.1029/2005GC001053>
- [15] Ichim A, Teodoriu C, Falcone G. Estimation of cement thermal properties through the three-phase model with application to geothermal wells. *Energies*. 2018; 11: 2839 - 2850. <https://doi.org/10.3390/en11102839>
- [16] Adedayo AV. Characterization of graphite flakes in grey iron microstructure. *Arabian Journal for Science and Engineering*. 2012; 37: 1645 - 1652. <https://doi.org/10.1007/s13369-012-0265-7>
- [17] Behnam MMJ, Davami P, Varahram N. Effect of cooling rate on microstructure and mechanical properties of cast iron. *Materials Science and Engineering A*. 2010; 528: 583 - 588. <https://doi.org/10.1016/j.msea.2010.09.087>
- [18] Collini L, Nicoletta G, Konecna R. Microstructure and mechanical properties of pearlitic gray cast iron. *Materials Science and Engineering A*. 2008; 488: 529 - 539. <https://doi.org/10.1016/j.msea.2007.11.070>
- [19] Orlenius J, Dioszegi A, Dioszegi Z. Gas absorption in grey cast iron during mould filling. *International Journal of Cast Metals Research*. 2008; 2: 427 - 434. <https://doi.org/10.1179/136404608X373140>



Research Article

Investigation of glycerol-Ni(NO₃)₂·6H₂O /perlite composites as form stable phase change materials

Tuğba Gürmen Özçelik*

Department of Chemical Engineering, Engineering Faculty, Ege University, Turkey.

Article Info

Article history:

Received 21 Feb 2019

Revised 28 Jun 2019

Accepted 02 July 2019

Keywords:

Ni(NO₃)₂·6H₂O;

latent heat storage;

Composite PCM;

Glycerol;

Expanded perlite

Abstract

In this presented experimental research, composites of phase change materials (PCMs) were prepared by impregnating glycerol and nickel salt into the expanded perlite pores (EP). In this study, vacuum impregnation and wet impregnation methods were used. Glycerol and nickel salt were inserted to the pores of EP and during the phase transition the leakage of the glycerol and nickel salt were prevented. The characterization study of chemical structure and surface microstructure of the composite PCMs were performed by Fourier transformation infrared spectroscopy (FTIR) and scanning electron microscopy (SEM). Thermal properties were determined by differential scanning calorimeter (DSC) instrument. The melting temperature and latent heat were determined for prepared composite, as -8.3°C and 136 J/g for vacuum impregnation method. For wet impregnation method the melting point could not be measured because of the PCM mixture could not deposited into perlite by using this method. The FTIR analysis presented that no chemical reactions take place between the EP and prepared PCM mixture. SEM images showed that the glycerol nickel salt mixture dispersed uniformly into the EP pores. During the heating and cooling processes, leakage and impairment of the composite PCM were not detect. Consequently, the PCM composite obtained by vacuum impregnation method, can be used for thermal energy storage applications.

© 2019 MIM Research Group. All rights reserved.

1. Introduction

Industrial development and rising population increase the energy consumption in the world. It is a known fact that the primary used energy resources of the world are going to exhausted rapidly and also the usage of traditional energy sources are main cause of the environmental pollution. Energy storage seems as a good opportunity to solve the energy problem in the world as well as to improve new renewable and clean energy sources. To meet energy needs of the developed communities, the renewable energies can be used conjunction with energy storage systems. Also, efficient and compact energy storage systems seem to be important parameters to improve the use of renewable sources. [1].

Thermal energy could be stored as latent heat, sensible heat and thermo-chemical heat. Various thermal applications may include the thermal energy storage systems. For example; solar energy panels, heating and cooling systems and heat exchangers systems in industry contains thermal energy storage systems [2,3].

Latent heat storage materials which are known as Phase change materials (PCM) have a higher energy storage capacity with a small size of the systems. They absorb and release the heat at approximately constant temperature range during the phase transitions [4].

*Corresponding author: t.gurmen.ozcelik@ege.edu.tr

^a orcid.org/0000-0002-7861-0189

DOI: <http://dx.doi.org/10.17515/resm2019.122ma0221>

Res. Eng. Struct. Mat. Vol. 6 Iss. 2 (2020) 141-151

To control the temperature in many engineering applications, phase change materials (PCM) are commonly used for thermal energy storage. According to their phase transition states, phase change materials are categorized in four groups. These categories are solid-solid, solid-gas, solid-liquid, liquid-gas PCMs [2, 5, 6]. Even though liquid-gas and solid-gas phase transition have higher latent heat capacity, the volume change during the phase transition is immoderate. This volume change makes the systems more complex and ineffective [2]. Because of this reason, solid-liquid and solid-solid phase changes are preferred and investigated from the many researchers. The solid liquid phase change materials are categorised in three main groups according to their chemical structure: inorganic, organic and eutectic. Although inorganic PCMs have more latent heat capacity than the organic PCMs, phase separation and subcooling may happen during the phase transition. The organic PCMs provide many advantages; for example, generally, they are not toxic, noncorrosive, and crystallize with no super cooling and segregation. Organic PCMs are examined in two groups: paraffin and non-paraffin [3- 6]. An eutectic mixture comprising two or more components forms as composition with a minimum melting point. During the crystallization every component in the mixture melts and freeze and the composition of the formed component crystals is compatible with each other [7]. The eutectic mixture may melt and freeze without phase separation because of their crystal structures. The components in the mixture melt at the same time without segregation [3].

Hydrate salts as inorganic PCMs, have some advantages of constant phase change temperature, higher heat storage capacity (nearly 300 J/g) comparatively high thermal conductivity (0.5 W/m°C) and moderate costs. They are also nonflammable and nontoxic. Thus, it may be more suitable and safer than organic PCMs in energy storage processes. The most researchers have studied with hydrate salts and eutectic mixture of the hydrate salts [8].

To prevent liquid leakage during the solid-liquid phase change, the porous materials are generally used as supports. Graphite, expanded graphite, aluminum powder, expanded perlite, activated carbon, and carbon nanotubes are chosen to keep off the liquid leakage.

Expanded perlite (EP) is an amorphous glassy volcanic rock and having porous structure. Because it has very low thermal conductivity (0.03 - 0.05W/m°C), low sound transition property and nonflammability it is generally used as insulation material in buildings (9, 10). Also, some researchers reported that, EP have a good supporting matrix for preparing composite PCMs. At the same time, PCM composites which are prepared by using expanded perlite exhibit a reduced thermal conductivity [10, 11, 12]. Li et al. have studied shape-stabilized PCMs by impregnating of paraffin into the expanded perlite pores. They used vacuum impregnation method and produced heat storage boards by adding gypsum into the prepared composite for use in buildings [13]. Z. Lu et al. prepared and examined form-stable PCMs and using the direct impregnation method to absorb the paraffin into the pores of the EP, their results showed that the leakage was prevented [14]. Karaipekli and Sarı studied Capric-myristic acid/EP composite as phase change materials they used vacuum impregnation method and the prepared composite PCM had good thermal properties and stable for thermal applications [15].

Although PCMs prepared with organic-organic eutectics and inorganic salts and their eutectic mixtures have been widely studied in the literature, there are not many studies about the organic-inorganic eutectics. The aqueous salt solutions are used as PCM for low temperature applications, but these may cause the erosion. In this research, an organic-inorganic eutectic mixture of Glycerol-Ni (NO₃)₂·6H₂O were studied for low temperature applications and form stable Glycerol-Ni (NO₃)₂·6H₂O /Expanded perlite composites were prepared by using wet impregnation and vacuum impregnation methods. Both methods are inexpensive and eco-friendly method for the composite PCM preparation. The

prepared Glycerol-Ni (NO₃)₂6H₂O eutectic mixture was enclosed into the porous of the EP and in this way the leakage was prevented during the phase transitions. Differential scanning calorimeter (DSC) and thermo gravimetric analysis instrument (TGA) were used to analyze thermal properties and stability of prepared composite. The surface area and pore volume of the EP and composite were determined nitrogen adsorption analyses for Brunauer-Emmett-Teller (BET). The structures and morphologies of the perlite and Glycerol-Ni (NO₃)₂6H₂O composites were determined by Fourier transformation infrared spectroscope (FTIR) and scanning electronic microscope (SEM). Heating and cooling cycle tests were performed to define heat accumulation and heat release properties of PCMs.

2. Experimental Study

2.1 Materials

Glycerol and the metal salt of Nickel (Ni(NO₃)₂6H₂O) were purchased from Merck. Expanded Perlite (EP) was supplied by the Batiçim-AS Company, Turkey. It was heated in an oven at 110°C before using.

2.2 Methods

Before beginning the composite PCM preparation, the eutectic point of mixture of glycerol and Ni(NO₃)₂6H₂O was calculated to decide the compositions which gives lower melting point. The Schroder equation (1) was used for calculation of the eutectic point [7].

$$\ln x_B = -\frac{\Delta H_B}{R} \left(\frac{1}{T} - \frac{1}{T_{mB}} \right) \quad (1)$$

where ΔH is latent heat, T_m is melting temperature as K, subscript B indicates the one of the components into mixture.

Then the PCM mixture was prepared in these compositions. The prepared PCM mixture included 97 wt. % glycerol and 3wt. % Ni(NO₃)₂6H₂O. Evaluated melting point of mixture at this concentration is -10 °C.

Initially, PCM mixture was prepared. Nickel salt was weighed and melted at 57°C in a backer and weighed glycerol was added in the salt and mixed during 1 hour, at 1000 rpm to obtain homogeny solution. To enclose the mixture into EP pore, two different methods were used (Wet impregnation and vacuum impregnation). Firstly, wet impregnation method was applied. EP was added to prepared mixture solution and the resulting slurry was put in an ultrasonic bath at 50°C for 30 minutes to penetrate the solution into the EP pores. Finally, the obtained composite was placed into an oven at 60°C for 10 hours. Secondly, vacuum impregnation method was used. Weighed EP was placed in the vacuum set and the prepared mixture was added it slowly under vacuum at 50°C. Then, the obtained mixture was placed into an oven at 60°C for 10 hours.

The experimental set up of the vacuum impregnation is shown in Figure 1.

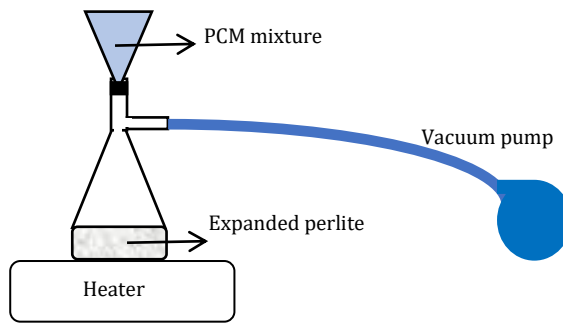


Figure 1 Experimental set-up for vacuum impregnation

To perform heating and cooling cycles, specific measure of prepared composite sample was placed into a glass tube and for recording the temperature a thermometer was put in the center of the tube. The tube was located in the hot water at 40°C for heating. When the temperature of the composite in the tube was reached steady state, the sample tube was carried into chilled water alcohol bath at -15°C for cooling. The temperature of the composite sample in the tube was measured with time while the heating and cooling process performed. 100 heating cooling cycles were performed to specify the prepared composite reliability.

3. Results and Discussions

3.1 Leakage Tests

To determine the absorption capacity of the EP for the eutectic mixture, leakage test was performed. Before the leakage test, PCM composite, containing 50 wt.% of perlite was prepared. This prepared PCM composite was placed on the filter paper and allowed to stand in an oven at 20°C for 30 min. The prepared PCM composite exhibits no leakage as shown in Figure 2.



Figure 2. Images of the leakage test of the composite PCM

3.2 Characterization of chemical compatibility between the eutectic mixture and EP

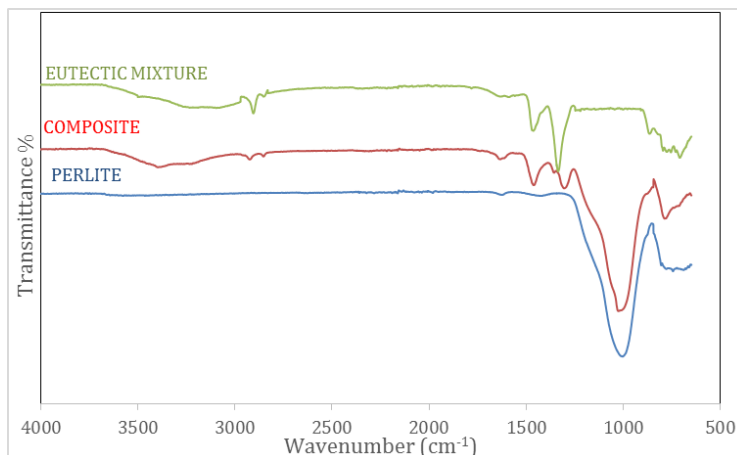


Figure 3. FTIR Spectrum of perlite, eutectic mixture and prepared composite PCM

The FTIR spectrum of expanded perlite, eutectic mixture and prepared PCM composite are shown in Figure 3. In the FTIR spectrum of the EP, the absorption band nearly at 850-900 cm^{-1} represents the vibrations of the Al-OH-Al and Al-OH-Mg groups, respectively. The intense and deep peak at 1020 cm^{-1} is described the Si-O-Si symmetric vibrations. The weak peak at 1625 cm^{-1} is described to the bending modes of the OH groups which are appended to the surface of expanded perlite and the adsorbed water molecules on the perlite [22]. In the FTIR spectra of PCM composite, which included perlite, glycerol and nickel salt, a medium absorption bands around 1300 cm^{-1} and 1360 cm^{-1} confirm the C-O stretching modes of glycerol. The symmetrical stretching vibration of CH_2 group which is stretching modes of glycerol is also shown at 2845 cm^{-1} . Intense and broad band in the range between 3000 and 3600 cm^{-1} shows the vibration of OH from coordinated those strong hydrogen bonds of water. The peak at 1458 cm^{-1} confirms the presence of the NO_3 from the nitrate salt in the composite. The band at 780 cm^{-1} can be assigned the Ni-O stretching vibration.

According to the FTIR spectrum of the composite, only the expanded perlite, glycerol and $\text{Ni}(\text{NO}_3)_2 \cdot 6\text{H}_2\text{O}$ peaks are seen, there are not observed new peaks. These specify that there is no chemical reaction between the prepared PCM mixture and the expanded perlite. The FTIR results show that the prepared composite is only a physical combination of the expanded perlite, glycerol and $\text{Ni}(\text{NO}_3)_2 \cdot 6\text{H}_2\text{O}$.

3.3 Microstructure of expanded perlite and PCM composite

The BET surface area and micropore volume of EP and prepared composite were determined. According to the result the used expanded perlite BET surface area and pore volume are obtained 112.3 m^2/g and 0.63 cm^3/g respectively. After vacuum impregnation of eutectic mixture PCM into the EP pores, BET surface area and pore volumes were decrease to 0.0345 m^2/g and 0.000007 cm^3/g , respectively. These significantly decrease shows that the PCM mixture was placed into the EP pores.

Figure 4 a and Figure 4 b show the SEM images of the expanded perlite and composite PCM prepared by vacuum impregnation method, respectively. It can be seen from Figure 4-a,

the expanded perlite has a highly porous structure having many micro-pores with different sizes. These structures make the expanded perlite as a good supporting material to keep the PCM mixture. As seen from Figure 4-b, PCM mixture were dispersed uniformly in the porous and the sheets of the EP and the composite shows the most favorable homogenous morphology.

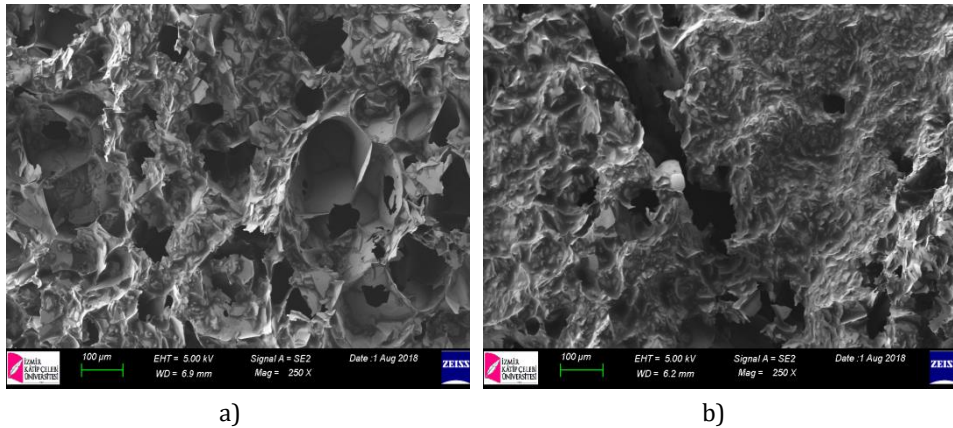


Figure 4. SEM images of a) expanded perlite, b) PCM composite prepared by vacuum impregnation method.

3.4 Thermal properties of eutectic mixture and PCM composite

The melting and freezing temperatures and latent heat values of the prepared PCM mixture and composites are listed in Table 1. DSC curves of PCM mixture and prepared composite with vacuum impregnation method before and after thermal cycling test are given in Figure 5. According to the DSC analysis from the PCM prepared using two different methods, there were observed no peaks in the wet impregnation method. It is thought that the PCM mixture could not be enclosed into the EP pores by using this method.

Table 1. Thermal properties of PCM

	Melting Point (°C)	Melting Latent Heat (J/g)	Freezing Point (°C)	Freezing Latent Heat (J/g)
PCM Mixture	-9.7	165	-9.8	163
Wet Impregnation	-	-	-	-
Vacuum Impregnation	-8.3	134	-8.2	136
Vacuum Impregnation (After 100 cycle test)	-8.4	130	-8.1	136

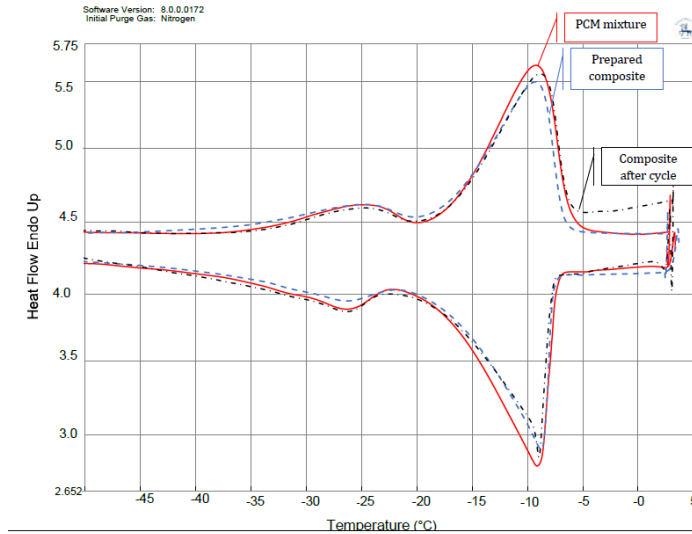


Figure 5. DSC curves for prepared composite PCM

According to DSC results, the phase transition temperatures of composite PCM which prepared by using vacuum impregnation method were about 1.4°C higher than that of the prepared eutectic mixture. On the other hand, the latent heats prepared composite PCM were found to be lower than the latent heats of the PCM eutectic mixture. The changes of the phase transition temperatures and the latent heat values are an indication of the force of the interactions between the expanded perlite and PCM mixture. When there is a strong relation between the PCM and pores of the support, the phase change temperature may increase and the same results have been found by some researchers for different composites [15, 16, 17 and 18]. The reduction of the latent heat value can be explained as the physical relation between the EP pores and eutectic mixture. C. Wang et al. have referred that the interaction between PCM and its support material cause the decrease of latent heat value [16]. Karaipekli and Sarı prepared eutectic mixture of capric and myristic acid and impregnated it into the EP by using vacuum impregnation method and they obtained form stable composite PCM. According to their results, melting and freezing temperatures of the eutectic mixture and prepared composite were determined as 22.61, 21.18 °C and 21.70, 20.70 °C, respectively [15]. Galazutdinova et.al. studied with inorganic composite mixture includes 40% of $MgCl_2 \cdot 6H_2O$ and 60% of $Mg(NO_3)_2 \cdot 6H_2O$. The prepared inorganic mixture, melting temperature and latent heat value were obtained as 62 °C and 120 J/g. Vacuum impregnation method was used to enclose the $MgCl_2 \cdot 6H_2O$ - $MgCl_2 \cdot 6H_2O$ mixture into EP. The prepared composite PCM had melting temperature of 63.5 °C and latent heat of 106.8 J/g [19]. Zang et all investigated $MgCl_2 \cdot 6H_2O$ - $CaCl_2 \cdot 6H_2O$ Eutectic/EP composite PCM. The prepared eutectic mixture included 15% $MgCl_2 \cdot 6H_2O$. The melting temperature and latent heat were determined as 23.9°C, 151.9 J/g, respectively. Composite PCM including 50 wt% of EP was prepared by using this eutectic mixture. The $MgCl_2 \cdot 6H_2O$ - $CaCl_2 \cdot 6H_2O$ /EP composite had exhibited a melting point of 23.5 °C and latent heat of 73.55 J/g, and there was no leakage seen after leakage tests [20]. Yilmaz et al. developed binary mixtures of tridecane and dodecane to be used as PCMs for thermal energy storage in

cooling applications. The melting point and heat of fusion of their PCM was found as -9.1°C and 145 J/g [21].

The thermal reliability is the important point to evaluate the PCM composite performance. The thermal properties of the materials can change after many thermal cycles and latent heat and phase change temperatures may change significantly. A suitable composite PCM should have steady thermal properties with many phase changes cycles without degradation [8, 10, 15]. DSC results show that, the latent heat value and phase change temperatures of the prepared composite PCM remained nearly constant after 100 heating and cooling cycles.

3.5 Thermal stability of PCM composite

TGA is commonly used to determine the thermal stability of the composites, In Figure 6, the TGA curves composite PCM is shown. The weight loss of the composite starts nearly 80°C . Due to the evaporation of glycerol the decomposition amount increased rapidly after 150°C this temperature and 58 % weight loss were measured at 350°C . Before 150°C , only 5 % decomposition is seen.

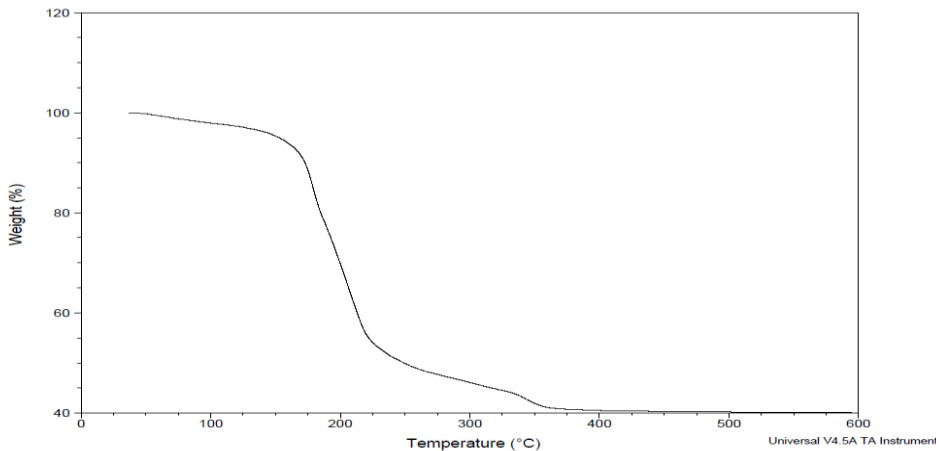


Figure 6. TGA curves of PCM composite

Heating and cooling cycles were performed to the PCM mixture and prepared PCM composite. The recorded results were drawn as temperature versus time graphic that is given in Figure 7. Each cycle of the heating and cooling were performed 20 min to obtain the steady state temperature. Figure 7 shows that, the heating and cooling rate of the prepared composite are lower than that of the PCM mixture.

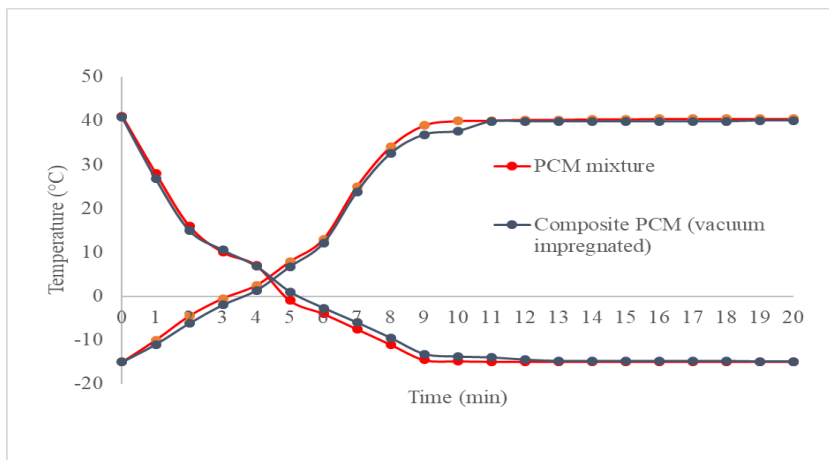


Figure 7. Heating and cooling processes for PCM mixture and PCM composites

4. Conclusion

In this work, Glycerol-Ni(NO₃)₂6H₂O / EP composite PCMs were prepared by using wet impregnation and vacuum impregnation methods. The used both methods are environmentally safe and economical therefore they are suitable for fabrication of PCM composite for industrial applications. But, according to the DSC analysis, there were not observed any phase change point by using wet impregnation method. It is thought that the PCM mixture could not be enclosed into the EP pores by using this method. Before preparation of the PCM mixture, eutectic point of the Glycerol-Ni(NO₃)₂6H₂O mixture was determined as melting point at -10°C, with 97 wt.% glycerol and 3 wt.% Ni(NO₃)₂6H₂O concentrations and the mixture were prepared at calculated composition, then it was absorbed into perlite pores.

The melting point of PCM mixture and PCM composite which prepared by using vacuum impregnation were found -9.7 and -8.3°C respectively. And phase change enthalpy values were determined 165 J/g for PCM mixture and 134 J/g for PCM composite. The changes of the melting and freezing temperatures are an indication of the force of the interactions between the EP and PCM mixture. The decrease on the latent heat values depending on the relation between the EP and PCM mixture. After heating and cooling cycles performed the composite PCM retained its melting and freezing temperatures and latent heat values. SEM images show that PCM mixture was distributed uniformly in the porous and the sheets of the EP and the composite shows the most favorable homogenous morphology. The leakage test show that the phase change process takes place in the pores of the EP. There were no leakages obtained. According to the FTIR results the eutectic PCM mixture and EP keep their original structure in the composite and the composite PCM was only the physical combination of nickel salt, glycerin and EP. After the heating cooling cycle, there was no leakage and degeneration at the composite PCM. TGA results revealed that the prepared composite has good energy storage capacities, good thermal reliability and stability.

Based on the obtained results, the presented composite PCM provide many properties of shape stabilization, moderate latent heat value and good thermal stability. In conclusion, it can be said that the prepared composite PCM has a great potential for the use in low temperature applications of thermal energy storage.

References

- [1] Trigui, A., Karkri, M., Krupa, I., Thermal conductivity and latent heat thermal energy storage properties of LDPE/wax as a shape-stabilized composite phase change material, *Energy Conversion and Management*, 2014, 77, pg. 586-596. <https://doi.org/10.1016/j.enconman.2013.09.034>
- [2] Prakash J., Garg H.P., Datta G., A Solar Heater with a Built-in Latent Heat Storage, *Energy Conversion and Management*, 1985, 25, pg. 51-56. [https://doi.org/10.1016/0196-8904\(85\)90069-X](https://doi.org/10.1016/0196-8904(85)90069-X)
- [3] Sharma A., Tyagi V.V., Chen C.R., Buddhi D., Review on Thermal Energy Storage with Phase Change Materials and Applications, *Renewable and Sustainable Energy Reviews* 2009, 13, pg. 318-345 <https://doi.org/10.1016/j.rser.2007.10.005>
- [4] Yuan Y., Zhang N., Tao W., Cao X., He Y., Fatty acids as phase change materials: A review *Renewable and Sustainable Energy Reviews*, 2014, 29, pg. 482-498. <https://doi.org/10.1016/j.rser.2013.08.107>
- [5] Rathod M. K., Banerjee J, Thermal Stability of Phase Change Materials Used in Latent Heat Energy Storage Systems: A review, *Renewable and Sustainable Energy Reviews* 2013, 18, pg. 246-258. <https://doi.org/10.1016/j.rser.2012.10.022>
- [6] Jamekhorshid A., Sadrameli S.M., Farid M., A Review of Microencapsulation Methods of Phase Change Materials (PCMs) As a Thermal Energy Storage (TES) Medium, *Renewable and Sustainable Energy Reviews* 2014, 31, pg. 531-542. <https://doi.org/10.1016/j.rser.2013.12.033>
- [7] George A., Hand book of thermal design. [chapter 1], In: Guyer C, editor. Phase change thermal storage materials. McGraw Hill Book Co.; 1989.
- [8] Farid Mohammed M., Khudhair Amar M., Razack Siddique Ali K., Al-Hallaj Said, A review on phase change energy storage: materials and applications *Energy Conversion and Management*, 2004, 45, pg. 1597-1615. <https://doi.org/10.1016/j.enconman.2003.09.015>
- [9] Won J.-P., Kang H.-B., Lee S.-J., Lee S.-W., Kan J.-W. g, Thermal characteristics of high-strength polymer cement composites with lightweight aggregates and polypropylene fiber, *Constr. Build. Mater.*, 2011, 25-10, pg. 3810-3819. <https://doi.org/10.1016/j.conbuildmat.2011.03.023>
- [10] Ye R., Fang X., Zhang Z., Gao X., Preparation, mechanical and thermal properties of cement board with expanded perlite based composite phase change material for improving buildings thermal behavior, *Materials*, 2015, 12, pg. 7702-7713. <https://doi.org/10.3390/ma8115408>
- [11] Zhang D., Tian S., Xiao D., Experimental Study on The Phase Change Behavior of Phase Change Material Confined in Pores, *Solar Energy*, 2007, 81, pg. 653-660. <https://doi.org/10.1016/j.solener.2006.08.010>
- [12] Kong X.F., Zhong Y.L., Rong X., Min C.H., Qi C.Y., Building energy storage panel based on paraffin/expanded perlite: preparation and thermal performance study, *Materials* 2016, 9, pg. 70-75. <https://doi.org/10.3390/ma9020070>
- [13] Li M., Wub Z., Chena M., Preparation and properties of gypsum-based heat storage and preservation material, *Energy and Buildings*, 2011, 43, pg. 2314-2319. <https://doi.org/10.1016/j.enbuild.2011.05.016>
- [14] Z. Lu, B. Xu, J. Zhang, Y. Zhu, G. Sun, Z. Li, Preparation and characterization of expanded perlite/paraffin composite as form-stable phase change material, *Solar Energy*, 2014, 108, pg. 460-466. <https://doi.org/10.1016/j.solener.2014.08.008>
- [15] Wang C., Feng L., Zeng J., and Tian W., Li X., Shape-stabilized phase change materials based on polyethylene glycol / porous composite: Influence of pore structure of carbon materials, *Solar Energy Materials & Solar Cells*, 2012, 105, pg. 21-26. <https://doi.org/10.1016/j.solmat.2012.05.031>

- [16] Zhang J.W., Guan X.M., Song X.X., Hou H.H., Yang Z.P., Zhu J.P., Preparation and properties of gypsum based energy storage materials with capric acid palmitic acid/expanded perlite composite PCM, *Energy Build*, 2015,92 , pg. 155-160. <https://doi.org/10.1016/j.enbuild.2015.01.063>
- [17] Mei B., Zhang, R., Liu Y., Zhang J., Liu, E, Preparation of Capric acid / Halloysite Nanotube Composite as Form-Stable Phase Change Material For Thermal Energy Storage, *Solar Energy Materials & Solar Cells*, 2011, 95, pg. 272-277. <https://doi.org/10.1016/j.solmat.2011.05.024>
- [18] Karaipekli A, Sarı A, Capric-myristic acid/expanded perlite composite as form-stable phasechange material for latent heat thermal energy storage, *Renewable Energy*, 2008, 33 pp. 2599- 2605 <https://doi.org/10.1016/j.renene.2008.02.024>
- [19] Galazutdinova Y, Vega M, Grageda M, Cabeza L.F, Ushak S, Preparation and Characterization of an inorganic magnesium chloride/ nitrate/graphite composite for low temperature energy storage, *Solar energy storage and Solar Cells*, 2018, 175, pp. 60-70. <https://doi.org/10.1016/j.solmat.2017.09.046>
- [20] Zang C, Zang Z, Ye R, Gao X, Ling Z, Characterization of MgCl₂.6H₂O-Based Eutectic/Expanded Perlite Composite phase change material with Low Thermal Conductivity, *Materials*, 2018, 11, 2369 pp. 1-11. <https://doi.org/10.3390/ma11122369>
- [21] Yılmaz S, Sayın K, Gök Ö, Yılmaz MÖ, Beyhan B, Sahan N, et al. New binary alkane mixtures as pcms for cooling applications. In: 11th International conference on thermal energy storage for energy efficiency and sustainability, June 14-17, 2009, Stockholm International Fairs. Stockholm, Sweden.
- [22] Jahanshahi, R. and Akhlaghinia, B. Expanded perlite: an inexpensive natural efficient heterogeneous catalyst for the green and highly accelerated solvent-free synthesis of 5-substituted-1H-tetrazoles using [bmim]N₃ and nitriles, *Royal Societies of Chemistry*, 2015, 5, pg. 104087-104094. <https://doi.org/10.1039/C5RA21481E>

Blank Page



Research Article

Fabrication and characterization of vapor grown carbon nanofiber reinforced flexible polymer composites

Hatice Aylin Karahan Toprakci^{*1,2,a}, Ayse Turgut^{1,2,b}, Ozan Toprakci^{1,2,c}

¹Yalova University Polymer Engineering Department, Yalova, Turkey

²Yalova University Institute of Science, Yalova, Turkey

Article Info

Article history:

Received 31 Jan 2019

Revised 08 Aug 2019

Accepted 13 Sep 2019

Keywords:

Polymer
nanocomposites;
Vapor grown carbon
nanofibers (VGCNFs);
Styrene-*b*-(ethylene-co-
butylene)-*b*-styrene
(SEBS);
Mechanical
characterization

Abstract

In this study, highly flexible polymer nanocomposites that can be stretched more than 9 times their original length were successfully fabricated by using poly [styrene-*b*-(ethylene-co-butylene)-*b*-styrene] (SEBS) and vapor grown carbon nanofibers (VGCNFs). Two different polymers were used in order to investigate the effects of the polymer molecular weight on viscosity, morphological and mechanical properties of the samples. Mixing was carried out by a planetary high shear mixer for various levels of VGCNFs and SEBS. Nanocomposites were prepared by the combination of solvent casting and compression molding. Viscosity measurements were carried out as a function of filler ratio for both polymers. Higher molecular weight and higher filler ratio led to higher viscosity. Morphological analysis showed homogeneous filler dispersion without any dominant filler orientation throughout the composites with good filler-matrix interface and absence of any pores or voids. Filler content and matrix molecular weight were found significant for mechanical properties. The mechanical strength and elastic modulus of the nanocomposites increased by the addition of VGCNF regardless of the polymer molecular weight. Nanocomposites fabricated by using higher molecular weight polymer showed better mechanical properties. Above mentioned attributes those belong to both polymer composites meet the requirements of flexible electronics and can be used for many applications including micro-electro-mechanical systems, conductive coatings, electromagnetic shielding applications, polymeric sensors and actuators.

© 2019 MIM Research Group. All rights reserved.

1. Introduction

Recent developments in technology, lead to the development of new materials and electronic materials are one of the most popular areas. Since traditional electronic materials are hard and brittle, over the last decades many of the efforts have been focused on flexible electronics because of their potential to provide the multiple requirements. Elastic and stretchable polymer-based materials with electronic capabilities have been referred to as flexible electronics. Depending on the components, type, and application, flexible electronics may be capable of sensing, data processing, actuation, and energy storage or generation. In all these applications flexibility is particularly crucial for micro-electro-mechanical systems (MEMS), sensors and actuators whose basic function is depended on their electromechanical properties. For the flexible electronics various polymers can be used as basic or auxiliary components including inherently conductive polymers [1-5], thermoplastics [6-8], thermosets [9, 10], elastomers [11-13], and thermoplastic elastomers [14-16] or polymer blends [17]. In this case, in addition to electrical character, mechanical character plays an important role during the functioning

*Corresponding author: aylin.toprakci@yalova.edu.tr

^a orcid.org/0000-0001-7078-9690; ^b orcid.org/0000-0003-3175-6364; ^c orcid.org/0000-0001-7944-4269
DOI: <http://dx.doi.org/10.17515/resm2019.108ma0131>

and not only flexible but also stretchable, bendable, twistable materials are required with high resilience and satisfying recoverability after unloading the mechanical effect [18]. Therefore, in the process of designing any the electro-mechanical system; analysis and characterization of the mechanical properties of the materials should be in the first place. As known, for electro-mechanical based systems such as sensors and actuators; electrical property is mostly governed by mechanical properties and response under various internal and/or external conditions [19, 20]. The group of polymeric materials that show all those required functions is called thermoplastic elastomers (TPEs). TPEs are polymers that combine the unique properties of thermoplastics and rubber. TPEs are compatible with a wide range of technologies and they can be used for many applications for a variety of purposes such as sealants, adhesives, rubber bands, protective films, airbag covers, automotive panels, sensors, actuators, electro-mechanical components of MEMS and so on. Processability, mechanical and end-use properties of the TPEs are the most important reasons for being preferred in these applications. While they perform as rubber in terms of elastic behavior; they can be melt-processed as thermoplastics. TPEs are copolymers with two phases as the elastomeric phase and the rigid phase. While the elastomeric phase represents the flexibility of rubber; the rigid phase represents the strength and processability of thermoplastics. Depending on the chemical structure, the ratio of these soft/rigid phases, the molecular weight of the polymer; physical, chemical and morphological properties of the TPEs change. They are named based on the thermoplastic block in the structure such as polyamide-based, olefin-based and styrene-based TPEs. In all, styrene-based thermoplastic elastomers are one of the most common TPEs found in the market due to their superior properties. In this group, poly [styrene-b-(ethylene-co-butylene)-b-styrene] (SEBS) stands out because of its superior properties such as higher thermo-oxidative and UV resistance. In SEBS, the polystyrene blocks act as rigid blocks because of physical cross-links between styrene blocks. As seen from Fig. 1, styrene blocks tie the continuous elastomeric phase in a three-dimensional network and minimize the deformation of the TPE system [21-25].

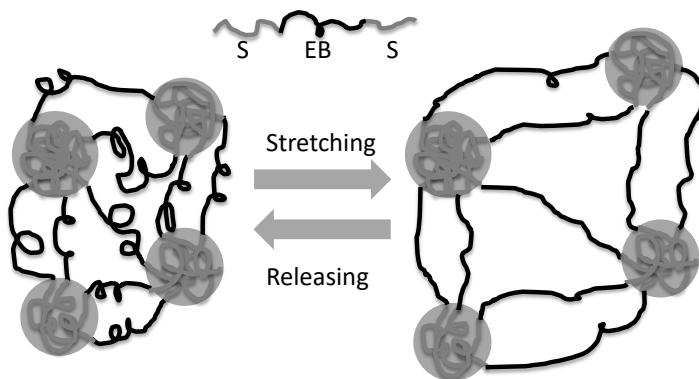


Fig. 1 SEBS under stretch and release

As mentioned above, SEBS is a promising material for flexible electronics because of its low elastic modulus, high degree of stretch ability and good resilience. In order to make it mechanically stronger and electrically conductive, fillers are needed to be incorporated into the structure. Since mechanical properties of the flexible electronics are very critical in terms of stretch ability, bendability and recoverability; filler selection should be done carefully. Surface area, surface properties, geometry and aspect ratio of the fillers have to be considered. In addition to that, if high level of fillers is loaded into the structure,

flexibility and resilience of the material will be destroyed. At this point, nanofillers become more important.

Although, SEBS can be filled with various nanofillers [26-29], depending on our experience and previous studies CNFs are one of the most suitable materials [16, 18]. Their contribution to mechanical property improvement stemmed from their unique structure. As known, CNFs are cylindrical, fibrous nanostructures that consist of arranged graphene layers with high elastic modulus that is at least two orders of magnitude higher than the polymeric materials. In addition to that high aspect ratio and high surface area enhance the filler-matrix interface and improves the mechanical properties even at low filler loadings. Since filler loading is relatively low, stretching limits and flexibility of the material can be kept almost in the same range [30-32]. However CNFs have unique properties, mechanical properties of the CNF filled composites might be affected by many factors such as polymer properties, polymer-matrix interface, filler distribution, filler orientation, mixing conditions and composite fabrication [32]. In all these filler dispersions is the most critical one. In the case of nonhomogeneous filler dispersion, many problems might occur including filler aggregation, insufficient filler wetting, decrease in the aspect ratio of fillers, bad filler-matrix interface [32, 33]. As a result of these, stress transfer from matrix to filler might not be sufficient enough and mechanical properties of the composites get worse. In the literature, CNFs were mostly dispersed in the polymeric matrix in various ways such as extrusion compounding [33-35] sonication [17, 36, 37] and so on.

In above-mentioned methods, extrusion compounding has some drawbacks such as filler breakage and/or filler agglomeration. As reported by Al-Saleh [33], depending on the process conditions fillers can break and/or agglomerate and aspect ratio of the filler decreases that leads to change in various properties. Another common method for the dispersion of the CNF is the sonication and in order to obtain good filler dispersion, the viscosity of the solution or polymer-filler mixture has to be low enough. In other words, sonication process cannot be used effectively for highly viscous solutions or mixtures. On the contrary, planetary high shear mixing has no such problems. In this method, the aspect ratio of the fillers is almost the same that is significant for the mechanical properties of the composites. Also, it can be used for both low and high viscosity solutions/mixtures. Another important advantage is relatively short processing time is (1-2 minutes) [18].

In the literature there is a very limited number of studies regarding CNF/SEBS nanocomposites. In one of these studies, polypropylene/maleated SEBS (PP/SEBS-g-MA) blends were reinforced with CNFs. Polymer and fillers were compounded by a twin-screw Brabender extruder and granules were injection molded. Injection-molded samples were analyzed in terms of morphological, thermal and mechanical properties. It was reported that mechanical properties were enhanced by the addition of CNFs [30]. In another study, CNF/PP/SEBS composites were fabricated; the toughness and ductility of the composites were reported to be improved [38]. In another study, Huang et al, fabricated CNF decorated flexible and super-hydrophobic polyurethane (PU)/SEBS composite nanofiber membranes. In this study, the nanofiber mat was immersed into the CNF suspension in order to cover the surface of the mat by the fillers. Although the aim of the study was to develop a piezoresistive gas sensor, mechanical properties were also analyzed. Even though CNFs were not compounded with the matrix, attachment of the CNFs on the mat surface was reported to improve the tensile strength and elastic modulus of the flexible nanofibers. This was attributed to the alignment of CNFs and nanofiber mat to the direction of applied force and increase in interfacial area between both phases. As a result of this load transfer and mechanical strength was found to increase [39]. However, in the studies mentioned above, SEBS was not the only matrix and also it was used in order to modify the impact resistance properties of thermoplastics or to tune the spinnability of other thermoplastic elastomers. On the other hand, Dios et al. fabricated SEBS based composites

by using various carbonaceous fillers including CNF. CNF/SEBS nanocomposites were prepared by the combination of sonication and solvent casting. Unlike the studies mentioned above, mechanical strength and elastic modulus of the samples were reported to decrease after the addition of the CNFs. Even though the reason for that was not mentioned in the study, this was probably caused by the solvent casting process. As known, the thickness of the film is very crucial for this process and for thicker films there might be some pores in the structure and those pores lead to the worsening of mechanical properties. The mechanical characterization was also carried out after the annealing of composites and as expected lower tensile stress values were obtained [17]. In another study, Turgut *et al.*, developed CNF/SEBS nanocomposites and investigated their piezoresistive strain sensing behavior. In this study two different SEBS polymers with different block ratios were used. Mechanical and electromechanical properties were investigated. Mechanical properties were reported to increase by the addition of CNFs [16].

In the present study, we have designed, fabricated and characterized the VGCNF filled SEBS nanocomposites. Two different polymers were used in order to investigate the effects of the molecular weight of the polymer on viscosity, morphological and mechanical properties of the samples. VGCNFs at various concentration levels were mixed with SEBS matrix by the high shear mixer in order to obtain good dispersion. Solvent cast samples were compression molded in order to obtain a homogeneous film. Viscosity, morphology and mechanical properties were found to be affected by VGCNF ratio, and matrix molecular weight.

2. Materials and Methods

Two SEBS block copolymers (linear) with S/EB ratio of 30/70 were used. Low molecular weight is shown as SEBS-1 (180 kDa), medium molecular weight is shown as SEBS-2 (250 kDa). White mineral oil (MO) manufactured as Merlot 261 with a molecular weight of 567 g/mol by Petroyag ve Kimyasallar San. Tic. A.Ş./Petroyag Lubricants (Gebze, Kocaeli, TURKEY), was used as received. Toluene (Merck, Germany) was used as a solvent. VGCNFs were purchased from Sigma-Aldrich, USA. The average diameter of VGCNFs is 130 nm and the length of the fibers changes from 20 to 200 μm .

Nanocomposites were fabricated in 3 main steps as shown in Fig. 2. In the first step polymer and mineral oil (MO) were mixed with a ratio of 30:70 (Polymer: MO). Then toluene was added into this mixture with the ratio of 1:2 ((Polymer+MO): toluene). Stirring was performed until complete dissolution was achieved with a magnetic stirrer at 200 rpm for 12 hours at room temperature (25°C). In order to obtain nanocomposites, the relevant amount of VGCNF solution was mixed by a planetary high shear mixer (Kurabo-Mazerustar-KK250, Japan) for 90 sec. After that, the polymer solution was added and mixed for another 90 sec. by a high shear mixer at 1600 rpm. Following that step, the mixture was solution cast in a petri dish and placed in a vacuum oven at 50°C for 12 hours. In the final step, cast films were compression molded into 0.8-0.9 mm thick films by using a laboratory type hot press at 190°C for 15 min. under 0,3 MPa of pressure.

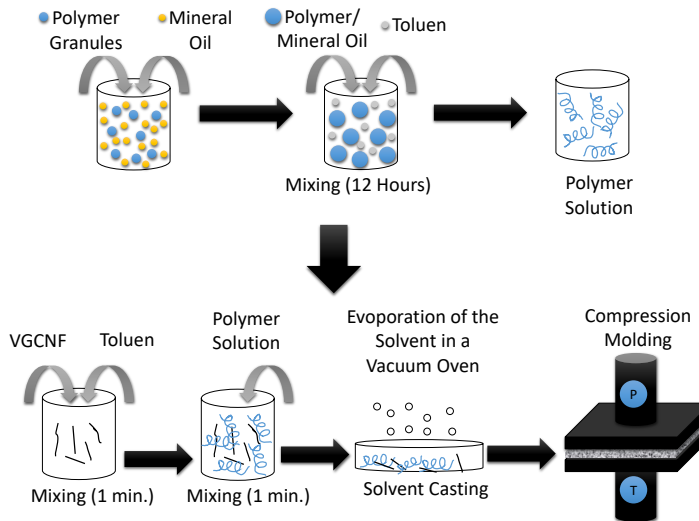


Fig. 2 Preparation of nanocomposites

Viscosity measurements were carried out by a Brookfield DV2T viscometer just after the high-shear mixing. All the measurements were done at 200 rpm with the spindle # 7 at room temperature (25°C). The morphology of nanocomposites was analyzed by scanning electron microscope (FESEM) (5 kV, METU Central Research Laboratory). The stress-strain behavior of the composite films was characterized by a universal load frame (Devotrans, DVT GPU/RD). The test speed was 50 mm/min. For each composite type, 3 specimens with the dimensions of 25 mm x 5mm (length x width) were prepared and tested for load-extension behavior. This test is a modified version of the ASTM 1708 Standard Test Method for Tensile Properties of Plastics by Use of Microtensile Specimens. Since thermoplastic elastomers are highly stretchable, we have used small-sized samples. Otherwise, the maximum jaw distance of the device will be exceeded and complete set of data may not be obtained. The stress-strain graphs were given as true stress vs true strain. Engineering stress and strain were calculated by using the Eq(1) and Eq (2), true stress and strain were calculated by using the Eq (3) and Eq (4):

$$\sigma_E = F / A_0 \quad (1)$$

where σ_E : Engineering stress (MPa), F: Force (N), A_0 : Initial cross sectional area (mm²)

$$\varepsilon_E = (L - L_0) / L_0 = \Delta L / L_0 \quad (2)$$

where ε_E : Engineering strain (mm/mm), L: Final length of sample (mm), L_0 : Initial length of sample (mm), ΔL : Change in length (mm)

$$\sigma_T = \sigma_E (\varepsilon_E + 1) \quad (3)$$

where, σ_T : True stress, σ_E : Engineering stress (MPa), ε_E : Engineering strain (mm/mm)

$$\varepsilon_T = \ln(1 + \varepsilon_E) \quad (4)$$

where, ε_T : True strain ε_E : Engineering strain (mm/mm)

3. Results and Discussions

3.1 Viscosity

The results of the viscosity measurements are given in Table 1 and Fig. 3 as a function of VGCNF for both polymers. As seen from Table 1, SEBS-2 showed higher viscosity. While SEBS-1 polymer solution had a viscosity value of 2.18 cP, SEBS-2 had a value of 16.76 cP. As known higher molecular weight leads to higher molecular chain entanglements and resistance to flow. In addition to that increase in filler concentration resulted in higher viscosity for both polymers. As seen from Fig. 3, viscosity values are 2.26, 2.38, 2.76 cP for 2, 4 and 6 wt % VGCNF/SEBS-1, respectively. Similar to that, other set of samples showed an increase in viscosity and 18.14, 18.9, 19.64 cP are the values for 2, 4 and 6 wt % VGCNF containing SEBS-2 samples respectively. As known, VGCNFs are rigid fillers with high elastic modulus. Addition of those rigid materials into the polymer solution increases the rigidity of the system and causes an increase in the viscosity [40, 41]. In order to understand the response of the two sample sets and to provide a better comparison, normalized viscosity (NV) was also calculated for the samples by dividing the viscosity of VGCNF filled sample to the viscosity of polymer solution (η/η_0). NV of the samples are 1.036, 1.092, 1.26 for 2, 4 and 6 wt % VGCNF/SEBS-1, respectively and 1.082, 1.127, 1.171 for 2, 4 and 6 wt % VGCNF/SEBS-2, respectively. As seen in Fig. 4, while SEBS-2 showed a linear fit, SEBS-1 showed a polynomial fit and 6 wt % VGCNF/SEBS-1 sample showed a drastic change in NV around 27 %. This is explained as rheological percolation. Rheological percolation is the value at which VGCNF bundles come very close to form the percolation network. Similar to the electrical percolation, at this point fillers form a continuous network throughout the sample and the change in viscosity is not linear anymore. Since SEBS-2 has relatively high viscosity, rheological percolation was not observed at 6 wt%. It will be probably observed at higher filler concentrations. In addition to that, as will be explained in SEM results, agglomeration of the fillers and cluster formation might also retard this region to higher filler concentrations [41].

Table 1. Viscosity and normalized viscosity values of the samples

Polymer	Filler Ratio (wt%)	Viscosity (cP)	Normalized Viscosity (η/η_0)
SEBS-1	0	2.18	1
	2	2.26	1.036
	4	2.38	1.091
	6	2.76	1.266
SEBS-2	0	16.76	1
	2	18.14	1.082
	4	18.9	1.127
	6	19.64	1.171

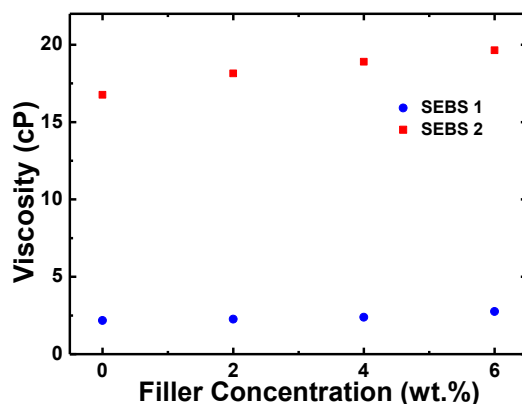


Fig. 3 Viscosity values as a function of VGCNF concentration for SEBS-1 and SEBS-2

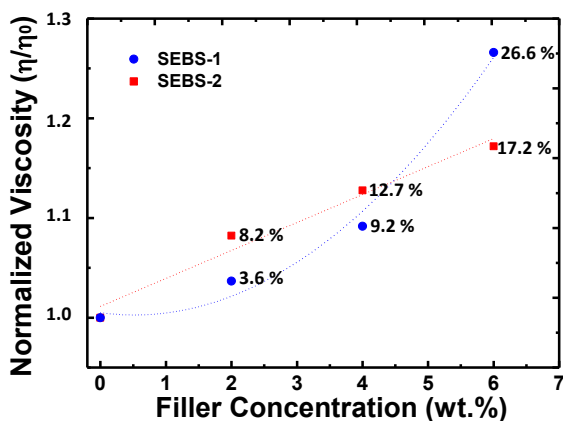


Fig. 4 Normalized viscosity values and the % increase in normalized viscosity as a function of VGCNF concentration for SEBS-1 and SEBS-2

3.2 Morphological Characterization

In order to examine the morphology of the samples; both SEBS films and VGCNF filled nanocomposites were cryo-fractured in liquid nitrogen and cross-sections of the samples were analyzed by FESEM. Fig 5 a and e are SEBS-1 and SEBS-2 films, respectively. As seen, both SEBS-1 and SEBS-2 showed classical fractured surface morphology. It can also be inferred from the images that both samples were melted completely under determined processing conditions. In order to understand the VGCNF dispersion, orientation and filler-matrix interface all nanocomposites were analyzed. SEBS-1 based nanocomposites (Fig. 5 b-d) showed homogeneous filler dispersion for all concentrations. In addition to these, no pores, pulled out VGCNFs, or matrix discontinuity were observed. VGCNF/SEBS-1 composites were found to show a good filler-matrix interface. The good matrix-filler interaction is probably due to well-dispersed fibers (high-shear mixing), high-temperature processing (melt processing), and nanoscale surface roughness of the VGCNF particles.

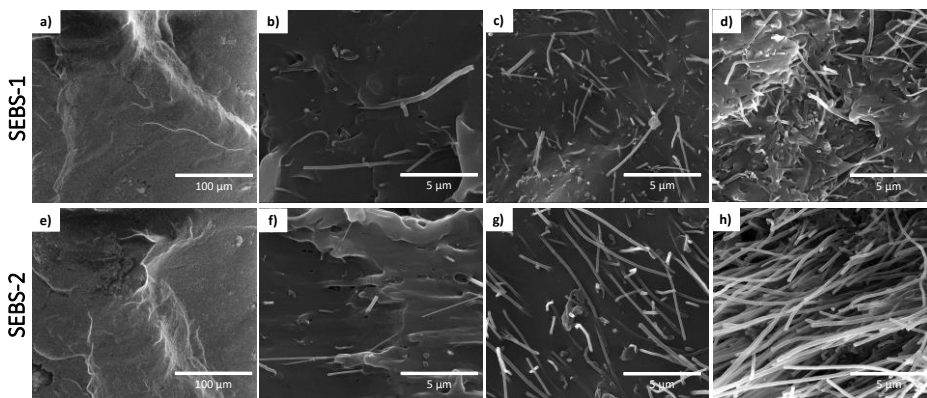


Fig. 5 Cross-sectional SEM images of a) SEBS-1 film b) 2 wt % VGCNF/SEBS-1 c) 4 wt % VGCNF/SEBS-1 d) 6 wt % VGCNF/SEBS-1 e) SEBS-2 film f) 2 wt % VGCNF/SEBS-2 g) 4 wt % VGCNF/SEBS-2 h) 6 wt % VGCNF/SEBS-2

High shear mixing is a one-step, easy and effective way of dispersing nanofillers in a polymeric matrix. Also, it lowers the matrix viscosity during the process by which the matrix-filler interaction is enhanced [18]. SEBS-2 nanocomposites (Fig. 5 f-g) showed almost same behavior as SEBS-1. On the other hand, at high filler concentrations such as 6 wt% VGCNF/SEBS-2 composite, some filler clusters were observed. In Fig. 5h one of those clusters is shown. As obvious from the image the wetting of VGCNFs was not completed. That was probably caused by not only high filler concentration but also higher solution viscosity of SEBS-2 polymer. As previously mentioned in the viscosity analysis, the higher molecular weight causes higher interaction between polymer macromolecules and interlocking of the macromolecular chains will increase the viscosity of the polymer solution [18]. In our case, as shown in Fig. 6, higher viscosity of the SEBS-2 polymer solution led to nonhomogeneous filler dispersion throughout the matrix. This is also parallel with the mechanical data shown in Fig. 8. In other words, under the same processing conditions, solution of the low molecular weight polymer can be mixed more efficiently with the fillers and that leads to better wetting and filler dispersion [18].

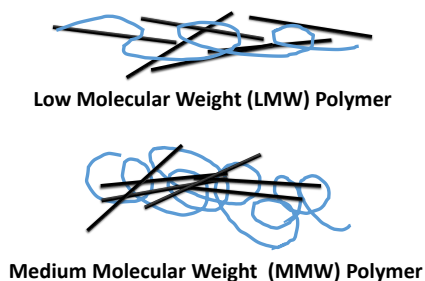


Fig. 6 Dispersion characteristics of VGCNF in LMW and MMW SEBS

3.3 Mechanical Characterization

True stress-strain and elastic modulus values of SEBS films, VGCNF/SEBS-1, and VGCNF/SEBS-2 nanocomposites can be seen from Table 2 and Fig.7 and 8.

Table 2. Mechanical properties of the samples

Polymer	Filler Ratio (wt%)	Maximum True Stress (MPa)	Maximum True Strain (mm/mm)	True Elastic Modulus (MPa)
SEBS-1	0	4.558	2.3	0.164
	2	4.887	2.3	0.241
	4	6.095	2.3	0.341
	6	7.770	2.3	0.534
SEBS-2	0	8.847	2.3	0.197
	2	10.369	2.3	0.254
	4	12.255	2.3	0.407
	6	11.626	2.3	0.726

All samples showed a linear elastic deformation behavior at low strain. As seen in Fig. 7-8, SEBS-2 film showed better mechanical properties and elastic modulus compared to SEBS-1. This is caused by the higher molecular weight of SEBS-2. Longer macromolecular chains increase the interlocking and that leads to better mechanical properties. As clearly seen from both figures, an increase in the VGCNF wt % content leads to an increase in stress values. The incorporation of filler increases the load-bearing capacity of the composites. As previously reported in the literature VGCNF has relatively high elastic modulus when compared with polymeric materials. In the case of homogeneous mixing of VGCNF and SEBS, the mechanical properties of the nanocomposites enhanced. VGCNF increases the mechanical properties not only because of its rigid structure but also surface properties.

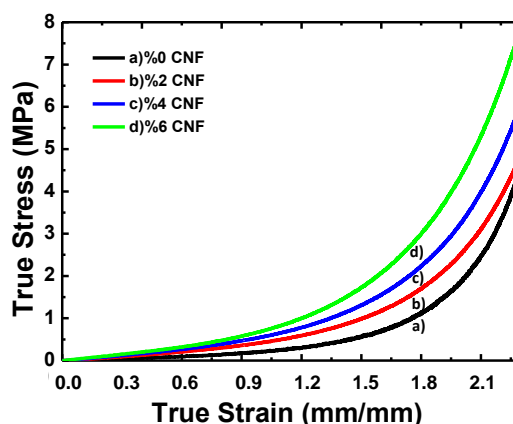


Fig. 7 True stress-strain graphs SEBS-1 film and VGCNF/SEBS-1 nanocomposites

As known, VGCNFs have a nano-scale surface roughness that helps to increase filler-matrix interaction and mechanical interlocking that leads to a good filler-matrix interface [18, 30]. On the other hand, 6 wt % VGCNF filled SEBS-2 composite showed a decrease in stress value at high level of strain. That is probably caused by the formation of some filler clusters at this concentration which is consistent with the FESEM images included in Fig. 5 h. As previously mentioned, that is probably caused by higher viscosity of the SEBS-2 polymer solution. Viscosity of the SEBS-2 is around 8 times higher than SEBS-1 solution and the viscosity of 6% VGCNF/SEBS-2 mixture is 6 times higher than of 6% VGCNF/SEBS-1.

Incorporation of fillers led to higher viscosity that prevents effective mixing and filler dispersion at a given time. This might be prevented by addition of more solvent or increased mixing time.

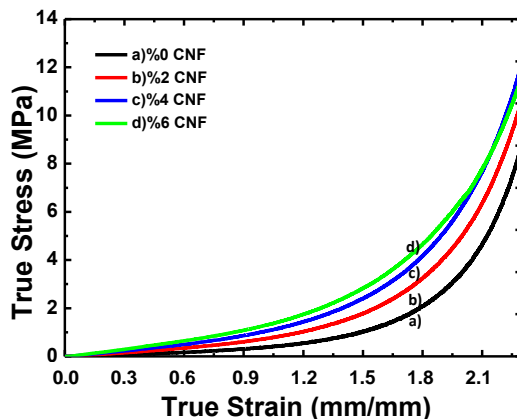


Fig. 8 Stress-strain graphs of SEBS-2 film and VGCNF/SEBS-2 nanocomposites

In addition to stress values and mechanical strength, strain values can also be analyzed from stress-strain curves. SEBS-1, SEBS-2 films can be more than 9 times their original length. No difference was observed between two polymers in terms of strain levels. These strain values are very high when compared to traditional vulcanized rubber or thermoplastics. It is also obvious that the addition of nanofillers did not affect the strain values. In other words, regardless of the polymer type, all nanocomposites can be stretched more than 9 times compared to their initial length.

4. Conclusions

In this study, flexible polymer nanocomposites were prepared by using poly[styrene-*b*-(ethylene-co-butylene)-*b*-styrene] and vapor grown carbon nanofibers that can be stretched more than 9 times their original length. Nanocomposites were prepared at various levels of VGCNFs 0, 2, 4 and 6 wt % by using two different SEBS. SEBS-1 and SEBS-2 have the same block ratio (S/EB : 30/70) and they have different molecular weights (SEBS-1: 180 kDa; SEBS-2: 250 kDa). In order to obtain homogeneous VGCNF dispersion, a planetary high shear mixer was used. Composites were prepared by the combination of solvent casting and compression molding. Morphological characterization showed homogeneous filler dispersion without any dominant filler orientation throughout the composites with good filler-matrix interface and absence of any pores or voids. That was caused by two-step fabrication method. High shear mixing is a very effective method for dispersion of the VGCNFs. In addition to that, pressure application during compression molding led to the removal of the solvent completely and increase the filler-matrix interface. Nanofiber clusters were observed for only 6 wt % VGCNF filled SEBS-2 nanocomposite. Mechanical properties were characterized by a mechanical testing system as a function of VGCNF and polymer type. SEBS-2 film showed higher stress values compared to SEBS-1. This is caused by the higher molecular weight of SEBS-2. For both systems, incorporation of filler increases the load-bearing capacity of the composites. VGCNF increases the mechanical properties of the composite system not only because of its rigid structure but also its surface properties. As known, VGCNFs have nano-scale surface roughness that helps to increase filler-matrix interaction and mechanical interlocking that leads to a good filler-matrix interface.

From the outcomes of the present study, the following conclusions can be drawn:

- Highly flexible polymer nanocomposites that can be stretched more than 9 times compared to their initial length were successfully fabricated,
- Molecular weight of polymer directly affects the solution viscosity and filler dispersion,
- Increased polymer molecular weight and filler ratio led to increase in viscosity,
- Homogeneous filler dispersion was obtained for almost all nanocomposites,
- At higher VGCNF concentrations, filler dispersion was not very homogeneous for the polymer with higher molecular weight,
- Films and nanocomposites fabricated by using higher molecular weight polymer showed better mechanical properties,
- Mechanical strength of the nanocomposites increased by the addition of VGCNF regardless of the polymer molecular weight,
- Depending on the requirements, both systems can be used for many applications including, conductive coatings, electromagnetic shielding applications, flexible electronics, wearable electronics and polymeric sensors.

Acknowledgement

This work was supported by Yalova University, Project No. 2018/YL/0006, Yalova University, Project No. 2018/YL/0019 and TUBITAK 2210-C National Graduate Scholarship Program in High Priority Technological Areas (TUBITAK 2210-C Oncelikli Alanlara Yonelik Yurt Ici Yuksek Lisans Burs Programi)

References

- [1] Lorenzo M, Zhu B, Srinivasan G. Intrinsically flexible electronic materials for smart device applications. *Green Chemistry*, 2016;18(12): 3513-7. <https://doi.org/10.1039/C6GC00826G>
- [2] Gao F, Zhang N, Fang X, Ma M. Bioinspired design of strong, tough, and highly conductive polyol-polypyrrole composites for flexible electronics. *ACS applied materials & interfaces*, 2017; 9(7): 5692-8. <https://doi.org/10.1021/acsami.7b00717>
- [3] Li W, Gao F, Wang X, Zhang N, Ma M. Strong and robust polyaniline-based supramolecular hydrogels for flexible supercapacitors. *Angewandte Chemie International Edition*, 2016; 55(32): 9196-201. <https://doi.org/10.1002/anie.201603417>
- [4] Oh JY, Kim S, Baik HK, Jeong U. Conducting polymer dough for deformable electronics. *Advanced Materials*, 2016; 28(22): 4455-61. <https://doi.org/10.1002/adma.201502947>
- [5] Wang L-X, Li X-G, Yang Y-L. Preparation, properties and applications of polypyrroles. *Reactive and Functional Polymers*, 2001; 47(2): 125-39. [https://doi.org/10.1016/S1381-5148\(00\)00079-1](https://doi.org/10.1016/S1381-5148(00)00079-1)
- [6] Lan Y, Liu H, Cao X, Zhao S, Dai K, Yan X, et al. Electrically conductive thermoplastic polyurethane/polypropylene nanocomposites with selectively distributed graphene. *Polymer*, 2016; 97: 11-9. <https://doi.org/10.1016/j.polymer.2016.05.017>
- [7] Chen Y, Li Y, Xu D, Zhai W. Fabrication of stretchable, flexible conductive thermoplastic polyurethane/graphene composites via foaming. *RSC Advances*, 2015; 5(100): 82034-41. <https://doi.org/10.1039/C5RA12515D>
- [8] Mao C, Zhu Y, Jiang W. Design of electrical conductive composites: tuning the morphology to improve the electrical properties of graphene filled immiscible polymer blends. *ACS applied materials & interfaces*, 2012; 4(10): 5281-6. <https://doi.org/10.1021/am301230q>

- [9] Zabihi O, Khodabandeh A, Mostafavi SM. Preparation, optimization and thermal characterization of a novel conductive thermoset nanocomposite containing polythiophene nanoparticles using dynamic thermal analysis. *Polymer degradation and stability*, 2012; 97(1): 3-13. <https://doi.org/10.1016/j.polymdegradstab.2011.10.022>
- [10] Kumar V, Yokozeki T, Goto T, Takahashi T. Mechanical and electrical properties of PANI-based conductive thermosetting composites. *Journal of Reinforced Plastics and Composite*, 2015; 34(16): 1298-305. <https://doi.org/10.1177/0731684415588551>
- [11] Filiatrault HL, Porteous GC, Carmichael RS, Davidson GJ, Carmichael TB. Stretchable light-emitting electrochemical cells using an elastomeric emissive material. *Advanced Materials*, 2012; 24(20): 2673-8. <https://doi.org/10.1002/adma.201200448>
- [12] Park J, Wang S, Li M, Ahn C, Hyun JK, Kim DS, et al. Three-dimensional nanonetworks for giant stretchability in dielectrics and conductors. *Nature communications*, 2012; 3:916. <https://doi.org/10.1038/ncomms1929>
- [13] Yamada T, Hayamizu Y, Yamamoto Y, Yomogida Y, Izadi-Najafabadi A, Futaba DN, et al. A stretchable carbon nanotube strain sensor for human-motion detection. *Nature nanotechnology*, 2011; 6(5): 296. <https://doi.org/10.1038/nnano.2011.36>
- [14] Liu H, Li Y, Dai K, Zheng G, Liu C, Shen C, et al. Electrically conductive thermoplastic elastomer nanocomposites at ultralow graphene loading levels for strain sensor applications. *Journal of Materials Chemistry C*, 2016; 4(1): 157-66. <https://doi.org/10.1039/C5TC02751A>
- [15] Costa P, Silva J, Sencadas V, Simoes R, Viana J, Lanceros-Méndez S. Mechanical, electrical and electro-mechanical properties of thermoplastic elastomer styrene-butadiene-styrene/multiwall carbon nanotubes composites. *Journal of Materials Science*, 2013; 48(3): 1172-9. <https://doi.org/10.1007/s10853-012-6855-7>
- [16] Turgut A, Tuhin MO, Toprakci O, Pasquinelli MA, Spontak RJ, Toprakci HA. Thermoplastic Elastomer Systems Containing Carbon Nanofibers as Soft Piezoresistive Sensors. *ACS Omega*, 2018; 3(10): 12648-57. <https://doi.org/10.1021/acsomega.8b01740>
- [17] Dios JR, García-Astrain C, Costa P, Viana JC, Lanceros-Méndez S. Carbonaceous Filler Type and Content Dependence of the Physical-Chemical and Electromechanical Properties of Thermoplastic Elastomer Polymer Composites. *Materials*, 2019; 12(9): 1405. <https://doi.org/10.3390/ma12091405>
- [18] Toprakci HAK. (2012). Piezoresistive Properties of Polyvinyl Chloride Composites. Ph.D. Dissertation, North Carolina State University, North Carolina.
- [19] Gibson RF. A review of recent research on mechanics of multifunctional composite materials and structures. *Composite structures*, 2010; 92(12): 2793-810. <https://doi.org/10.1016/j.compstruct.2010.05.003>
- [20] Farajpour A, Ghayesh MH, Farokhi H. A review on the mechanics of nanostructures. *International Journal of Engineering Science*, 2018; 133: 231-63. <https://doi.org/10.1016/j.ijengsci.2018.09.006>
- [21] Drobny J. *Handbook of Thermoplastic Elastomers*, William Andrew Inc. Norwich, NY. 2014. <https://doi.org/10.1016/B978-0-323-22136-8.00012-0>
- [22] Shanks R, Kong I. *Thermoplastic Elastomers*, Intech publishing Rijeka, Croatia; 2012. <https://doi.org/10.5772/36807>
- [23] Visakh P.M, Thomas S, Chandra A.K., Mathew A.P. *Advances in Elastomers I*: Springer Berlin-Heidelberg, Germany, 2013. <https://doi.org/10.1007/978-3-642-20928-4>
- [24] Amin S, Amin M. Thermoplastic elastomeric (TPE) materials and their use in outdoor electrical insulation. *Rev Adv Mater Sci*, 2011; 29(2011): 30-15.
- [25] Mark J, Erman B, Roland M. *The Science and Technology of Rubber*, Academic Press, Boston, 2013.

- [26] Pavlovsky S, Siegmann A. Chemical sensing materials. I. Electrically conductive SEBS copolymer systems. *Journal of applied polymer science*, 2009; 113(5): 3322-9. <https://doi.org/10.1002/app.30310>
- [27] Melnykowycz M, Koll B, Scharf D, Clemens F. Comparison of piezoresistive monofilament polymer sensors. *Sensors*, 2014; 14(1): 1278-94. <https://doi.org/10.3390/s140101278>
- [28] Albers WM, Karttunen M, Wikström L, Vilkman T. Effects of compression and filler particle coating on the electrical conductivity of thermoplastic elastomer composites. *Journal of electronic materials*, 2013; 42(10): 2983-9. <https://doi.org/10.1007/s11664-013-2689-6>
- [29] Li Y, Shimizu H. Toward a stretchable, elastic, and electrically conductive nanocomposite: morphology and properties of poly [styrene-b-(ethylene-co-butylene)-b-styrene]/multiwalled carbon nanotube composites fabricated by high-shear processing. *Macromolecules*, 2009; 42(7): 2587-93. <https://doi.org/10.1021/ma802662c>
- [30] Al-Saleh MH, Sundararaj U. A review of vapor grown carbon nanofiber/polymer conductive composites. *Carbon*, 2009; 47(1): 2-22. <https://doi.org/10.1016/j.carbon.2008.09.039>
- [31] Kuriger RJ, Alam MK, Anderson DP, Jacobsen RL. Processing and characterization of aligned vapor grown carbon fiber reinforced polypropylene. *Composites Part A: Applied Science and Manufacturing*, 2002; 33(1): 53-62. [https://doi.org/10.1016/S1359-835X\(01\)00070-7](https://doi.org/10.1016/S1359-835X(01)00070-7)
- [32] Al-Saleh MH, Sundararaj U. Review of the mechanical properties of carbon nanofiber/polymer composites. *Composites Part A: Applied Science and Manufacturing*, 2011; 42(12): 2126-42. <https://doi.org/10.1016/j.compositesa.2011.08.005>
- [33] Al-Saleh MH, Sundararaj U. Processing-microstructure-property relationship in conductive polymer nanocomposites. *Polymer*, 2010; 51(12): 2740-7. <https://doi.org/10.1016/j.polymer.2010.03.022>
- [34] Liao CZ, Tjong SC. Effects of carbon nanofibers on the fracture, mechanical, and thermal properties of PP/SEBS-g-MA blends. *Polymer Engineering & Science*, 2011; 51(5): 948-58. <https://doi.org/10.1002/pen.21903>
- [35] Luo Z, Koo JH. Quantitative study of the dispersion degree in carbon nanofiber/polymer and carbon nanotube/polymer nanocomposites. *Materials letters*, 2008; 62(20): 3493-6. <https://doi.org/10.1016/j.matlet.2008.03.010>
- [36] Kabir ME, Saha M, Jeelani S. Effect of ultrasound sonication in carbon nanofibers/polyurethane foam composite. *Materials Science and Engineering: A*, 2007; 459(1-2): 111-6. <https://doi.org/10.1016/j.msea.2007.01.031>
- [37] Bal S. Experimental study of mechanical and electrical properties of carbon nanofiber/epoxy composites. *Materials & Design (1980-2015)*, 2010; 31(5): 2406-13. <https://doi.org/10.1016/j.matdes.2009.11.058>
- [38] Parameswaranpillai J, Joseph G, Shinu K, Salim NV, Hameed N, Jose S. High performance PP/SEBS/CNF composites: Evaluation of mechanical, thermal degradation, and crystallization properties. *Polymer Composites*, 2017; 38(11): 2440-9. <https://doi.org/10.1002/pc.23830>
- [39] Gao J, Wang H, Huang X, Hu M, Xue H, Li RK. A super-hydrophobic and electrically conductive nanofibrous membrane for a chemical vapor sensor. *Journal of Materials Chemistry A*, 2018; 6(21): 10036-47. <https://doi.org/10.1039/C8TA02356E>
- [40] Litchfield DW, Baird DG. The rheology of high aspect ratio nano-particle filled liquids. *Rheology Reviews*, 2006; 2006:1.
- [41] Du F, Scogna RC, Zhou W, Brand S, Fischer JE, Winey KI. Nanotube networks in polymer nanocomposites: rheology and electrical conductivity. *Macromolecules*, 2004; 37(24): 9048-55. <https://doi.org/10.1021/ma049164g>

Blank Page



Preparation and characterization of a new adsorbent from *Raphia taedigera* seed

Emmanuel Folorunso Olasehinde^{1,a}, Segun Michael Abegunde^{*2,b}

¹Department of Chemistry, Federal University of Technology, Akure, Nigeria

²Department of Science Technology, Federal Polytechnic, Ado-Ekiti, Ekiti State, Nigeria

Article Info

Abstract

Article history:

Received 13 Jul 2019

Revised 10 Sep 2019

Accepted 16 Sep 2019

Keywords:

Raphia taedigera;

adsorbent;

carbonization;

activation;

methylene blue;

SEM

There has been widespread research and engagement in recent years on the use of plant material in preparing porous carbon for wastewater treatment. In this study, new biochars (BCs) impregnated with 0.1 M sulphuric acid (RTA) and 0.1 M sodium hydroxide (RTB) were prepared. The BCs and raw seed [RTR] were characterized using scanning electron microscopy (SEM), Fourier-transform infrared (FTIR) spectrophotometer, and thermogravimetric/Differential thermal analyser. [TGA/DTA] to determine their morphology, spectral bands and thermal behaviour respectively. RTR showed a scattered aggregated surface microstructure, while both RTA and RTB gave aggregated rough surfaces with high number of pores. The FTIR analysis showed significant changes in term of band shift, bands disappearances, and new band formations due to pyrolysis and activation of the BCs. The results of the TGA/DTA revealed that RTA and RTB have better thermal stability than RTR, with the maximum degradation temperature of RTR, RTA, and RTB occurred at 380°C, 425°C and 410°C respectively. Adsorption efficiencies ranged from 81.671 to 99.743% for performance evaluation on the BCs using different adsorbent dosages and the initial concentrations of methylene blue solutions. These preliminary investigations suggest that biochars prepared from *Raphia taedigera* seed can be used for methylene blue removal from wastewater.

© 2019 MIM Research Group. All rights reserved.

1. Introduction

In recent years, heavy metals and textile dyes have been considered the most ubiquitous contaminants of water worldwide. Water pollution is a major concern in our environment, and so providing a solution to this issue will be of obvious benefit to humans [1]. Over the years, adsorption has been recognized as one of the most reliable and efficient methods of removing organic and inorganic pollutants from industrial wastewater. Activated carbon (AC) has been undoubtedly recognized as the most common and widely employed adsorbent for wastewater treatment, given its simplicity of use, low cost, renewable nature, availability, and non-toxicity; its porous structure over large surface areas makes it a material of choice as an effective adsorbent [2 - 4]. With the introduction of stricter environmental regulations, the demand for porous carbons has progressively increased [5, 6]. Recently, there have been reports on several

*Corresponding author: abegundes@gmail.com

^a orcid.org/0000-0002-3909-1283; ^b orcid.org/0000-0002-6688-5230

DOI: <http://dx.doi.org/10.17515/resm2019.139ma0713>

Res. Eng. Struct. Mat. Vol. 6 Iss. 2 (2020) 167-182

treatment processes by which to remove contaminants from wastewater, including degradation by photocatalytic processes [7–12]; the Fenton process [13]; photo-Fenton processes [14]; sono-chemical degradation [15]; chemical coagulation/flocculation, ozonation, cloud point extraction, oxidation, nano-filtration, chemical precipitation, ion exchange, reverse osmosis, and ultra-filtration [16–20]; and modified processes such as those combining ultrasound with adsorption-desorption processes [21–24]. However, among these, adsorption techniques have gained favour, owing to their simplicity, cost-effectiveness, and efficiency in removing pollutants that are too stable for conventional methods [8, 25–29]. Recently, the idea of using locally sourced materials to prepare adsorbent materials for water and effluent treatment has gained popularity among environmentalists and material engineers. Given the exorbitant cost of commercial AC, there is a need to develop a low-cost and high-performance adsorbent from readily available and locally sourced alternative materials. Several agricultural waste products have been utilized [30], including cotton stalks [31], cereal by-product [6], bamboo [32], acorn shells [33], groundnut shells [34, 35], bagasse [36], cow bone powder [37], palm oil stones [38], coconut shells [39], tobacco residues [40], olive stones [41], apricot stones [42], nutshells [43], walnut shells [41], pine cones [44], and cherry stones [45].

Little information is currently available on *Raphia taedigera*, despite having been in existence for centuries. The plant remains quantitatively and qualitatively untapped in terms of their potential applications. *R taedigera* is native to Brazil, Cameroon, Costa Rica, Nicaragua, Nigeria, and Panama [46–50], and grows in swampy forests along streams. It produces egg-sized fruits of about 5–7 cm long and 3 cm in diameter, which are covered by imbricate glossy reddish-brown scales; each fruit contains one seed. A well-dried seed is hard and has a brown outer part and white shiny inner part.

In literature, no study has clearly evaluated the possibility of using *R taedigera* seed as an adsorbent. With recent developments in the need to source locally for available materials to prepare adsorbent, since metal ion and dye pollutants pose a serious threat to biological and environmental sources, given their harmful effects on human health and the environment [51, 52] hence; a need to check the potential of *R. taedigera* seed as a useful adsorbent. This present study is aimed at preparation and characterization of adsorbent from *Raphia taedigera* seed considered as waste, for the recovery of methylene blue dye from aqueous solution.

2. Materials and Methods

2.1. Sample collection and treatment

R. taedigera seeds were obtained locally from a farmland in Ise-Ekiti, washed and sun-dried for several days until moisture evaporation was completed. The dried samples were crushed using 911MPE-24 laboratory crusher. The crushed sample was kept in an airtight plastic container for further analysis.

2.2. Preparation of *Raphia taedigera* adsorbent

2.2.1. Carbonization of samples

The carbonization was done as reported by [53]. The dried and crushed *R. taedigera* seeds were carbonized by placing 100 g of the seed in a muffle furnace (Carbolite, Sheffield, England, LMF4) at 350°C for about 2 hours. During carbonization, an exhaust pipe was used to remove steam to set the process oxygen-deficient. This made the material to thermally decompose to porous carbonaceous materials and compounds of the hydrocarbon. After the carbonization process, the carbonized biochars were

allowed to cool to room temperature, washed with double distilled water to a pH of about 7 and dried to constant weight in an oven at 105°C. The carbonized biochars were sieved with 100-mm mesh Tyler sieve and kept in an airtight polythene bag.

2.2.2. Activation of the carbonized samples

The activation was done as reported by [53]. Both acidic and basic activations were done on the material. 20 g carbonized material was carefully weighed and quantitatively transferred into a clean and dry 500 mL beaker containing 200 mL 0.1 M sulphuric acid for acidic activation and 200 mL of 0.1 M sodium hydroxide was used for alkaline activation of another 20 g of the carbonized material. The contents of the beakers were carefully homogenized and left to stand for about 24 hours. The impregnated materials were diluted with 200 mL distilled water to rinse off the sulphuric acid and sodium hydroxide used as activating agents respectively. The process of washing continued until the pH of 7.0 was attained and transferred into an oven and dried to constant weight at 105°C for about 4 hours. It was sieved with 100-mm mesh to obtain a fine powder of *Raphia taedigera* activated biochars for both the acid (RTA) and the base (RTB). The RTA, RTB, and RTR (raw *Raphia taedigera* seed powder) were stored in a separate airtight plastic container for further use.

2.3. Material Characterization

The morphology of the samples was carried out using scanning electron microscopy (SEM) to evaluate the microstructure characteristics. TGA/DTA was used to determine the thermal behaviour of the samples using thermogravimetric Analyzer Perkin-Elmer TGA 4000 at the temperature range of 30 - 900°C while Fourier-transform infrared spectrophotometer (FTIR) was engaged to evaluate the molecular bonding present in the materials.

2.4. Preparation of Methylene Blue (MB)

100 mg/L of methylene blue (MB) stock solution was prepared by quantitatively dissolving 0.1 g MB in distilled water in 1,000 mL volumetric flask and made up to the mark with distilled water. The maximum absorption wavelength was determined by UV spectrophotometer. 0.1 M of HCl and 0.1 M NaOH solutions were also prepared to adjust the pH. All reagents used were of analytical grade.

2.5. Evaluation of Effect some Parameters on the Adsorption

2.5.1. Effect of Adsorbent Dose

The effect of the adsorbent dose was experimented using different adsorbent dosages of 0.1 g, 0.3 g, 0.5 g, 0.7 g and 0.9 g. 10 mL of 100 mg/L MB was introduced into a beaker containing each of the adsorbent doses for 15 minutes at room temperature. The solution was filtered, and the concentrations of the filtrates were determined using a UV spectrophotometer and the amount of MB adsorbed was calculated using Eq 1.

$$q_e = \frac{(C_0 - C_e)V}{W} \quad (1)$$

Where, q_e is the amount of MB adsorbed per unit mass in mg/g, C_0 is the initial MB concentration in mg/L, C_e is the MB concentration at equilibrium in mg/L, V is the volume of MB solution in liter and W is the mass of the adsorbent in grams.

The adsorption efficiency was calculated using the equation below:

$$\text{Adsorption efficiency} = \frac{(C_o - C_e)}{C_o} \times 100 \quad (2)$$

2.5.2. Effect of Initial Solution Concentration

The effect of initial concentrations of MB was evaluated using different concentrations of 20 mg/L, 40 mg/L, 60 mg/L, 80 mg/L and 100mg/L. 0.5 g of the adsorbent was introduced into a conical flask containing 10 mL of each of the solution and allowed to stand for 15 minutes at room temperature. The solution was filtered, and the concentrations of the filtrates were determined. The amount of MB adsorbed and percentage efficiency of the adsorbents were calculated using equations 1 and 2 respectively.

3. Results and Discussion

3.1. Surface morphology studies.

The surface morphology studies of RTR, RTA and RTB were done using Scanning electron microscopy and presented in Figures 1, 2 and 3 respectively. The photomicrographs at a magnification of 300x, 500x and 1000x are given as A, B and C respectively. As expected, pyrolysis and surface activation, altered to a noticeable level, the surface morphologies of the biochars (RTA and RTB) compared to raw *Raphia taedigera* (RTR). Figure 1 shows scattered aggregated surface, while figures 2 and 3 show aggregated and rough surface morphology with links between the surface particles creating many more pores at the surfaces. The roughness and uneven nature of the surfaces observed in figures 2 and 3 are due to the activation of the porous carbon using H_2SO_4 and NaOH solutions respectively.

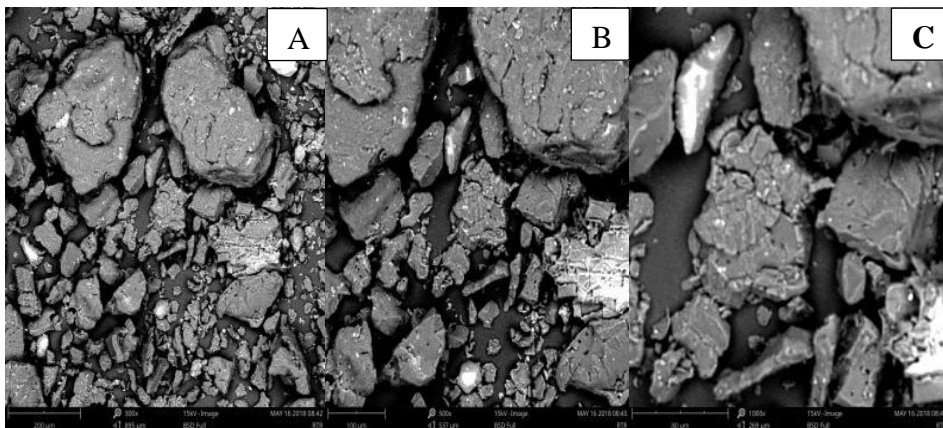


Fig. 1. SEM images of RTR at 300x (A), 500x (B) and 1000x (C)

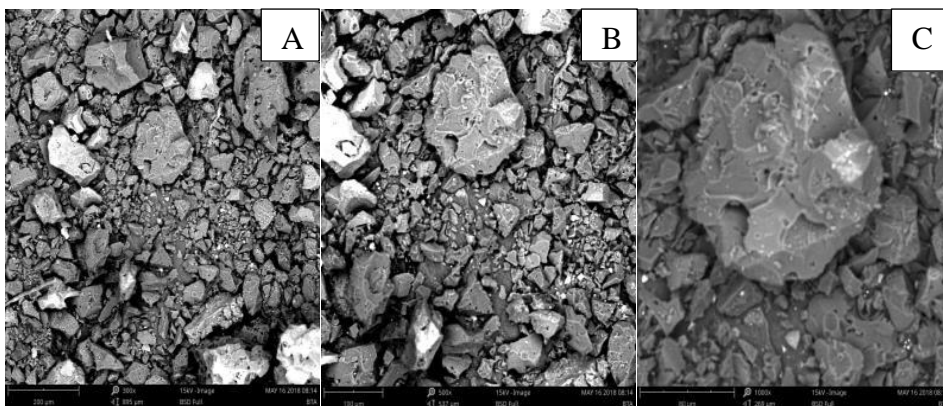


Fig. 2. SEM images of RTA at 300x (A), 500x (B) and 1000x (C).

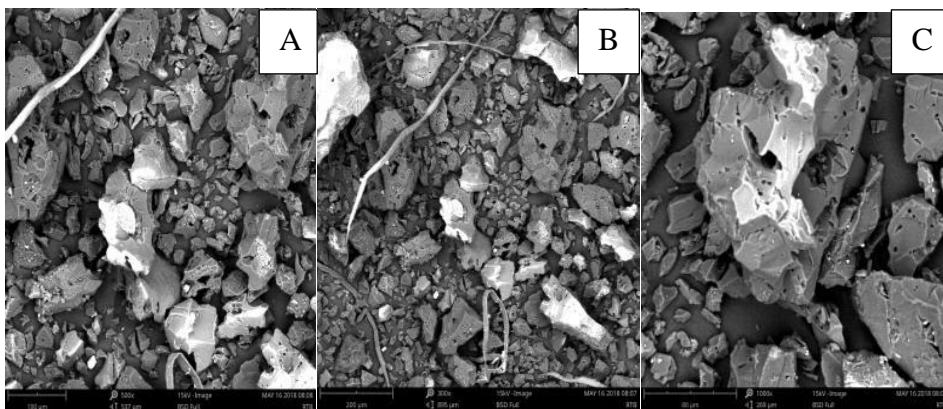


Fig. 3. SEM images of RTB at 300x (A), 500x (B) and 1000x (C)

3.2. FTIR Spectral Analysis

Figures 4, 5 and 6 show the FTIR spectra of raw *R. taedigera* seed powder, acid activated *R. taedigera* seed and base activated *R. taedigera* seed respectively. Again significant changes were observed in the materials in term of band shift, band disappearances and new band formations due to pyrolysis and activation of RTA and RTB. As shown in the spectra, a strong and sharp band at about $3700 - 3500 \text{ cm}^{-1}$ due to free OH group, a broad band at $3600 - 3200 \text{ cm}^{-1}$ representing bonded OH group, a band at about $3000 - 2850 \text{ cm}^{-1}$ corresponding to aliphatic C-H group, a band at about $1820 - 1670 \text{ cm}^{-1}$ indicating C=O stretch, a band in about $1385 - 1345 \text{ cm}^{-1}$ indicating N-O stretch of nitro molecule, a band at about $1300 - 1000 \text{ cm}^{-1}$ corresponds to C-O stretch of ester and a strong band at about $800 - 600 \text{ cm}^{-1}$ indicating C-Cl of alkyl halide were observed in the three materials. Comparing the spectra of RTA and RTB (Figures 5 and 6) with RTR (figure 4), two new bands corresponding to free OH group at about $3700 - 3500 \text{ cm}^{-1}$, new band at about $1600 - 1400 \text{ cm}^{-1}$ corresponding to C=C of aromatic and a band at about 1354 cm^{-1} corresponding to C-N stretching of amine were observed. However, the extra band at 2374 cm^{-1} indicating CN stretch of nitrile and a band at 1241 cm^{-1} corresponding to CN stretch of amine observed in RTA spectral were not found in RTB spectral. The changes in the FTIR spectra of the materials may be due to the introduction of activating agents for surface modifications [54, 53] of RTA and RTB.

Undoubtedly, the shifts in the spectra indicated the prepared materials would be of great use as adsorbents for heavy metals and dye removal. This is in line with reports of previous studies as reported by [55, 56, 57].

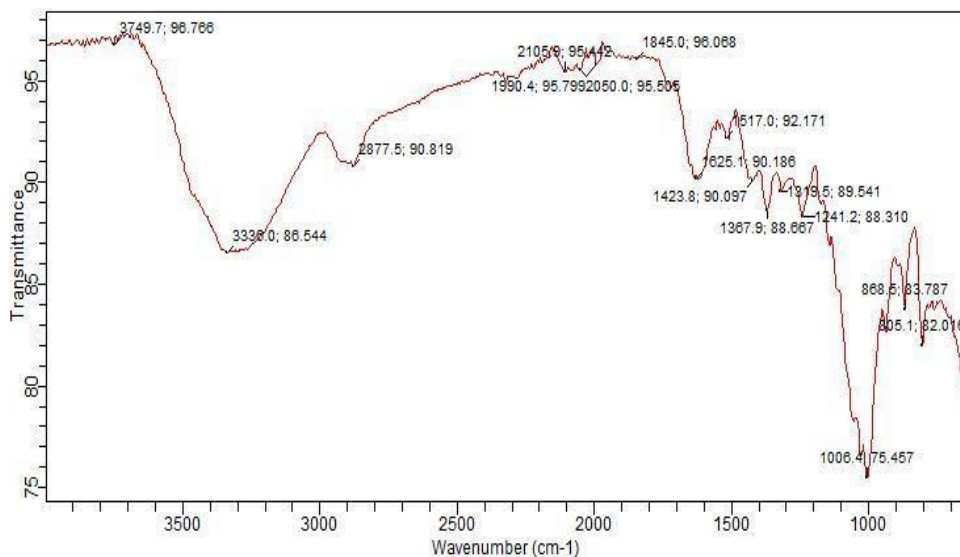


Fig. 4. FTIR Spectra of RTR

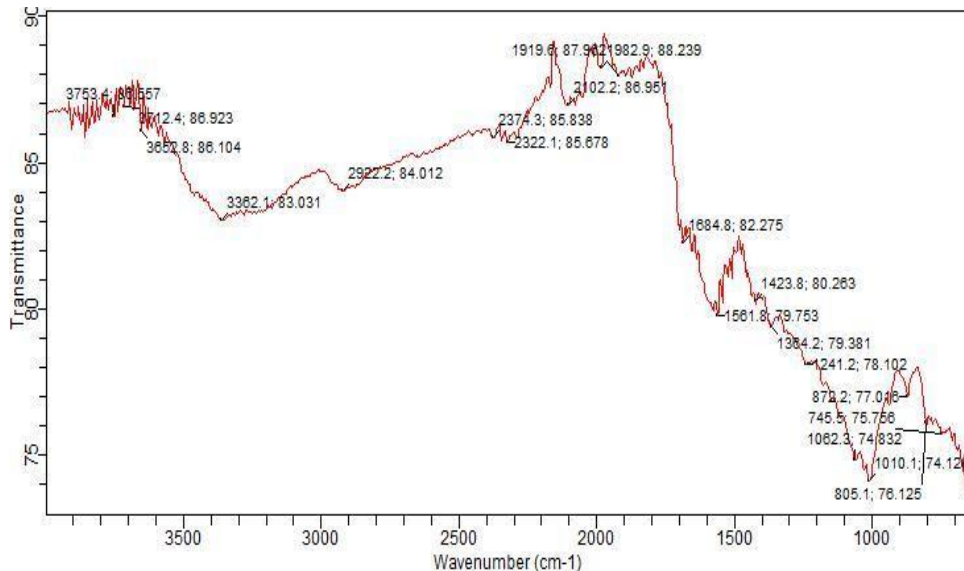


Fig. 5. FTIR Spectra of RTA

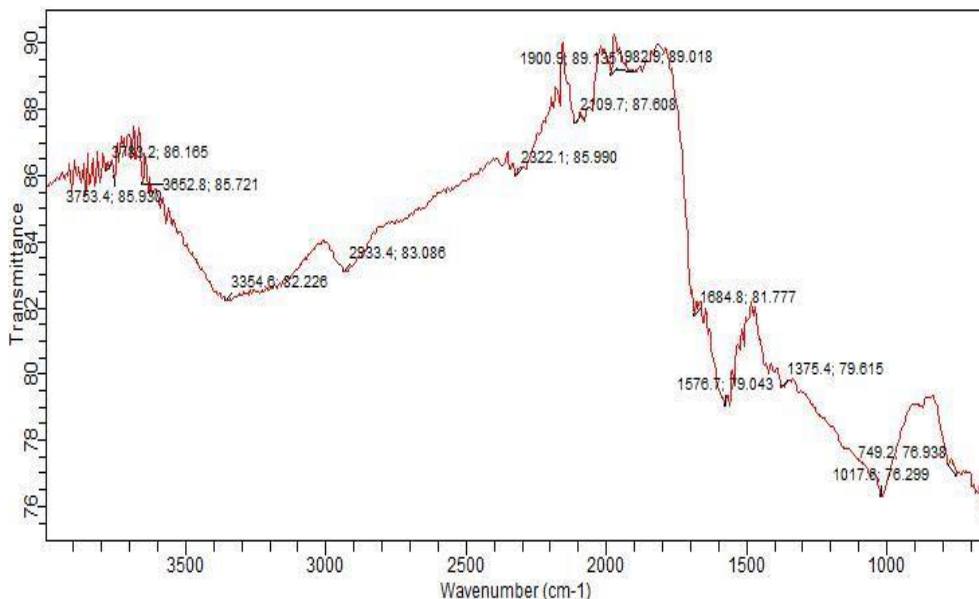


Fig. 6. FTIR Spectra of RTB

3.3. Thermal Behaviour

Thermogravimetric analysis (TGA) reveals the thermal stability of the materials while Differential thermogravimetric analysis (DTA) gives the temperature of the maximum decomposition rate. The TGA and DTA curves of raw *R taedigera*, acid and base biochars are presented as Figure 7, 8 and 9 respectively. According to the results of TGA presented in Figures 7, 8, and 9, there was slight loss of weight in the materials within a temperature range of 50 – 130°C. The loss of weight can be attributed to the removal of weak-bonded water molecules within the materials. The second stage of weight loss which was a major weight loss in the materials was observed at around 350 – 500°C for RTR and at about 350 – 550°C for RTA and RTB. This second stage loss of weight was due to decomposition of glycosyl units of cellulose or lignin followed by the formation of char (Vilar *et al.*, 2009). Also, as shown in the DTA Figures, the peaks corresponding to maximum degradation temperatures of RTR, RTA and RTB were observed at 380°C, 425°C and 410°C respectively. This indicates the activated materials exhibited greater thermal stability. This may be as a result of pyrolysis and the ability of acid and base used as activating agents to further burn out more of organic compounds from the carbonized material.

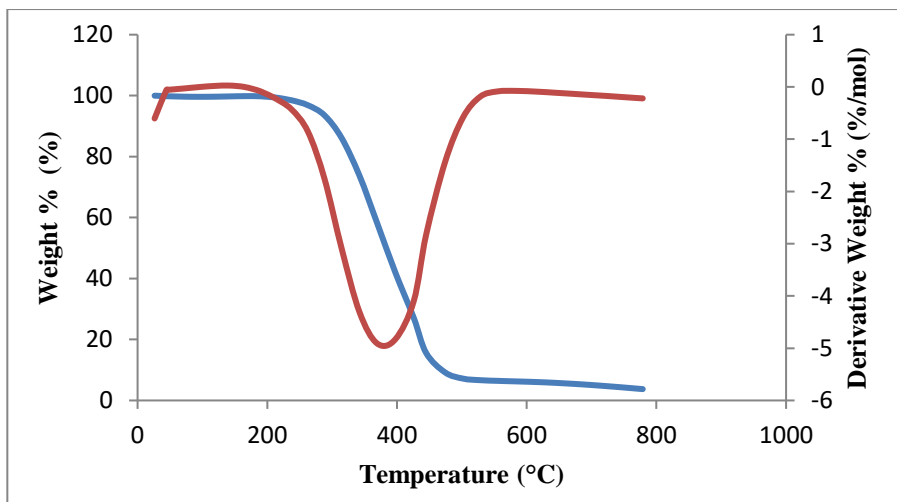


Fig. 7. TGA/DTG curves for RTR

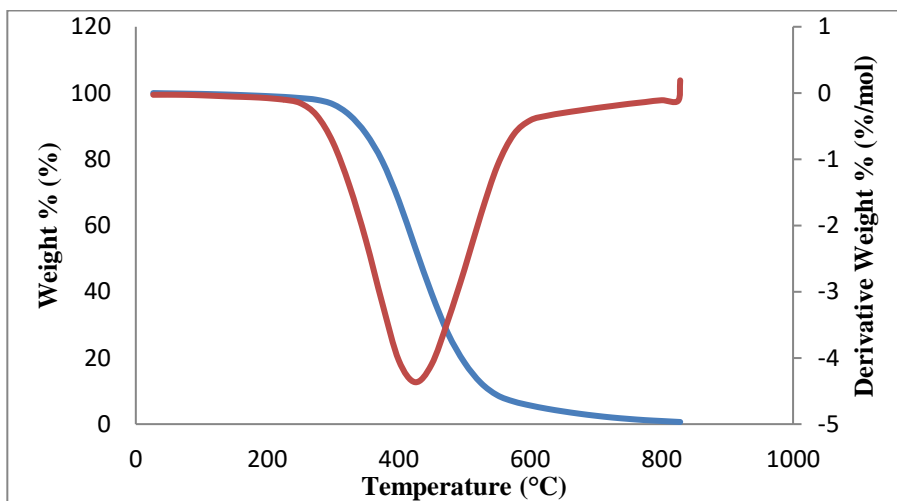


Fig. 8. TGA/DTG curves for RTA

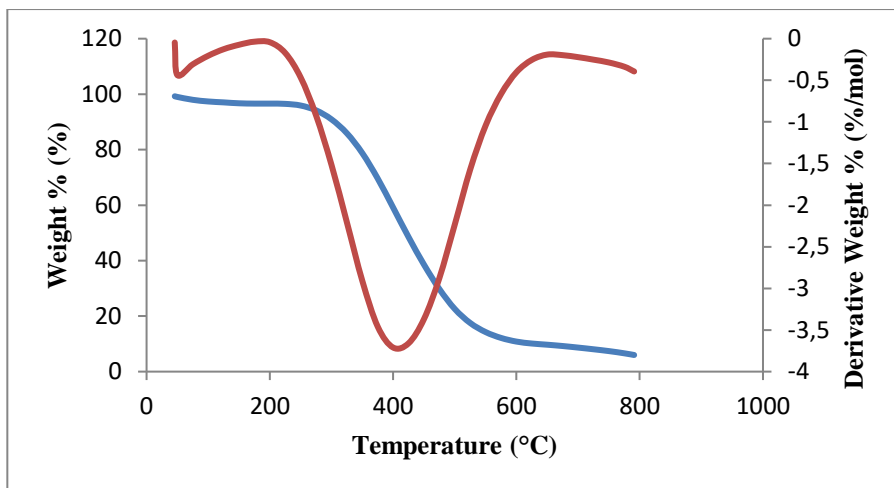


Fig. 9. TGA/DTG curves for RTB

3.4. Results of Parameters Evaluation

3.4.1. Determination of Maximum Absorption Wavelength.

Maximum absorption wavelength of the stock solution was determined using UV-1800 series spectrophotometer between the wavelength 200 and 900 nm. The scanning revealed the maximum absorption wavelength of the methylene blue to be 659 nm as obtained from the curve of absorbance against wavelength as presented as Figure 10. The maximum absorption wavelength was used for subsequent determinations.

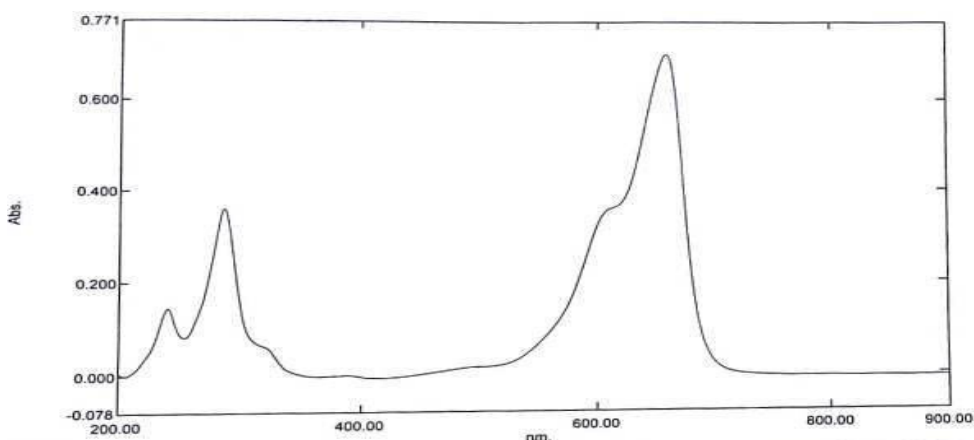


Fig. 10. Absorption Curve of Methylene Blue as a function of Wavelength

3.4.2. Effect of Biochar Dosage

The effect of adsorbent dosage on Methylene blue was determined at room temperature (298 K), adsorbent concentration (100 mg/L) and time (15 minutes). The result, as presented in Figure 11 showed an increase in adsorption as the dosage increases [58, 59, 60] up to 0.7 g. The increase may be due to the availability of a larger active surface area [61] and pore size. Maximum adsorptions of 99.207% and 89.997% were observed at 0.7 g for RTA and RTB respectively. Reduction in the adsorption was observed with a

dosage above 0.7 g for both adsorbents. The reduction can be attributed to the initial vacant sites on the adsorbents being quickly and completely filled with molecules of MB.

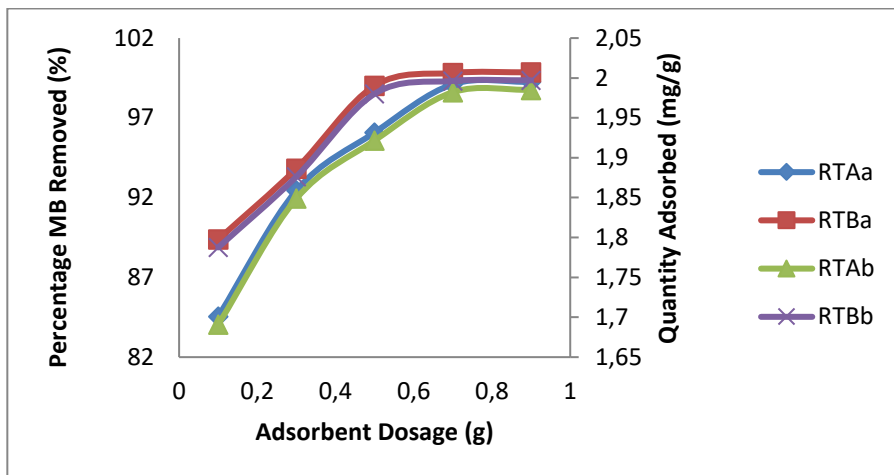


Fig. 11. Effect of dosage on adsorption capacity of RTA and RTB

RTAa and RTBa are percentage of MB removed by RTA and RTB respectively, while RTAb and RTBb are quantity of MB adsorbed per unit mass of RTA and RTB respectively

3.4.3. Effect of Initial Solution Concentration

The effect of initial methylene blue concentration was evaluated with 20.00 mg/L, 40.00 mg/L, 60.00 mg/L, 80.00 mg/L and 100.00 mg/L of methylene blue at constant temperature (298K), time (15 min) and adsorbent dose (0.5 g). Figure 12 revealed that adsorption increases with concentration. This implies that the diffusion of methylene blue is accelerated with increasing concentration due to the increase in forces of attraction of the concentration gradients [62] leading to effective interactions between dye particles and adsorbent surface [63]. On the other hand, the continuous increase of the initial concentration of MB reduces the adsorption capacity of the adsorption; this may be due to the equilibrium between the MB particles and the surface of the adsorbent.

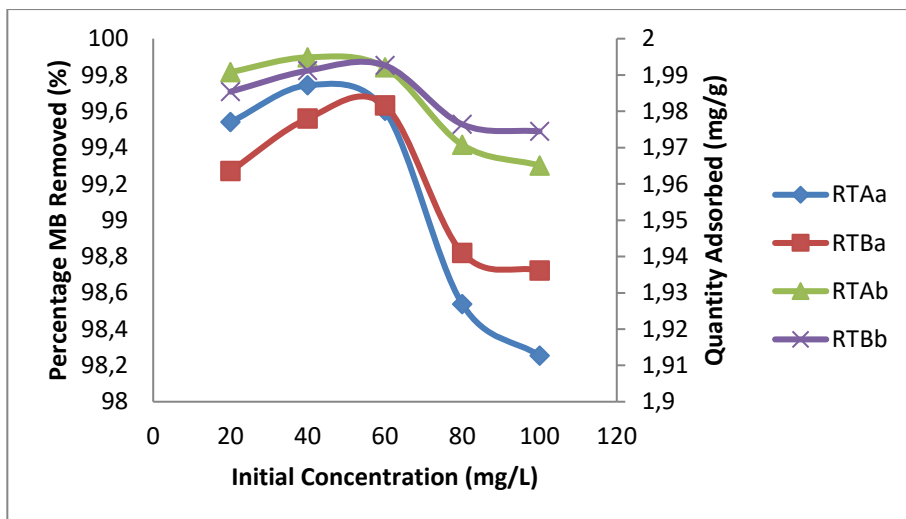


Fig. 12. Effect of initial concentration on adsorption capacity of RTA and RTB

RTAa and RTBa are percentage of MB removed by RTA and RTB respectively, while RTAb and RTBb are quantity of MB adsorbed per unit mass of RTA and RTB respectively

4. Conclusion

In the present study, new potential acidic activated *Raphia taedigera* seed and alkaline activated *Raphia taedigera* seed biochars were prepared from *Raphia taedigera* seed. The biochars were prepared by carbonization and chemical activation using 0.1 M sulphuric acid and 0.1 M sodium hydroxide to produce RTA and RTB respectively. Scanning electron microscopy (SEM), Fourier-transform infrared (FTIR) spectrophotometry, and thermogravimetric/Differential thermal analyses (TG/DTA) were carried out on the prepared biochars and raw *R. taedigera* seed.

- The results of the analyses revealed that acid and base activated materials could be excellent adsorbents for removal of dyes from industrial and agricultural wastewater.
- Considering the results from scanning electron microscope, the activated materials have aggregated and rough surface morphologies with links between surface particles creating porous structure with greater homogeneity.
- Results of thermal analyses, showed higher thermal stability of the biochars with 380°C, 425°C and 418°C maximum decomposition temperatures for RTR, RTA and RTB respectively.
- Fourier-transform infrared spectrophotometry result revealed a large number of peaks corresponding to different functional groups such as hydroxyl group, ketonic group, carboxylic group, alkene group among others, which are all capable of aiding adsorption process.
- The adsorbents performance evaluations using different initial concentrations of methylene blue and adsorbent dosage were evaluated. The results revealed the percentage efficiencies of RTA and RTB to be within 98.245 % to 99.743 % and 98.723 % to 99.632 % respectively for the methylene blue initial concentrations range of 20 to 100 mg/L. Also, 84.542 % to 99.256 % and

89.375 % to 99.851 % efficiencies were observed for RTA and RTB respectively, for the effect of adsorbent dosages range of 0.1 g to 0.9 g.

The results of the preliminary investigations showed great potentials of the materials being used as adsorbents. Further studies are required to investigate the mechanism involved and the efficiencies of the prepared materials.

Acknowledgement

The authors appreciate the efforts of the staff of the department of chemistry, Federal University of Technology, Akure and the department of Science Technology, The Federal Polytechnic, Ado-Ekiti. This research did not receive any grant from funding agencies in the public, commercial, or not-for-profit sectors.

Reference

- [1] Rajendran S, Khan MM, Gracia F, Qin J, Gupta VK, Arumainathan S. Ce³⁺-ion-induced visible-light photocatalytic degradation and electrochemical activity of ZnO/CeO₂ nanocomposite. *Sci. Rep.*, 2016; 5: 31641. <https://doi.org/10.1038/srep31641>
- [2] Vijayakumar G, Tamilarasan R, Dharmendirakumar MM. Adsorption, Kinetic, Equilibrium and Thermodynamic studies on the removal of basic dye Rhodamine-B from aqueous solution by the use of natural adsorbent perlite. *J. Mater. Environ. Sci.*, 2012; 3: 157- 170.
- [3] Wawrzekiewicz M, Hubicki Z. Removal of tartrazine from aqueous solutions by strongly basic polystyrene anion exchange resins. *J. Hazard. Mater.* 2009; 164: 502-509. <https://doi.org/10.1016/j.jhazmat.2008.08.021>
- [4] Poinern GEJ, Senanayake G, Shah N, Thi-Le XN, Parkinson GM, Fawcett B. Adsorption of the aurocyanide, complex on granular activated carbons derived from macadamia nut shells - A preliminary study. *Miner. Eng.*, 2011; 24: 1694-1702 <https://doi.org/10.1016/j.mineng.2011.09.011>
- [5] Kirubakaran CJ, Krishnaiah K, Seshadri SK. Experimental study of the production of activated carbon from coconut shells in a fluidized bed reactor. *Ind. Eng. Chem. Res.*, 1991; 30: 2411-2416. <https://doi.org/10.1021/ie00059a008>
- [6] Arris S, Bencheikh LM, Miniai HA. Preparation and characterisation of an natural adsorbent used for elimination of pollutants in wastewater, *Energy Procedia.* 2012; 18: 1145 - 1151. doi: 10.1016/j.egypro.2012.05.129 <https://doi.org/10.1016/j.egypro.2012.05.129>
- [7] Saravanan R, Sacari E, Gracia F, Khan MM, Mosquera E, GuptaVK. Conducting PANI stimulated ZnO system for visible light photocatalytic degradation of colored dyes. *Mol. Liq. J.*, 2016; 221: 1029-1033 <https://doi.org/10.1016/j.molliq.2016.06.074>
- [8] Gupta VK, Jain R, MittalA, Tawfik A, Saleh A, Naya A, Agarwal S, Sikarwa S. Photocatalytic degradation of toxic dye amaranth on TiO₂/UV in aqueous suspensions. *Mater. Sci. Eng. C*, 2012; 32: 12-17
- [9] Gupta VK, Jain R, Nayak A, Agarwal S, Shrivastava M. Removal of the hazardous dye Tartrazine by photodegradation on titanium dioxide surface. *J. Hazard. Mater.*, 2011; 31: 1062-1067 <https://doi.org/10.1016/j.msec.2011.03.006>
- [10] Saleh TA, Gupta VK. Photo-catalyzed degradation of hazardous dye methyl orange by use of a composite catalyst consisting of multi walled carbon nanotubes and titanium dioxide. *J. Colloid Interface Sci.*, 2012; 371: 101-106 <https://doi.org/10.1016/j.jcis.2011.12.038>

- [11] Saravanan R, Gracia F, Khan MM, Poornima V, Gupta VK, Narayanan A. ZnO/CdO nanocomposites for textile effluent degradation and electrochemical detection. *J. Mol. Liq.*, 2015; 209: 374-380. <https://doi.org/10.1016/j.molliq.2015.05.040>
- [12] Saravanan R, Gupta VK, Mosquera E, Gracia F. Preparation and characterization of V2O5/ZnO nanocomposite system for photocatalytic application. *J. Mol. Liq.*, 2014; 198: 409-412 <https://doi.org/10.1016/j.molliq.2014.07.030>
- [13] Behnajady MA, Modirshahla N, Ghanbary F. A kinetic model for the decolorization of C. I. Acid yellow 23 by Fenton process. *J. Hazard. Matter.*, 2007; 148: 98-102 <https://doi.org/10.1016/j.jhazmat.2007.02.003>
- [14] Garcia-Montano J, Ruiz N, Munoz I, Domenech X, Garcia-Hortal JA, Torrades F, Pearl J. Environmental assessment of different Photo-Fenton approaches for commercial reactive dye removal. *J. Hazard. Mater.*, 2007; 138: 218 - 225 <https://doi.org/10.1016/j.jhazmat.2006.05.061>
- [15] Abbasi M, Asi NR. Sonochemical degradation of Basic Blue 41 dye assisted by nano TiO₂ and H₂O₂. *J. Hazard. Mater.*, 2008; 153: 942 - 947 <https://doi.org/10.1016/j.jhazmat.2007.09.045>
- [16] Saleh TA, Gupta VK. Column with CNT/magnesium oxide composite for lead(II) removal from water. *Envir. Sci. Poll. Res.*, 2012; 19: 1224-1228 <https://doi.org/10.1007/s11356-011-0670-6>
- [17] Lorenc-Grabowski E, Gryglewicz G. Adsorption characteristics of Congo red on coal-based mesoporous activated carbon. *Dyes Pigm.*, 2007; 74: 34-40. <https://doi.org/10.1016/j.dyepig.2006.01.027>
- [18] Malik PK, Sanyal SK. Kinetics of decolorization of azo dyes in wastewater by UV/H₂O₂ process. *Sep. Purif. Technol.*, 2004; 36: 167-170 [https://doi.org/10.1016/S1383-5866\(03\)00212-0](https://doi.org/10.1016/S1383-5866(03)00212-0)
- [19] Banat IM, Nigam P, Singh R. Marchant, Microbial decolorization of textile dye containing effluents: a review. *Bioresour. Technol.*, 1996; 58: 217-227. [https://doi.org/10.1016/S0960-8524\(96\)00113-7](https://doi.org/10.1016/S0960-8524(96)00113-7)
- [20] Malik PK, Saha SK. Oxidation of direct dyes with hydrogen peroxide using ferrous ion as catalyst. *Sep. Purif. Technol.*, 2003; 31: 241-250. [https://doi.org/10.1016/S1383-5866\(02\)00200-9](https://doi.org/10.1016/S1383-5866(02)00200-9)
- [21] Asfaram A, Ghaedia M, Hajati S, Goudarzi A, Alipanahpour Dil E. Screening and optimization of highly effective ultrasound-assisted simultaneous adsorption of cationic dyes onto Mn-doped Fe₃O₄-nanoparticle-loaded activated carbon Ultrason. Sonochem., 2017; 34: 1-12 <https://doi.org/10.1016/j.ultsonch.2016.05.011>
- [22] Alipanahpour Dil E, Ghaedi M, Asfaram A, Hajati S, Mehrabi F, Goudarzi A. Preparation of nanomaterials for the ultrasound-enhanced removal of Pb²⁺ ions and malachite green dye: chemometric optimization and modelling Ultrason. Sonochem., 2017; 34: 677-691 <https://doi.org/10.1016/j.ultsonch.2016.07.001>
- [23] Ghaedi M, Zare Khafri H, Asfaram A, Goudarzi A. Response surface methodology approach for optimization of adsorption of Janus Green B from aqueous solution onto ZnO/Zn(OH)₂-NP-AC: kinetic and isotherm study. *Spectrochim. Acta. A*, 2015; 152: 233-240 <https://doi.org/10.1016/j.saa.2015.06.128>
- [24] Mazaheri H, Ghaedi M, Asfaram A, Hajati S. Performance of CuS nanoparticle loaded on activated carbon in the adsorption of methylene blue and bromophenol blue dyes in binary aqueous solutions: using ultrasound power and optimization by central composite design. *J. Mol. Liq.*, 2016; 219: 667-676 <https://doi.org/10.1016/j.molliq.2016.03.050>
- [25] Mittal A, Mittal J, Malviya A, Kaur D, Gupta VK. Decoloration treatment of a hazardous triarylmethane dye, light green SF (Yellowish) by waste material

- adsorbents. *J. Colloid Interface Sci.*, 2010; 342: 518-527
<https://doi.org/10.1016/j.jcis.2009.10.046>
- [26] Gupta VK, Nayak A. Cadmium removal and recovery from aqueous solutions by novel adsorbents prepared from orange peel and Fe₂O₃ nanoparticles. *Chem. Eng. J.*, 2012; 180: 81-90 <https://doi.org/10.1016/j.cej.2011.11.006>
- [27] Gupta VK, Nayak A, Agarwal S. Bioadsorbents for remediation of heavy metals: current status and their future prospects. *Environ. Eng. Res.*, 2015; 20: 1-18
<https://doi.org/10.4491/eer.2015.018>
- [28] Gupta VK, Nayak A, Bhushan B, Agarwal S. A critical analysis on the efficiency of activated carbons from low-cost precursors for heavy metals remediation. *Crit. Rev. Environ. Sci. Technol.*, 2015; 45: 613-668
<https://doi.org/10.1080/10643389.2013.876526>
- [29] Saleh TA, Gupta VK. Processing methods, characteristics and adsorption behavior of tires derived carbons: a review. *Adv. Colloid Interface Sci.*, 2014; 211: 92-100
<https://doi.org/10.1016/j.cis.2014.06.006>
- [30] Alok M, Jyoti M, Arti M, Gupta VK. Removal and recovery of Chrysoidine Y from aqueous solutions by waste materials, *Journal of Colloid and Interface Science*, 2010; 344: 497-507. <https://doi.org/10.1016/j.jcis.2010.01.007>
<https://doi.org/10.1016/j.jcis.2010.01.007>
- [31] Deng H, Yang L, Tao G, Dai J. Preparation and characterization of activated carbon from cotton stalk by microwave assisted chemical activation-application in methylene blue adsorption from aqueous solution., *Journal of Hazardous Materials* 2009; 166: 1514-1521. <https://doi.org/10.1016/j.jhazmat.2008.12.080>
- [32] Liu QS, Zheng T, Wang P, Guo L. Preparation and characterization of activated carbon from bamboo by microwave-induced phosphoric acid activation. *Industrial Crops and Products*, 2010; 31: 233 - 238.
<https://doi.org/10.1016/j.indcrop.2009.10.011>
- [33] Saka C. BET, TG-DTG, FT-IR, SEM, iodine number analysis and preparation of activated carbon from acorn shell by chemical activation with ZnCl₂. *Journal of Analytical and Applied Pyrolysis*, 2012; 95: 21-24.
<https://doi.org/10.1016/j.jaap.2011.12.020>
- [34] Kamaraj M, Umamaheswari J. Preparation and characterization of Groundnut shell activated carbon as an efficient adsorbent for the removal of Methylene blue dye from aqueous solution with microbiostatic activity. *Journal of Materials and Environmental Sciences*, 2017; 8: 2019-2025
- [35] Malik R, Ramteke D, Wate S. Adsorption of malachite green on groundnut shell waste based powdered activated carbon. *Waste Management*, 2007; 27: 1129-1138.
<https://doi.org/10.1016/j.wasman.2006.06.009>
- [36] Tsai W, Chang C, Lin M, Chien S, Sun H, Hsieh M. Adsorption of acid dye onto activated carbons prepared from agricultural waste bagasse by ZnCl₂ activation. *Chemosphere* 2001; 45: 51-58. [https://doi.org/10.1016/S0045-6535\(01\)00016-9](https://doi.org/10.1016/S0045-6535(01)00016-9)
- [37] AbdulRahman A, Latiff1 AAA, Daud Z, Ridzuan MB, N F M D, Jagaba AH. Preparation and Characterization of Activated Cow Bone Powder for the Adsorption of Cadmium from Palm Oil Mill Effluent. *IOP Conf. Series: Materials Science and Engineering*, 2016; 136: 012045 doi:10.1088/1757-899X/136/1/012045
<https://doi.org/10.1088/1757-899X/136/1/012045>
- [38] Lua AC, Guo J. Preparation and characterization of activated carbons from oil-palm stones for gas-phase adsorption. *Colloids and Surfaces A: Physicochemical and Engineering Aspects*, 2001; 179: 151-162. [https://doi.org/10.1016/S0927-7757\(00\)00651-8](https://doi.org/10.1016/S0927-7757(00)00651-8)

- [39] Li W, Yang K, Peng J, Zhang L, Guo S, Xia H. Effects of carbonization temperatures on characteristics of porosity in coconut shell chars and activated carbons derived from carbonized coconut shell chars. *Industrial Crops and Products*, 2008; 28: 190-198. <https://doi.org/10.1016/j.indcrop.2008.02.012>
- [40] Kilic M, Apaydin-Varol E, Pütün AE. Adsorptive removal of phenol from aqueous solutions on activated carbon prepared from tobacco residues: Equilibrium, kinetics and thermodynamics. *Journal of Hazardous Materials*, 2011; 189: 397-403. <https://doi.org/10.1016/j.jhazmat.2011.02.051>
- [41] Martinez M, Torres M, Guzman C, Maestri D. Preparation and characteristics of activated carbon from olive stones and walnut shells. *Industrial Crops and Products*, 2006; 23: 23-28. <https://doi.org/10.1016/j.indcrop.2005.03.001>
- [42] Sentorun-Shalaby C, Ucak-Astarhuglu MG, Artok L, Sarica C. Preparation and characterization of activated carbons by one-step steam pyrolysis/activation from apricot stones. *Microporous and Mesoporous Materials*, 2006; 88: 126-134 <https://doi.org/10.1016/j.micromeso.2005.09.003>
- [43] Hayashi J, Horikawa T, Takeda I, Muroyama K, Nasir Ani F. Preparing activated carbon from various nutshells by chemical activation with K₂CO₃. *Carbon*, 2002; 40: 2381-2386. [https://doi.org/10.1016/S0008-6223\(02\)00118-5](https://doi.org/10.1016/S0008-6223(02)00118-5)
- [44] Momcilovic M, Purenovic M, Bojic A, Zarubica A, Randelovic M. Removal of lead (II) ions from aqueous solutions by adsorption onto pine cone activated carbon. *Desalination*, 2011; 276: 53-59. <https://doi.org/10.1016/j.desal.2011.03.013>
- [45] Angin D. Production and characterization of activated carbon from sour cherry stones by zinc chloride. *Fuel*, 2014; 115: 804-811. <https://doi.org/10.1016/j.fuel.2013.04.060>
- [46] Bailey LJ. *Certain palms of Panama*. Gentes Herbarium, 1935; 3: 33-116.
- [47] Allen PH. *Rain forest palms of Golfo Dulce*. Principle, 1965a; 9: 48-66.
- [48] Henderson A. *Palms of the Amazon*. Oxford University Press, Oxford, England, 1996.
- [49] Abegunde SM. Proximate Composition, Phytochemical Analysis and Elemental Characterization of *Raphia taedigera* Seed. *Asian Journal of Chemical Sciences*, 2018; 5: 1 - 8. <https://doi.org/10.9734/AJOCS/2018/45819>
- [50] Dransfield J, Uhl NW, Asmussen-Lange CB, Baker WJ, Harley MM, Lewis CE. *Genera Palmarum - Evolution and Classification of the Palms*. Royal Botanic Gardens, Kew, 2008.
- [51] Li J, Wang X, Zhao G, Chen C, Chai Z, Alsaedi A. Metal-organic framework-based materials: superior adsorbents for the capture of toxic and radioactive metal ions. *Chemical Society Review*, 2018; 27: 2322 - 2356. [10.1039/C7CS00543A](https://doi.org/10.1039/C7CS00543A) <https://doi.org/10.1039/C7CS00543A>
- [52] Anderson R, Mori S. A preliminary investigation of *Raphia* palm swamps. *Puerto Viejo, Costa Rica*. Turrialba, 1967; 17: 221-224.
- [53] Bello OS, Adegoke KA, Akinyunni OO. Preparation and characterization of a novel adsorbent from *Moringa oleifera* leaf. *Appl Water Sci.*, 2017; 7: 1295-1305 DOI [10.1007/s13201-015-0345-4](https://doi.org/10.1007/s13201-015-0345-4) <https://doi.org/10.1007/s13201-015-0345-4>
- [54] Al-Ghouti MA, Khraishe M, Allen SJ, Ahmad MN. The removal of dyes from textile wastewater: a study of the physical characteristics and adsorption mechanisms of diatomaceous earth. *J Environ Manag.*, 2013; 69: 229. <https://doi.org/10.1016/j.jenvman.2003.09.005>
- [55] Bekci Z, Seki Y, Cavas L. Removal of malachite green by using an invasive marine alga *Caulerpa racemosa* var. *Cylindracea*. *J Hazard Mater*, 2009; 161: 1454-1460. <https://doi.org/10.1016/j.jhazmat.2008.04.125>

- [56] Arabi M, Ghaedi M, Ostovan A. Development of a Lower Toxic Approach Based on Green Synthesis of Water-Compatible Molecularly Imprinted Nanoparticles for the Extraction of Hydrochlorothiazide from Human Urine. *ACS Sustainable Chemistry & Engineering* 2017; 5: 3775-3785. doi:10.1021/acssuschemeng.6b02615 <https://doi.org/10.1021/acssuschemeng.6b02615>
- [57] Sekhar CP, Kalidhasan S, Rajesh V, Rajesh N. Biopolymer adsorbent for the removal of malachite green from aqueous solution. *Chemosphere*, 2009; 77: 842-847 <https://doi.org/10.1016/j.chemosphere.2009.07.068>
- [58] Kumar KK, Prasad MK, Baburao G, Sudhakar M, Sivajyothi J, Sathish T, Murthy VR. A fortunate marine algae biomass, *Sargassum cinereum* for removal of Pb(II): Studies on thermodynamics, kinetics and characterization. *Desalination and Water Treatment*, 2018; 116: 179-186 doi: 10.5004/dwt.2018.22544 <https://doi.org/10.5004/dwt.2018.22544>
- [59] Sogbochi E, Balogoun CK, Dossa CPA, Sohounhloue DCK. Evaluation of Adsorption Capacity of Methylene Blue in Aqueous Medium by Two Adsorbents: The Raw Hull of *Lophira lanceolata* and Its Activated Carbon. *American Journal of Physical Chemistry*, 2017; 6: 76 - 87.. <https://doi.org/10.11648/j.ajpc.20170605.11>
- [60] HAMEED AM, Bassim H. Adsorption of methyl violet dye on acid modified activated carbon: isotherms and thermodynamics. *Journal of Applied Sciences in Environmental Sanitation*, 2010; 5: 161-170.
- [61] Saleh TA, Gupta VK. Photo-catalyzed degradation of hazardous dye methyl orange by use of a composite catalyst consisting of multi-walled carbon nanotubes and titanium dioxide. *Journal of Colloid and Interface Science*, 2012; 371: 101-106. doi.org/10.1016/j.jcis.2011.12.038 <https://doi.org/10.1016/j.jcis.2011.12.038>
- [62] Mahmut O. Phosphate adsorption characteristics of alunite to be used as a cement additive. *Cement and Concrete Research*, 2003; 33: 1583-1587. [https://doi.org/10.1016/S0008-8846\(03\)00113-3](https://doi.org/10.1016/S0008-8846(03)00113-3)
- [63] Robati D, Mirza B, Rajabi M, Moradi O, Tyagi I, Agarwal S, Gupta VK. Removal of hazardous dyes-BR 12 and methyl orange using graphene oxide as an adsorbent from aqueous phase. *Chemical Engineering Journal*, 2016; 284: 687-697 doi.org/10.1016/j.cej.2015.08.131 <https://doi.org/10.1016/j.cej.2015.08.131>



Research Article

Fabrication and in-vitro evaluation of copper doped bioactive glass/polymer composite scaffolds for bone tissue engineering

Ahsen Ünal*^{1,a}, Işıl Özer^{1,b}, Melek Erol Taygun^{1,c}, Sadriye Küçükbayrak^{1,d}

Department of Chemical Engineering, Chemical and Metallurgical Engineering Faculty, Istanbul Technical University, Turkey

Article Info

Article history:

Received 31 Jan 2019

Revised 3 June 2019

Accepted 4 June 2019

Keywords:

Composite;

Scaffold;

Bioactive glass;

Therapeutic ion;

Bone tissue engineering

Abstract

Composites developed by combining bioactive glasses and biopolymers are attractive materials for use in bone tissue engineering scaffolds due to their bioactivity, biocompatibility, osteoconductivity and mechanical properties. From this point of view, in this study, three-dimensional polymer/bioactive composite scaffolds were fabricated by using polymer foam replication method. To be able to achieve this goal, in the first stage new bioactive glass composition in the system $\text{SiO}_2\text{-CaO-Na}_2\text{O-P}_2\text{O}_5$ were developed with the incorporation of copper which have antibacterial and angiogenic properties. Scaffolds that mimic the structure of the foams were obtained after the heat treatment process. Then, the scaffolds were coated with gelatine at different percentages (1 and 3 weight%) in order to improve mechanical properties of the scaffolds. Microstructural, physical, chemical and mechanical properties of the composite scaffolds were investigated by using scanning electron microscopy (SEM), energy-dispersive X-ray spectroscopy (EDS), Fourier-transform infrared spectroscopy (FTIR), X-ray diffraction analysis (XRD), compressive strength test and porosity measurements. Furthermore, bioactivity and biodegradability behavior of the samples were determined by in vitro simulated body fluid (SBF) studies. The results showed that all scaffolds favored precipitation of calcium phosphate layer when they were soaked in SBF; they can also deliver controlled doses of copper toward the SBF medium. It was concluded that scaffolds coated with gelatine may be promising candidates for bone tissue engineering applications due to their porosity, bioactivity and appropriate biodegradation rate.

© 2019 MIM Research Group. All rights reserved.

1. Introduction

Tissue engineering is an alternative approach to traditional methods for regeneration, repair and replacement of tissues and organs damaged as a result of trauma, infections or aging with the aid of scaffolds which have the ability to mimic the structure and function of the native tissues. Scaffolds that optimize cell integration with surrounding environment, cell migration and nutrient diffusion between the cells distributed within the matrix and the surroundings, provide a temporary framework for cells in order to constitute their own extracellular matrix (ECM) and degrade with the concurrent new tissue formation [1-7].

By virtue of innovation in bone tissue engineering, design of a novel scaffold with well-defined architecture is essential to fulfil the requirements in this field. The suitable scaffold

*Corresponding author: unal@itu.edu.tr

^a orcid.org/0000-0003-1268-6380; ^b orcid.org/0000-0002-3755-1389; ^c orcid.org/0000-0002-5938-3101;

^d orcid.org/0000-0002-2297-4629

DOI: <http://dx.doi.org/10.17515/resm2019.107ma0131>

Res. Eng. Struct. Mat. Vol. 6 Iss. 2 (2020) 183-195

should (i) be bioactive, biocompatible and biodegradable which encourages cell proliferation; (ii) has a highly porous three-dimensional (3-D) architecture with an interconnected pore network; (iii) has sufficient mechanical properties comparable to the host tissues permitting cell mechanoregulation to occur and structural integrity to remain [7-9]. Pore size and overall porosity are thought critical factors influencing bone tissue growth and nutrient transportation. However, mechanical strength is inversely related to increasing porosity of the scaffold. Therefore, the design of a suitable scaffold with optimum porosity and mechanical strength is a challenging issue [9-10].

Porous 3-D scaffolds were developed through utilizing a variety of materials including metals, polymers, ceramics and composites. Natural bone framework is a composite composed of organic components (25%) consisting mainly of collagen I and inorganic components (65%) consisting mainly of hydroxyapatite. The composite scaffolds as hybrid organic/inorganic biomaterials have hold great promise to mimic the natural bone composition [2].

Bioactive glasses comprise of a silicate network integrating sodium, calcium and phosphorus in various relative amounts are of great interest in biomedical applications due to their high bioactivity. However, low mechanical properties of bioactive glasses restrict their use in load-bearing applications. Bioactive glass/biopolymer composite materials that manipulate the flexibility of polymers with the stiffness and bioactive property of the bioactive glasses have enhanced mechanical properties, chemical stability or biological reactivity [11]. Common methods for fabrication of bioactive glasses include traditional melt quenching method and sol-gel method [12,13]. The foam replication method used in scaffold fabrication draws attention because of its ability to controlling pore size and distribution, not using toxic chemicals and simply adjusting the structure of the foam template [14].

The composition of porous bioactive glasses widely accepted in the systems of $\text{SiO}_2\text{-CaO}$ or $\text{SiO}_2\text{-CaO-P}_2\text{O}_5$, has been improved with controlled amounts of therapeutic ions such as Cu^{2+} , Co^{2+} , Sr^{2+} and Ag^+ due to their antibacterial activity, osteogenic and angiogenic properties. Wu et. al. [15] explained the facility of released copper ions to induce osteogenic and angiogenic response and promote bone regeneration. In this study, Cu-doped bioactive glass/polymer composite scaffolds were fabricated by using polymer replication method.

2. Materials and Methods

2.1. Preparation of Bioactive Glass

Bioactive glasses in the system of $\text{SiO}_2\text{-Na}_2\text{O-P}_2\text{O}_5\text{-CaO-CuO}$ containing 0.5% copper oxide by weight were produced by conventional melt-quenching technique. The nominal composition of this glass is, in weight% 45 SiO_2 , 24.5 Na_2O , 6 P_2O_5 , 24 CaO and 0.5 CuO . For this purpose, appropriate amounts of silicon dioxide (SiO_2 , Sigma-Aldrich), di-sodium hydrogen phosphate (Na_2HPO_4 , Merck), calcium carbonate (CaCO_3 , Merck), copper (II) nitrate ($\text{Cu}(\text{NO}_3)_2$, Sigma-Aldrich) and sodium carbonate (Na_2CO_3 , Merck) were first placed in a platinum crucible. The mixture was melted at 1623 K for 1 h and then quenched into deionized water. As-prepared glasses were ground and kept at 1623 K for 2 h in order to reduce the viscosity of the glass. The obtained bioactive glasses were ground ($\leq 45\mu\text{m}$) for obtaining homogeneous structure.

2.2. Scaffold Fabrication

Scaffolds were prepared by using a polymer foam replication technique. Firstly, the appropriate amount of polyvinyl alcohol (PVA) was dissolved in deionized water for 1 h at 343 K. Once the homogeneous solution was obtained, the temperature was reduced to 313

K and glass powder was dispersed in the solution under constant stirring. The composition of as-prepared solution is 6.28% PVA, 52.37% water and 41.35% glass powders. Polyurethane foams (60 PPI, pore per inch-152 pores/cm) which were cut into 10 x 10 x 10 mm samples, were immersed in the prepared solution for 2 min in order that the foams were coated with bioactive glass particles. Afterwards, as-coated foams were dried at room temperature overnight and subjected to a controlled heat treatment process for 1.5 h at 1223 K and for 2 h at 823 K to remove the polymer and sinter the glass. The scaffolds were then, immersed in the 1wt% and 3 wt% gelatine (50% Type A and 50% Type B) solutions for 2 min. The coated scaffolds with gelatine were left to dry at room temperature overnight.

2.3. Structural Analysis

FTIR spectra were collected using a Perkin-Elmer, Spectrum 100 Model spectrometer in transmittance mode in the mid infrared region ($650\text{-}4000\text{ cm}^{-1}$) for determination of chemical structure of scaffolds before and after immersion in simulated body fluid (SBF). X-ray diffraction (XRD) patterns of coated and uncoated scaffolds were recorded using PANalytical X'Pert Pro diffractometer to determine the characteristic phases and amorphous structure of the scaffolds. Samples were ground and measured in powder form for XRD and FTIR analysis.

2.4. Surface Morphology

Scanning electron microscopy with energy dispersive spectroscopy (SEM-EDS, JEOL 5410) was utilized for morphological and elemental analysis of coated and uncoated scaffolds. Prior to the SEM measurements, all of the samples were coated with platinum under vacuum for 120 seconds by using sputter coater (SC7620, Quorum Technologies Ltd) in order to reduce electron charging effects.

2.5. Assessment of Bioactivity

Biodegradability of coated and uncoated scaffolds and formation of bone-like apatite on various surfaces were evaluated in vitro through immersion of samples in SBF, as described by Kokubo et al. [16]. Each sample of dimensions $5 \times 5 \times 5\text{ mm}^3$ was immersed in 30 ml of SBF and was stored in an incubator at controlled temperature of $37\text{ }^\circ\text{C}$. Samples were immersed in SBF for different soaking periods: 1, 7, 14, and 28 days. When samples were removed from the SBF solution, they were rinsed with ethanol and water, and dried at $37\text{ }^\circ\text{C}$ for 30 minutes. The samples were then characterized using SEM and XRD.

2.6. Water Uptake and Weight Loss Measurements

Water absorption ($\%W_A$) and weight loss ($\%W_L$) of samples upon immersion in SBF were determined over the 28-day period using equations (1) and (2). The initial weights (W_I) of the scaffolds were recorded before they were immersed in SBF. Afterwards, prepared samples were immersed in 30 ml of SBF and incubated at 310 K for 1, 4, 7, 14, 21 and 28 days separately. Samples removed from SBF were dried at room temperature for 1 h and then weighed (W_W) to measure water absorption ($\%W_A$). Subsequently, samples were left in an incubator at 310 K overnight and weighed (W_D) to measure the weight loss ($\%W_L$). Water absorption ($\%W_A$) and weight loss ($\%W_L$) of the samples were calculated using the Eqs. (1) - (2) respectively.

$$\%W_A = \left[\frac{W_W - W_D}{W_D} \right] \times 100 \quad (1)$$

$$\%W_L = \left[\frac{W_I - W_D}{W_I} \right] \times 100 \quad (2)$$

2.7. Mechanical Properties

The compressive strength of samples (dimensions: $5 \times 5 \times 10 \text{ mm}^3$) was measured using a Shimadzu AGS-J servo-hydraulic testing instrument. The crosshead speed was 1 mm/min. At least five specimens for each sample series were tested. Average values and standard deviations were determined.

2.8. Porosity

Porosities of the coated and uncoated scaffolds were measured by using Quantachrome Poromaster Model porosimeter. Experimentally measured raw data were evaluated through a microcomputer data acquisition system and total pore volume was determined.

2.9. Copper Release Investigations

Release properties of scaffolds were investigated by measuring the changes in the concentration of copper in the SBF solution as a result of the soaking of scaffolds for predefined time steps (1, 4, 7, 14, 21 and 28 days) using inductively coupled plasma optical emission spectrometry (ICP-OES). A Perkin Elmer Model Optima 2100 ICP operated at 13.56 MHz (using Ar and N₂ gases) was used for the measurements.

3. Results and Discussions

3.1. Structural Analysis

FTIR analysis was performed to identify the functional groups in the samples. For this purpose, the absorbance values of coated and uncoated samples recorded at 650-4000 cm^{-1} were examined. Figure 1 shows the transmittance spectra of uncoated and coated scaffolds. The characteristic absorption bands detected in the range 1000-1100 cm^{-1} were attributed to Si-O-Si bending stress and the characteristic absorption peak at 900 cm^{-1} indicated the presence of Si-O-Si asymmetric stretching. FTIR results showed that regular tetrahedron SiO₂ structure is formed in the samples. Furthermore, the appearance of the broad peaks in the range of 2900-3000 cm^{-1} are attributed to unsaturated asymmetric O-H stretching vibration due to -OH group related to moisture of the sample. Furthermore, it was determined that the absorption peak at 1600 cm^{-1} in the spectra of samples coated with 1% and 3% gelatine can be assigned to the N-H bending vibration in the amine groups in gelatine [17,18]. This result showed that the scaffolds were coated with gelatine and gelatine was held on the surface successfully.

3.2. Microstructural Analysis

Figures 2, 3 and 4 show the SEM images and EDS results of uncoated and coated scaffolds respectively. It is observed in Figure 2 that scaffold fabricated by the polymer replication method has a three dimensional, open and interconnected macrostructure similar to that of the used polyurethane foam. Moreover, it is seen that the pore walls are completely formed and the thicknesses are in appropriate size that prevents the decay of the structure. Figure 3 indicates that gelatine has attached onto the scaffold surface homogeneously without blocking the macroporous structure. As seen in Figure 4, the pore structure of the sample coated with 3% gelatine is not completely formed, however gelatine coating covered the sample in a homogeneous manner. In addition, 3% gelatine solution causes some of the pores to become clogged. Furthermore, according to the EDS results, it has been observed that Ca²⁺, Si⁴⁺, P⁵⁺ and Na⁺ ions forming the glass composition were present on the surface of the scaffolds. Since Cu²⁺ ion content in the glassy structure is too low, copper cannot be detected in the samples due to the measurement limit of the EDS instrument.

The porosities of the uncoated and coated (1% and 3% gelatine) scaffolds were measured as 81%, 62% and 55%, respectively. According to SEM analysis results and porosity measurements, it is concluded that scaffolds coated with 3% gelatine are not appropriate

for bone tissue regeneration. On the other hand, samples uncoated and coated with 1% gelatine may be suitable candidates for bone tissue regeneration due to higher porosity values than the assumed minimum porosity requirement of 50% [1]. The pore size distributions of uncoated and coated scaffolds are given in Figure 5.

3.3. Mechanical Behavior

The compressive strengths of the uncoated, 1% and 3% gelatine coated samples were measured as 0.052, 0.062 and 0.61 MPa, respectively. The mechanical strength of the scaffolds increased by coating with gelatine. Gelatine layer increases the mechanical strength by covering some pores and filling the micro cracks.

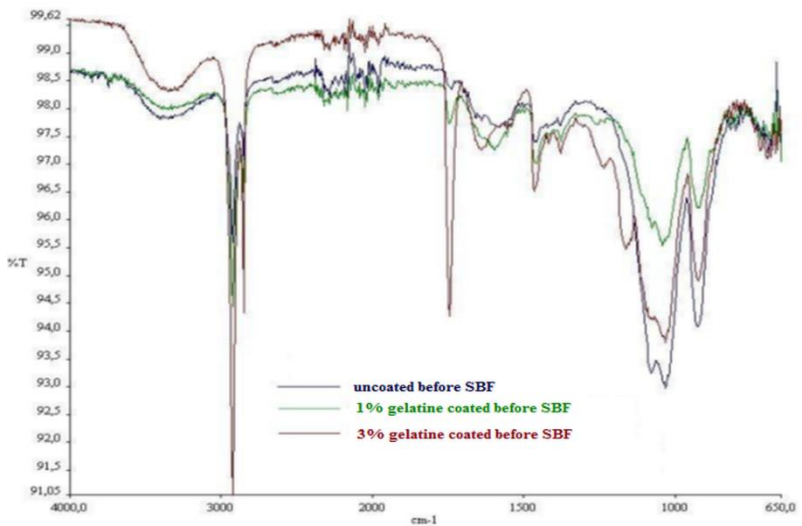


Fig. 1 FTIR spectra of the scaffolds before immersing into SBF

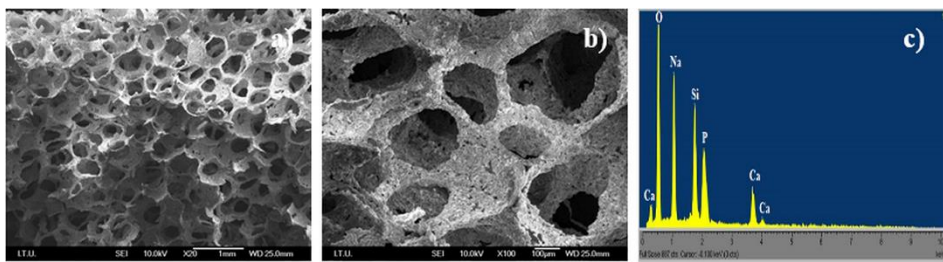


Fig. 2 (a) and (b) SEM images of uncoated scaffold and (c) EDS result of the sample

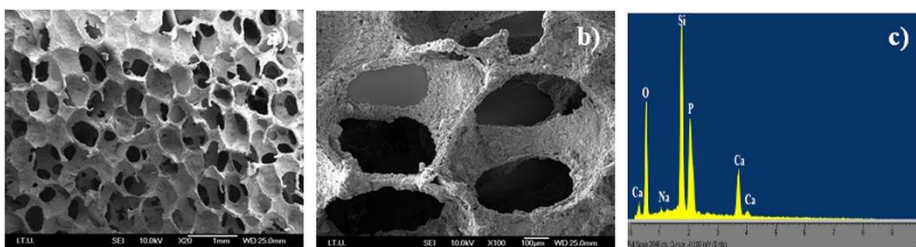


Fig. 3 (a) and (b) SEM images of 1% gelatine coated scaffold and (c) EDS result of the sample

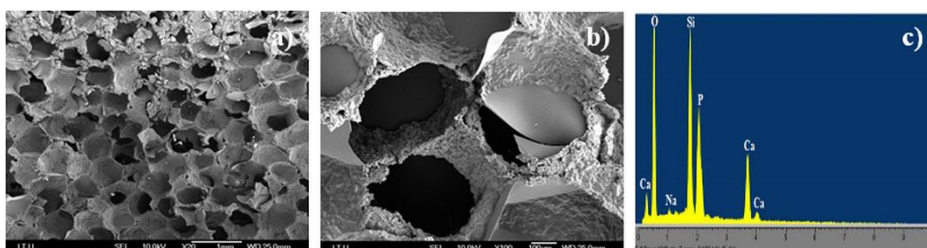


Fig. 4 (a) and (b) SEM images of 3% gelatine coated scaffold and (c) EDS result of the sample

3.4. Bioactivity Assessment

Surface modification of the produced scaffolds after contact with SBF was analyzed using SEM-EDS, XRD and FTIR analysis. Figures 6, 7 and 8 show the SEM images and EDS results of uncoated and coated scaffolds after 28 days immersion in SBF, respectively. It was observed that the hydroxyapatite layer was formed on the surface of the scaffolds from SEM micrographs. As a result of EDS analysis, Ca/P ratio for scaffolds uncoated, coated with 1% and 3% gelatine was determined as 1.53, 1.8 and 1.4, respectively. Ca/P ratio of the scaffold coated with 1% gelatine is closer to HA crystal structure with Ca/P ratio of 1.667. The formation of hydroxyapatite on the surfaces of scaffolds after immersion in SBF was confirmed both SEM and EDS analysis.

As seen in Figures 9, 10 and 11, peaks at 25° , 27° , 32° and 50° 2θ were detected in XRD patterns of uncoated and coated scaffolds immersed in SBF for different time steps. These peaks confirmed the formation of crystalline HA layer on the surface of the scaffolds after one-day contact with SBF. It has been also detected that coating scaffolds with gelatine improved the bioactive behaviour of the scaffolds due to the high bioactivity of the gelatine. According to the XRD results, it is concluded that crystalline HA layer become evident with the increase of soaking time in SBF. Scaffolds coated with 1% gelatine are highly bioactive materials.

FTIR spectra of uncoated and coated scaffolds after immersion in SBF for 28 days is given in Figure 12. P-O bonds, one of the most determinant indicators of formation of the HA layer could not be observed due to the minimum wavelength 650 cm^{-1} of the FTIR used in this study. After 28 days immersion in SBF, observed peaks at 875 cm^{-1} are attributed to carbonate hydroxyapatite (CHA).

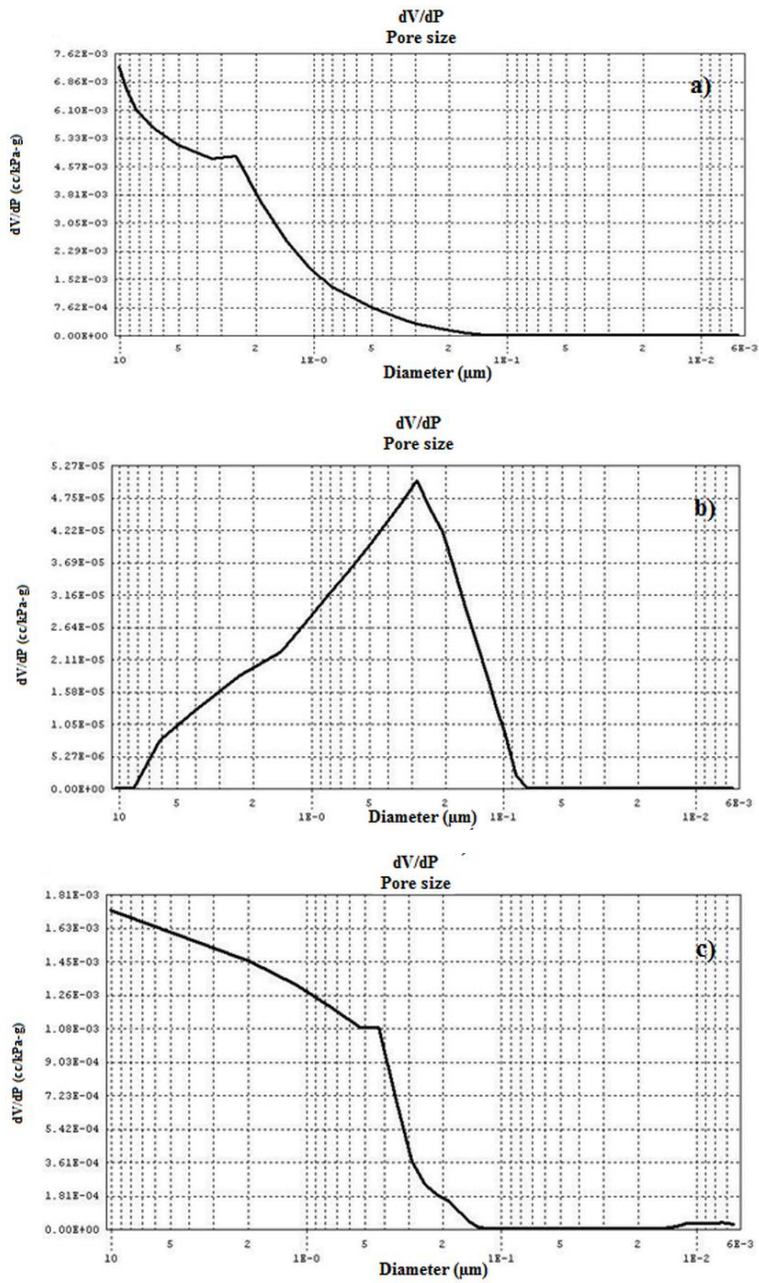


Fig. 5 Pore size distributions of scaffolds uncoated (a), coated with 1% (b) and coated with 3% (c) gelatine

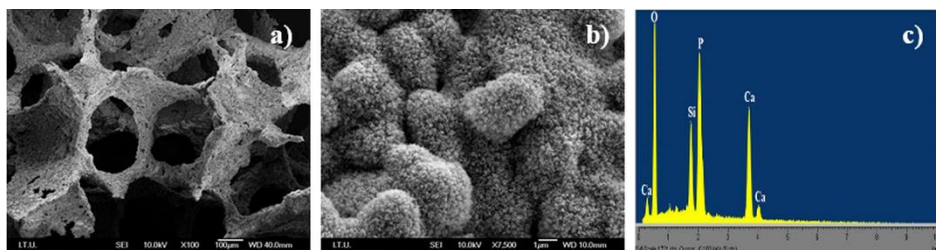


Fig. 6 (a) and (b) SEM images of uncoated scaffold after 28 days immersion in SBF and (c) EDS result of the sample

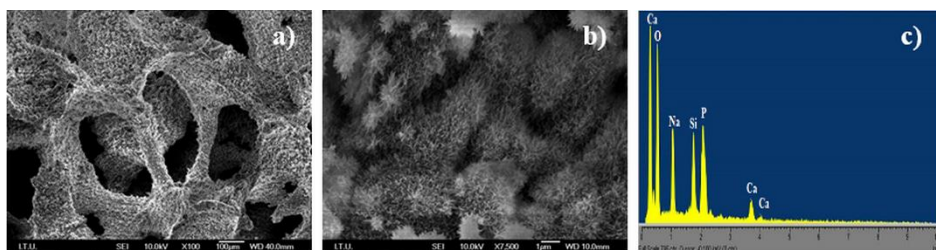


Fig. 7 (a) and (b) SEM images of 1% gelatine coated scaffold after 28 days immersion in SBF and (c) EDS result of the sample

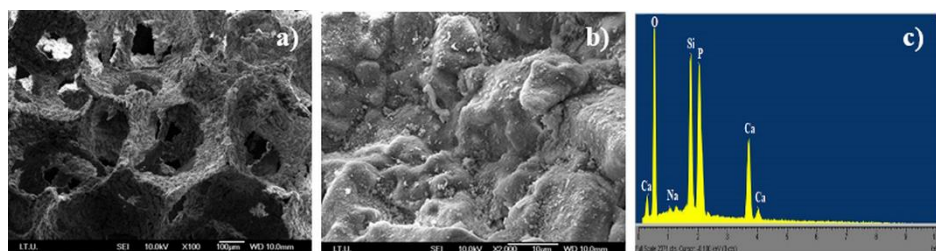


Fig. 8 (a) and (b) SEM images of 3% gelatine coated scaffold after 28 days immersion in SBF and (c) EDS result of the sample

3.5. Biodegradation Behavior

Water absorption and weight loss of scaffolds were investigated in order to determine biodegradability of the samples immersed in SBF for different time periods. According to water absorption analysis results given in Figure 13 (a), compared with the uncoated scaffolds, the rate of water absorption was increased in the coated scaffolds. As seen in the Figure 13 (b), weight loss analysis results showed that the rate of weight loss was increased with gelatine coating ratio. It is concluded that coated scaffolds have higher biodegradation rate.

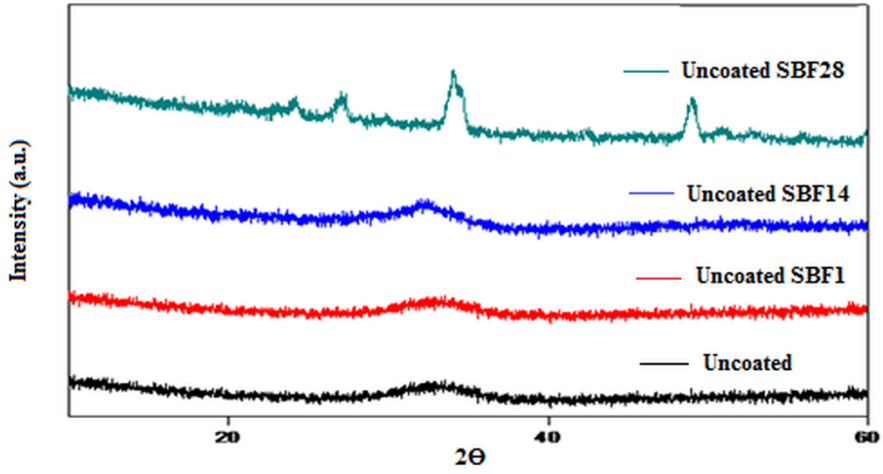


Fig. 9 XRD patterns of uncoated scaffolds before (a) and after (b) 1, (c) 14 and (d) 28 days immersion in SBF

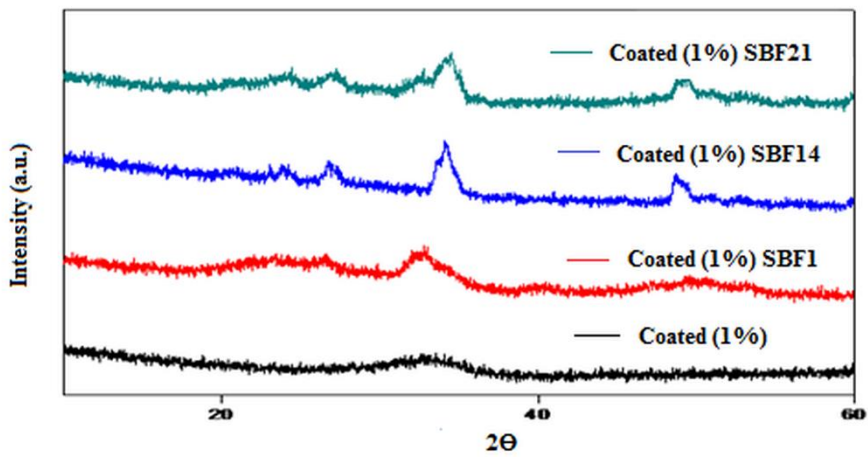


Fig. 10 XRD patterns of 1% gelatine coated scaffolds before (a) and after (b) 1, (c) 14 and (d) 21 days immersion in SBF

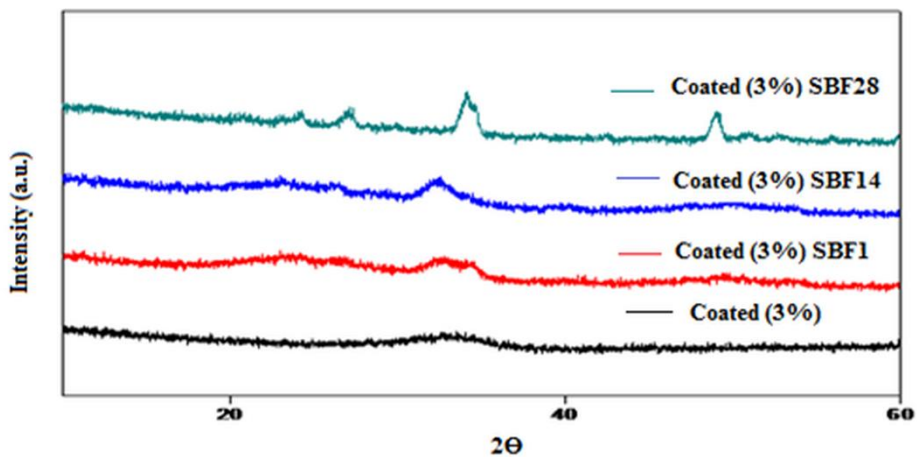


Fig. 11 XRD patterns of 3% gelatine coated scaffolds before (a) and after (b) 1, (c) 14 and (d) 28 days immersion in SBF

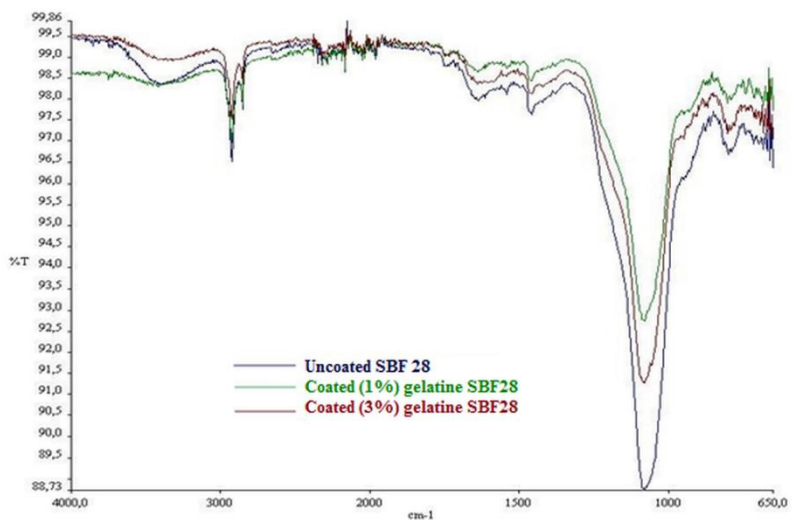


Fig. 12 FTIR spectra of scaffolds (a) uncoated (b) coated with 1% and (c) coated with 3% (c) gelatine after 28 days immersion in SBF

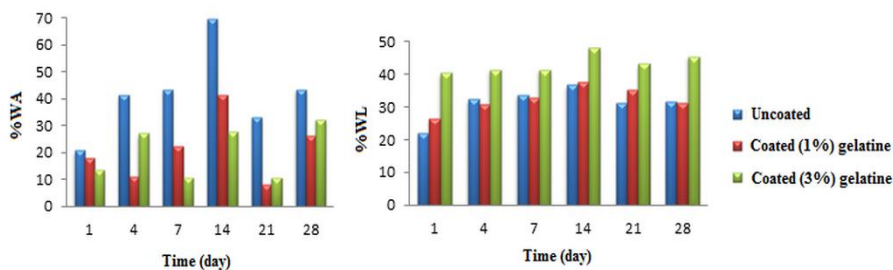


Fig. 13 (a) water absorption and (b) weight loss values for uncoated and coated scaffolds after immersion in SBF for 1, 4, 7, 14, 21 and 28 days

3.6. Copper Release

Copper release behaviour of scaffolds after immersion in SBF for different time periods were evaluated by ICP analysis. In Table 1, cumulative concentration of Cu^{2+} ions released from the uncoated and coated scaffolds into the SBF solution is given. It is clear that copper release from scaffolds increased with immersion time. Furthermore, Cu^{2+} ion release from uncoated scaffolds is higher than that of the release from coated samples because of the rate of glass dissolution process. It is reported that toxic level of copper concentration is accepted as 58 ppm. In addition, cell vascularization and rate of bone formation were increased with copper concentrations higher than 5.6 ppm [19]. From this point of view, it can be said that the obtained scaffolds have angiogenic properties without any toxic effects.

Table 1 Copper ion release from uncoated and coated scaffolds after immersion in SBF

Scaffolds	Copper concentration (ppm)					
	1 day	4 days	7 days	14 days	21 days	28 days
Uncoated	2.356	6.015	7.060	7.650	9.030	11.80
Coated (1%) gelatine	2.352	6.020	6.720	7.620	9.080	10.160
Coated (3%) gelatine	1.826	5.963	6.211	7.470	9.050	10.540

4. Conclusion

In the present study, 0.5% copper doped bioactive glass/gelatine composite scaffolds with interconnected macropores were successfully fabricated by using foam replication method. Porosity measurements and SEM analysis results indicated that produced scaffolds have suitable microstructure for bone tissue engineering requirements. It was found that microporous structure of scaffolds supports bone formation. Pore walls of the scaffolds are completely formed and the thicknesses are in appropriate size that prevents the decay of the structure; however, it was observed that coating with 3% gelatine solution causes some of the pores to become blocked. Uncoated samples and coated samples with 1% gelatine showed higher porosity values than the assumed minimum porosity requirement of bone. As a result of FTIR analysis, observed peaks related to Si-O-Si bonds which are the basic vibration bands of glassy structure and peaks attributed to N-H amine groups indicated that the scaffolds were coated with gelatine and gelatine was held on the surface successfully. According to EDS analysis, Ca/P ratio of the scaffold coated with 1% gelatine is determined as 1.8 which is closer to HA crystal structure with a Ca/P ratio of

1.667. In addition, presence of copper in the glass system promoted the effective bone regeneration. Mechanical strength of the scaffolds were improved by coating scaffolds with gelatine. All analysis proved that the scaffolds immersed in SBF had hydroxyapatite forming ability which is relevant to bone regeneration. The coated scaffolds exhibited improved bioactive behaviour. XRD patterns of uncoated and coated scaffolds immersed in SBF for different time intervals confirmed the formation of crystalline HA layer on the surfaces of the scaffolds. Furthermore, XRD analysis showed that after heating process and coating with gelatine, the amorphous structures of the samples were remained. This is the result of the fact that scaffolds improve the bioactivity properties. According to biodegradability studies, coated scaffolds showed enhanced biodegradability behaviour compared with the uncoated sample. Copper release studies indicated that produced scaffolds can release controlled doses of copper toward the SBF medium that is the determinant for bone tissue regeneration. Within this respect, copper doped bioactive glass/polymer scaffolds offer great perspectives and this results will be subject of further studies.

References

- [1] Fu Q, Saiz E, Rahaman MN, Tomsia AP. Bioactive glass scaffolds for bone tissue engineering: state of the art and future perspectives. *Materials science and engineering: C*. 2011; 31(7):1245-1256. <https://doi.org/10.1016/j.msec.2011.04.022>
- [2] Gaihre B, Jayasuriya A. Comparative investigation of porous nano-hydroxyapatite/chitosan, nano-zirconia/chitosan and novel nano-calcium zirconate/chitosan composite scaffolds for their potential applications in bone regeneration. *Materials science and engineering: C*. 2018; 91, 330-339. <https://doi.org/10.1016/j.msec.2018.05.060>
- [3] Gönen SÖ, Taygun ME, Küçükbayrak S. Fabrication of bioactive glass containing nanocomposite fiber mats for bone tissue engineering applications. *Composite structures*. 2016; 138, 96-106. <https://doi.org/10.1016/j.compstruct.2015.11.033>
- [4] Hsu FY, Hsu HW, Chang YH, Yu JL, Rau LR, Tsai SW. Macroporous microbeads containing apatite-modified mesoporous bioactive glass nanofibres for bone tissue engineering applications. *Materials science and engineering: C*. 2018; 89, 346-354. <https://doi.org/10.1016/j.msec.2018.04.027>
- [5] Mallick SP, Singh BN, Rastogi A, Srivastava P. Design and evaluation of chitosan/poly(l-lactide)/pectin based composite scaffolds for cartilage tissue regeneration. *International journal of biological macromolecules*. 2018; 112, 909-920. <https://doi.org/10.1016/j.ijbiomac.2018.02.049>
- [6] Moghanian A, Sedghi A, Ghorbanoghli A, Salari E. The effect of magnesium content on in vitro bioactivity, biological behavior and antibacterial activity of sol-gel derived 58s bioactive glass. *Ceramics international*. 2018; 44(8), 9422-9432. <https://doi.org/10.1016/j.ceramint.2018.02.159>
- [7] Rahaman MN, Day DE, Bal BS, Fu Q, Jung SB, Bonewald LF, Tomsia AP. Bioactive glass in tissue engineering. *Acta biomaterialia*. 2011; 7 (6), 2355-2373. <https://doi.org/10.1016/j.actbio.2011.03.016>
- [8] Bellucci D, Cannillo V, Ciardelli G, Gentile P, Sola A. Potassium based bioactive glass for bone tissue engineering. *Ceramics international*. 2010; 36(8), 2449-2453. <https://doi.org/10.1016/j.ceramint.2010.07.009>
- [9] Turnbull G, Clarke J, Picard F, Riches P, Jia L, Han F, Li B, Shu W. 3D Bioactive composite scaffolds for bone tissue engineering. *Bioactive materials*. 2018; 3 (3), 278-314. <https://doi.org/10.1016/j.bioactmat.2017.10.001>
- [10] Vyas V, Kaur T, Thirugnanam A. Chitosan composite three dimensional macrospherical scaffolds for bone tissue engineering. *International journal of biological*

- macromolecules. 2017; 104, 1946-1954. <https://doi.org/10.1016/j.ijbiomac.2017.04.055>
- [11] Balasubramanian P, Büttner T, Pacheco VM, Boccaccini AR. Boron-containing bioactive glasses in bone and soft tissue engineering. *Journal of the European ceramic society*. 2018; 38(3), 855-869. <https://doi.org/10.1016/j.jeurceramsoc.2017.11.001>
- [12] Erol M, Boccaccini AR, Stark WJ, Mohn D, Hong Z, Mano JF. Polymer/bioactive glass nanocomposites for biomedical applications: a review. *Composites science and technology*. 2010; 70(13), 1764-1776. <https://doi.org/10.1016/j.compscitech.2010.06.002>
- [13] Lacroix J, Jallot E, Lao J. Gelatin-bioactive glass composites scaffolds with controlled macroporosity. *Chemical engineering journal*. 2014; 256, 9-13. <https://doi.org/10.1016/j.cej.2014.06.022>
- [14] Bowen CR, Thomas T. Macro-porous Ti2AlC MAX-phase ceramics by the foam replication method. *Ceramics international*. 2015; 41(9), 12178-12185. <https://doi.org/10.1016/j.ceramint.2015.06.038>
- [15] Pontremoli C, Boffito M, Fiorilli S, Laurano R, Torchio A, Bari A, Tondra-Turo C, Ciardelli G, Vitale-Brovarone C. Hybrid injectable platforms for the in situ delivery of therapeutic ions from mesoporous glasses. *Chemical engineering journal*. 2018; 340, 103-113. <https://doi.org/10.1016/j.cej.2018.01.073>
- [16] Kokubo T, Huang ZT, Hayashi T, Sakka S, Kitsugi T, Yamamuro T. Ca, P-rich layer formed on high-strength bioactive glass-ceramic A-W. *Journal of biomedical materials research*. 1990; 24, 331-343. <https://doi.org/10.1002/jbm.820240306>
- [17] Haseraki S, Alizadeh M, Nazarian H, Sharifi D. Physico-chemical and in vitro biological evaluation of strontium/calcium silicophosphate glass. *Journal of material science: materials in medicine*. 2010; 21, 695-705. <https://doi.org/10.1007/s10856-009-3920-0>
- [18] Mansur HS, Costa HS. Nanostructured poly(vinyl alcohol)/bioactive glass and poly(vinyl alcohol)/chitosan/bioactive glass hybrid scaffolds for biomedical applications. *Chemical engineering journal*. 2008; 137, 72-83. <https://doi.org/10.1016/j.cej.2007.09.036>
- [19] Varmette EA, Nowalk JR, Flick LM, Hall MM. Abrogation of the inflammatory response in LPS-stimulated RAW 264.7 murine macrophages by Zn- and Cu-doped bioactive sol-gel glasses. *Journal of biomedical materials research A*. 2009; 90(2), 317. <https://doi.org/10.1002/jbm.a.32098>



Research on Engineering Structures & Materials

In This Issue

Research Article

105

Mehmet Palanci

Yield response prediction of unsymmetrically reinforced concrete rectangular beams

Research Article

119

Serço Serkis Yeşilkaya, Ünzile Ulutaş

Band gap modification of spray pyrolysed ZnS films by doping and thermal annealing

Research Article

127

Sevim Alisir, Sinem Cevik

The effects of foundry sand components on the cast iron

Research Article

141

Tuğba Gürmen Özçelik

Investigation of glycerol-Ni(NO₃)₂·6H₂O /perlite composites as form stable phase change materials

Research Article

153

Hatice Aysin Karahan Toprakci, Ayse Turgut, Ozan Toprakci

Fabrication and characterization of vapor grown carbon nanofiber reinforced flexible polymer composites

Research Article

167

Emmanuel Folorunso Olasehinde, Segun Michael Abegunde

Preparation and characterization of a new adsorbent from raphia taedigera seed

Research Article

183

Ahsen Ünal, Işıl Özer, Melek Erol Taygun, Sadriye Küçükbayrak

Fabrication and in-vitro evaluation of copper doped bioactive glass/polymer composite scaffolds for bone tissue engineering

C
O
N
T
E
N
T



Research on
Engineering
Structures & Materials

